博士論文

Development of metal-organic framework/polymer hybrids as cancer theranostics

(金属有機構造体/高分子ハイブリッドによるがんセラノスティクスの開発)

黎　上瑋

レイ　ジョウイ

博士論文

Development of metal-organic framework/polymer hybrids as cancer theranostics

(金属有機構造体/高分子ハイブリッドによるがんセラノスティクスの開発)

Doctoral Dissertation

Department of Bioengineering

Graduate School of Engineering

The University of Tokyo

2024

黎　上瑋 Li Shang-Wei

Preface

This dissertation summarized my main research project conducted during three years of doctoral course in The University of Tokyo from April of 2021 to March of 2024.

This study is a collaboration between The University of Tokyo and National Taiwan University. We focused on investigating the promising versatile cancer theranostics platform based on metal-organic framework with the surface stabilization via block copolymers. The results revealed in this dissertation are encouraging as our MOF/polymer hybrid system demonstrated effective antitumor responses and promising imaging capability. This system can be served as the model for the future development of MOF based theranostic platforms.

Here, I would like to give my heartfelt appreciation to Associate Professor Horacio Cabral for not only accepting me in his lab but also the enormous help during the 3-year of PhD study, especially during the period of COVID-19 entry restriction (2020/10/1~2022/04/01). Also, I want to express my appreciation to Dr. Taehun Hong and Mr. Pengwen Chen for their help in experimental techniques as well as Dr. Lucas Mixich for his continuous encouragement. Additionally, I am deeply grateful to Mrs. Hiroko Koyama for her secretarial support and office work.

Finally, I appreciate the financial support from The University of Tokyo Fellowship and the support from the office of The International Multidisciplinary Engineering (IME) Graduate Program.

Li Shang-Wei, 2024/01/28

Department of Bioengineering,

Graduate School of Engineering, The University of Tokyo

Contents

Chapter 1.

General Introduction

1.1 Cancer theranostics

Cancer theranostics, which combines diagnostic and therapeutic approaches, have gained significant attention for their ability to provide real-time monitoring and targeted cancer interventions. One of the key aspects of cancer theranostics is the development of targeted therapies that can specifically identify and attack cancer cells while minimizing damage to healthy tissues (Yordanova *et al.*, 2017). Unlike traditional cancer therapy, where monitoring and treatment are separate processes, theranostics allows for simultaneous imaging and treatment through the integration of advanced imaging techniques and targeted therapies (McNerney *et al.*, 2021). The real-time feedback can be used to adjust the application of drugs, track patient prognosis, and improve overall treatment outcomes. This approach has shown promise in improving treatment outcomes and patient quality of life (Turner, 2018). One pioneering example is the integration of supramolecular chemistry and nanotechnology to create a promising platform for cancer theranostics, offering high therapeutic performance and negligible long-term immunotoxicity (G. Yu *et al.*, 2018). Additionally, bio-inspired nanoparticles have been explored for their theranostic applications in cancer, showcasing the diverse and evolving nature of cancer theranostics (Madamsetty *et al.*, 2019). The ongoing advancement of protein-based nanoformulations for cancer theranostics in recent years has further expanded the scope of theranostic approaches (Gou *et al.*, 2018). Moreover, the increasing employment of nano-based approaches in theranostics has contributed to the development of advanced strategies to treat cancer (Evangelopoulos *et al.*, 2018).

The progress of nanotechnology has significantly contributed to faster, safer, and more effective cancer therapy (Alshehri *et al.*, 2021). Nanomaterials, such as bismuth sulfide nanorods and two-dimensional nanomaterials, have been explored for their potential in multimodal imaging and guided photothermal therapy of tumors (J. Liu *et al.*, 2015; Raja *et al.*, 2020). Furthermore, the functionalization of nanoparticles with aptamers has enabled cancer-specific recognition and sequential photodynamic-chemo theranostics, highlighting the versatility of nanomedicine in cancer treatment (Jin *et al.*, 2021). Various types of theranostic polymer and metal nanoparticles have been explored for their roles in cancer therapy and imaging, highlighting their potential for future applications in dendritic cell cancer vaccination, gene delivery, T cell activation, and immune modulation (Nabil *et al.*, 2019). Moreover, metallic, polymeric, and lipid-based systems have emerged as efficient and safer alternatives in cancer management, demonstrating the diverse range of materials being investigated for cancer theranostics (Silva *et al.*, 2019). Nanotheranostic approaches, such as polymeric micelles, are being explored as promising approaches in personalized medicine for cancer offering real-time molecular imaging (Domingues *et al.*, 2019). Advances in cancer theranostics have also been driven by the development of novel sensitizers for phototherapy with disease-activated signals for imaging-guided therapy (Turner, 2018). The clinical practice of theranostics in oncology has gained substantial attention, particularly in the context of personalized medicine, and the preclinical research in the development and application of theranostic systems has significantly contributed to the advancement of cancer theranostics emphasizing the growing significance of theranostics in cancer management (Johnson *et al.*, 2021; Turner, 2018).

Despite the progress in cancer theranostics, there are challenges that need to be addressed. The clinical applicability of these materials for cancer theranostics is currently limited to a small subset of cancer types, highlighting the need for broader applications across different

cancer types (van der Heide & Dalm, 2022). Although the development of multifunctional nanoparticle-based theranostics has shown promise, there is a need to bridge the gap between proof-of-concept research and clinical translation. Additionally, to achieve efficient *in vivo* monitoring, the imaging agents should be confined within the delivery platform to prevent premature loss of the imaging signal. Therefore, a well-designed delivery platform with improved loading capacity and manufacturing ease is crucial for the development of cancer theranostics.

To create an effective cancer theranostics system, the engineering of a versatile delivery platform is essential. The ideal platform should be nanosized, biocompatible, highly porous for efficient drug loading, easily manufacturable, and possess a modifiable surface (Hapuarachchige & Artemov, 2020). To address these issues, many metal nanoparticles, liposomes and polymeric micelles platforms are developed (C. Liang *et al.*, 2016; J. Yang & Yang, 2020). Moreover, researchers are focusing on mesoporous silica nanoparticles as promising candidates for drug delivery due to their high loading capacity. (Kumar *et al.*, 2018). However, these currently used drug delivery systems for cancer theranostics are still imperfect due to the drug loading efficiency, imaging capability, complexity, stability, and biocompatibility. Furthermore, a platform that facilitates in situ synthesis of transitional metal nanoparticles would greatly enhance the application of photothermal therapy (PTT) and photodynamic therapy (PDT) as pinpoint therapies in cancer theranostics. Hence, there are still needs for developing novel platforms for cancer theranostics. The success of cancer theranostics relies on three key components: effective pin-point cancer interventions, suitable monitoring approaches, and versatile delivery platforms **(Figure 1.1)**. An emerging porous material: metal-organic frameworks (MOFs) is drawing attention for their applications in cancer theranostics because of its versatile characteristics (Munawar *et al.*, 2023). Furthermore, MOFs distinguish themselves from currently developed materials through the intrinsic MRI

capability and reactivity by the metals within their structures (P. Horcajada *et al.*, 2010). Therefore, the nanoparticles with porous structure, various imaging techniques, and ease of modification such as MOFs will be favorable to make as the versatile delivery platforms for cancer theranostics.

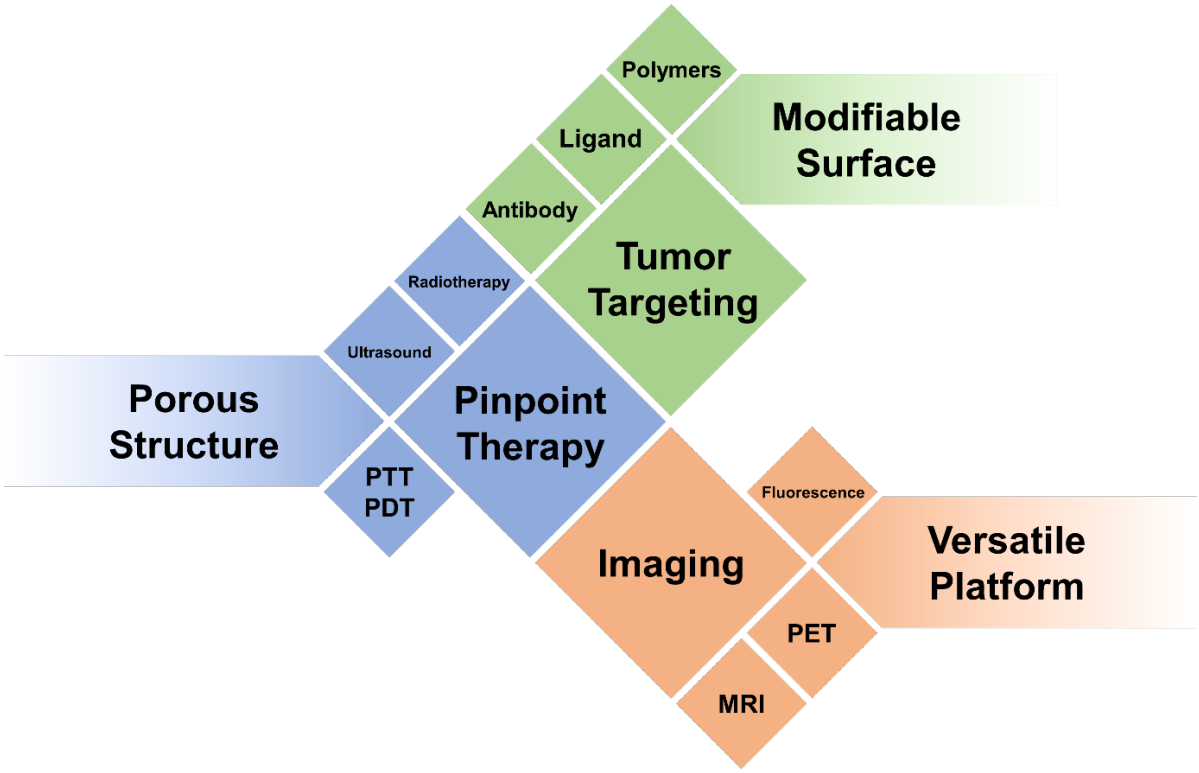

Figure 1.1 The principles of successful cancer theranostics.

1.2 Metal organic frameworks (MOFs)

Metal-organic frameworks (MOFs) are a class of porous materials that have garnered significant attention due to their diverse applications in various fields. MOFs are hybrid inorganic-organic materials, consisting of metal clusters or ions (nodes) connected by organic ligands (linkers) to form a three-dimensional porous framework (J. Yang & Yang, 2020). These materials possess high surface area (1,000~14,000 m^2 g^{-1}), tunable porosity, and ordered crystal frameworks, making them ideal for applications in chemical sensors, catalysis, and hydrogen storage (Garai & Yavuz, 2021; J. Yang & Yang, 2020). Additionally, MOFs exhibit cage-like structures and high porosities, which have shown promising applications in biomedical applications (J. Yang & Yang, 2020). These characteristics make MOFs an ideal platform for drug delivery systems, as they provide excellent loading capacities, easy body clearance, and low toxicity (Yin *et al.*, 2021). Furthermore, MOFs can be tailored to exhibit controlled drug release, prolonged blood circulation, and accurate bioimaging as the contrast enhancing agents, making them advantageous for cancer theranostics (Xu *et al.*, 2021).

MOFs have garnered significant attention in the field of cancer theranostics due to their unique properties including the modifiable surface, high porosity, intrinsic capability for MRI imaging and the ordered crystal structure as the versatile platforms. Especially, nanoscale MOFs have shown potential in various biomedical applications, owing to their ability to mediate radical therapy and enhance cancer immunotherapy (Ni *et al.*, 2020). Furthermore, the development of mixed-ligand MOFs has multiplied their properties and improved their versatility for theranostic applications, including controlled drug delivery and enhanced photodynamic therapy (H. Zhang & Yin, 2022). The structural and functional versatility of MOFs has also been harnessed for imaging-guided photo-chemotherapy, demonstrating their potential as multifunctional theranostic platforms (Yuan *et al.*, 2022). For example, a copper-based MOF exhibited dual functionalities of MRI-guided photothermal therapy (PTT) and

photodynamic therapy (PDT) in tumor bearing mice as a cancer theranostics agent (B. Li *et al.*, 2018). Due to their high porosity, MOFs offer the ability to simultaneously load multiple drugs. Moreover, the rigid and fixed-sized pores within MOF materials enable them to serve as scaffolds for controlling the size of nanoparticles formed within. For example, MOFs have been explored to incorporate with the bioactive molecules such as enzyme and even bacteria (W.-H. Chen *et al.*, 2018; J. W. Wang *et al.*, 2021). These biological reactive MOFs are small-sized bio-factories in the cells that can provide desire functionalities. In addition to biomolecules, the metal nanoparticles such as some transitional metal-based photothermal agents can be directly synthesized with the help of well-defined crystal structure within MOFs served as the scaffold resulting in a highly biocompatible photothermal agent (J. Yu *et al.*, 2017). This also allows for facile in situ synthesis of transitional metal nanoparticles. Another advantage of MOFs is their ease of surface modification. The remaining functional groups from the organic linkers and metal ions on the MOF surface can be used for further conjugations or modifications. Thus, nanosized MOFs hold great promise as versatile delivery platforms for cancer theranostics.

Among all the MOFs such as zinc-, copper-, and iron-based MOFs, the MIL-100(Fe) (MIL: Materials Institute Lavoisier), which is constructed from $[Fe_3O(OH^-)(H_2O)_2]^{6+}$ clusters and trimesic acid (BTC), exhibited one of the highest biocompatibilities (Patricia Horcajada *et al.*, 2007). Its rigid zeotype structure creates two distinct cavities: one measuring 25 Å and the other 29 Å, accessible through windows sized at 5.5 Å and 8.6 Å, respectively **(Figure 1.2)** (Patricia Horcajada *et al.*, 2007). Additionally, the porous, cage-like structure, and the easily modifiable surface render MIL-100(Fe) into a promising versatile platform for cancer theranostic **(Figure 1.2)**. From the previous reports of the lethal doss 50 (LD_{50}) indicating the concentration of killing 50% of the testing animals, the constituents of MIL-100(Fe) including Fe, and BTC show high LD_{50} values implying low toxicity **(Table 1.1)** (Egorova & Ananikov,

2017; Q. Yang *et al.*, 2016). Because of the favorable biocompatibility, MIL-100(Fe) has emerged as an attractive candidate for drug delivery and biomedical applications. Research studies have demonstrated the potential of MIL-100(Fe) as a drug delivery platform for various drugs, including flurbiprofen, isoniazid, and chloroquine (Al Haydar *et al.*, 2017; B. T. Le *et al.*, 2023; Simon *et al.*, 2019). The high drug loading capacity and controlled release properties of MIL-100(Fe) make it suitable for delivering a wide range of drugs, including poorly soluble drugs like norfloxacin (Yadav *et al.*, 2023). Furthermore, MIL-100(Fe) has been utilized in theranostic applications, enabling simultaneous tracking and combating of breast cancer (Mokhtarian *et al.*, 2022). Its potential in cancer therapy and as a carrier for anticancer drugs has been highlighted, showcasing its versatility in biomedical applications.

Although MIL-100(Fe) is reported to be highly stable in water, the exposed surface of MIL-100(Fe) makes it easily aggregated (Gao *et al.*, 2019; Simon-Yarza *et al.*, 2016). One of the main challenges in implementing MOFs such as MIL-100(Fe) in biomedical applications is the release of metal ions and the reactive surface, which can lead to instability under physiological conditions (Simon-Yarza *et al.*, 2016). MIL-100(Fe) with high drug loading capability and biocompatibility holds promise for therapeutic applications. However, its bioactive surface hinders its applications. A previous study showed that MIL-100(Fe) quickly aggregated in physiological conditions. Additionally, MIL-100(Fe) after systemic injection is cleared from blood within an hour (Simon-Yarza *et al.*, 2016). It is said that MIL-100(Fe) binds with plasma proteins forming the protective protein corona (Kush *et al.*, 2020). However, the high deposit of MIL-100(Fe) is found in the liver and spleen indicating its low *in vivo* serum stability (Simon-Yarza *et al.*, 2016). MIL-100(Fe) is a promising drug delivery system, but its poor pharmacokinetics limits its biomedical applications. Other MOFs and nanoparticles such as carbon-coated FeCo nanoparticles require surface stabilization to improve biodistribution (Song *et al.*, 2020). Therefore, it is essential to stabilize the surface of MIL-100(Fe) in order to

render it into practical drug delivery system. By implementing appropriate surface protection on MIL-100(Fe), we can enhance its colloidal and chemical stability in physiological conditions, resulting in increased bioactivity and facilitating *in vivo* drug delivery (Bunzen, 2021). Only the MIL-100(Fe) with appropriate surface stabilization can lead to the versatile cancer theranostic platforms.

Table 1.1 LD_{50} of the common component (metal and organic linkers) of MOFs.

Metals	LD_{50} (mg/kg)	Organic linkers	LD_{50} (mg/kg)	Other materials	LD_{50} (mg/kg)
Fe	30000	Trimesic acid (BTC)	8400	PEG12K	22000
Mg	8100	Terephthalic acid (BDC)	5000	Poly(vinylalcohol)	5000
Ca	1000	Isonicotinic acid	5000	Aspartic acid	9000
Zn	0.35	2-methylimidazole	1400	Liposomes	5-20

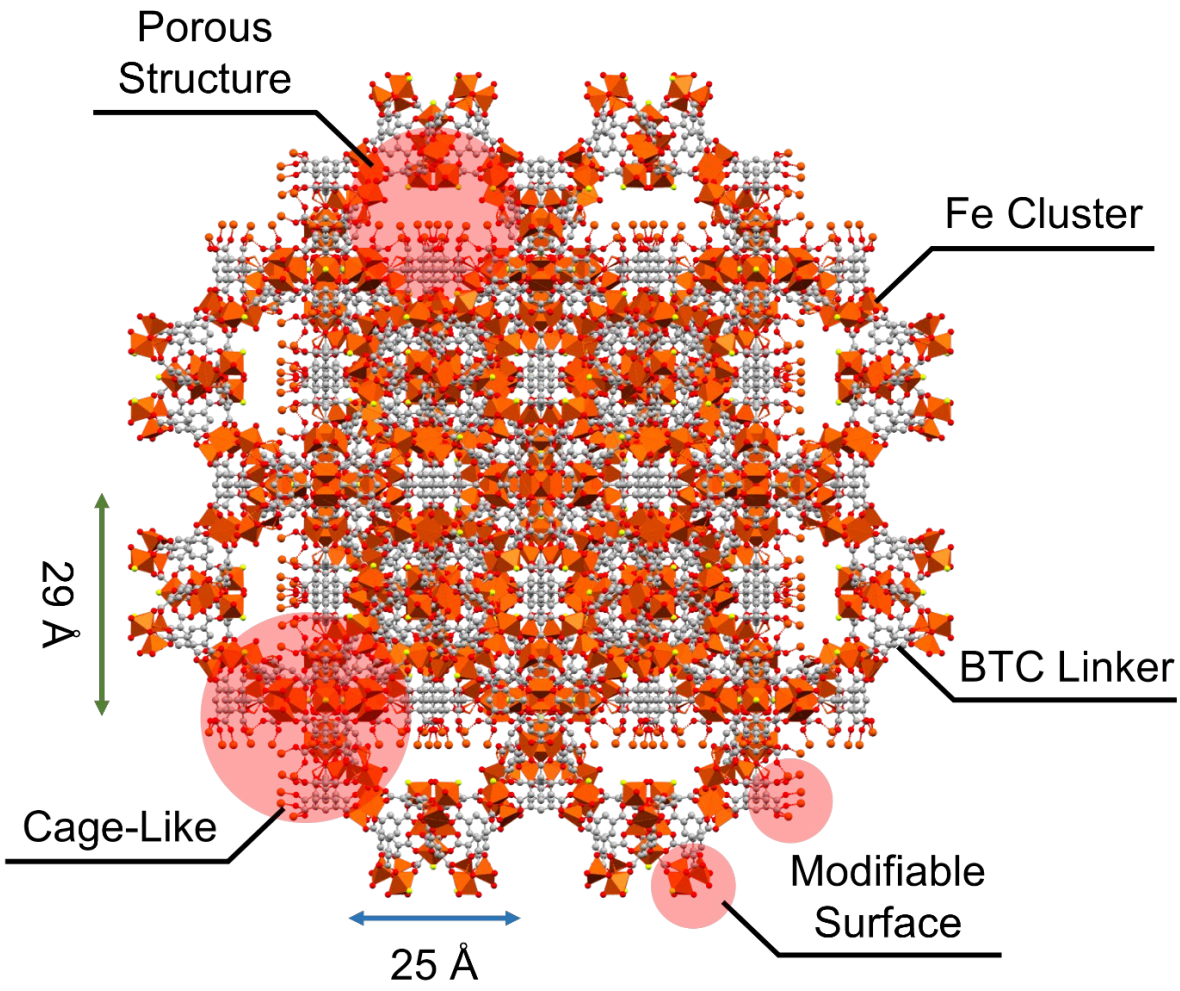

Figure 1.2 The structure and key points of MIL-100(Fe)

1.3 Strategies for surface stabilization

Many nanoparticles, especially metal nanoparticles or MOFs, have the challenge of preventing aggregation in the physiological conditions (Simon-Yarza *et al.*, 2016; Song *et al.*, 2020). Hence, the surface coating of nanoparticles plays a crucial role in cancer treatments, particularly in targeted drug delivery and therapy since the coating not only improves the stability and biocompatibility, but also provides the enhanced tumor targeting efficacy (Dai *et al.*, 2018). Targeting ligands such as small organic molecules, peptides, antibodies, and nucleic acids have been added to the surface of nanoparticles to specifically target cancerous cells through selective binding to the receptors overexpressed on their surface (Sun *et al.*, 2014). Additionally, after coating of the surface by polymers, it is reported to be versatile as the polymers can serve as additional layer for functionalization (Budijono *et al.*, 2010). With the ability of fostering the biodistribution, pharmacokinetic and potential of adding additional functions, the proper surface protection by biocompatible materials such as poly(ethylene glycol) (PEG) polymers is crucial for the application of nanoparticles on cancer theranostic.

Similarly, while MOFs offer promising properties for various applications, their stability in physiological media and the tendency of aggregation have been areas of concern (Christodoulou *et al.*, 2021). The stability of MOFs in physiological conditions is crucial for their potential biomedical applications, such as drug delivery and biological imaging. The aggregation of MOFs in physiological conditions has been observed in various studies, highlighting the need for improved stability and dispersion of MOFs to fully utilize the potential of MOFs in biomedical applications (B. Chen *et al.*, 2022; Malonzo *et al.*, 2018). Furthermore, the instability of MOFs in physiological media has been a significant challenge, particularly in the context of targeted drug release and biocompatibility (Poryvaev *et al.*, 2021). Efforts have been made to address this issue by surface stabilization with polymers (Shi *et al.*, 2020).

The surface coating of nanoparticles with polymers is a critical aspect of their functionalization for various applications, including drug delivery and cancer therapy. The use of polymers such as PEG as coatings on nanoparticles has been shown to influence cellular uptake, cytotoxicity, and biocompatibility. Additionally, the surface charge of nanoparticles coated with polymers has been found to influence cell localization and cytotoxicity, highlighting the significance of polymer coatings in cellular interactions (Asati *et al.*, 2010). Furthermore, the use of polydopamine, heparosan polysaccharide and PEG as a surface coating on nanoparticles such as MOFs has been reported to reduce serum protein adsorption and enhance cellular uptake, demonstrating the potential of polymer coatings in improving nanoparticle interactions with biological systems (Shi *et al.*, 2021; W. Yang *et al.*, 2022).

To deal with the issue of aggregation of MOFs such as MIL-100(Fe) in physiological conditions, the surface coating by the biocompatible polymers holds promise for enhancing the biodistribution (Shi *et al.*, 2021; Z. Zhang *et al.*, 2015). The combination of MOFs with highly biocompatible polymer, PEG, has been extensively explored, leading to the development of advanced composites and tailored architectures (Kalaj *et al.*, 2020). These hybrid materials offer unique properties arising from MOFs and polymer composite systems (MOF/polymer hybrids), making them suitable for biomedical applications (Giliopoulos *et al.*, 2020). The utilization of MOF/polymer hybrids in biomedical applications has been widely studied due to their improved biodistribution and the versatility of MOFs for cancer theranostic (Giliopoulos *et al.*, 2020).

The synthesis of MOF-polymer hybrids involves various techniques such as grafting, post-synthetic polymerization, templating, bottom-up assembly and complexation, which have been developed to achieve favorable interfacial interactions and enhance the properties of the resulting materials (Giliopoulos *et al.*, 2020; Hansson *et al.*, 2013; Troyano & Maspoch, 2023; Vrtovec *et al.*, 2023). Covalent bonding between MOFs and polymers has been explored to

improve the compatibility and catalytic activity of the hybrid materials (Kalaj *et al.*, 2020; Nunes *et al.*, 1982). Additionally, the use of complexation between the exposed metal ions on the surface of MOFs and the polymer functional groups such as carboxylates or catechol has been considered as one of the most promising approaches because of the flexibility and stability (Porter *et al.*, 2010). The interface between MOFs and polymers plays a crucial role in determining the properties of the resulting hybrid materials. The design of MOF-polymer interfaces is shown to have a significant impact on selectivity, highlighting the importance of engineering the interface for specific applications (Kalaj *et al.*, 2020; Pander *et al.*, 2023; Schmitt *et al.*, 2016). Therefore, the surface coating with polymers helps nanoparticles such as MOFs to unleash their full potential on biomedical applications as the versatile cancer theranostic platforms for incorporating pinpoint therapy and imaging capability.

1.4 Pinpoint therapy

Pinpoint therapy in cancer treatment aims to tailor medical treatment to maximize the specificity to tumors while minimize the damage to normal tissues (Yau, 2019). This approach involves the identification of molecular and tumor microenvironment patterns, which can then be targeted with therapies, thereby revolutionizing oncology (Friedman *et al.*, 2015). Pinpoint therapy utilizes biomarkers, including proteins and genes, to guide targeted therapy in various types of cancer, such as lung cancer and ovarian cancer (Imaoka *et al.*, 2021). In the context of cancer treatment, it also plays a crucial role in overcoming resistance to targeted therapies. A previous study demonstrates the potential of targeting molecular changes in plasma specific to anti-PD-1 therapy, showcasing the application of pinpoint therapy by immunotherapy for metastatic cutaneous melanoma (Babacic *et al.*, 2020).

Another approach of pinpoint therapy involves the use of precisely controlled high energy beam such as radiation and concentrated near-infrared (NIR) light to achieve tumor ablation. Photothermal therapy (PTT), photodynamic therapy (PDT), and radiotherapy are promising modalities in pinpoint cancer treatment. PTT utilizes light-absorbing agents to generate heat and induce tumor cell death via hyperthermia, while PDT involves the activation of photosensitizing agents to produce cytotoxic reactive oxygen species (ROS) upon light exposure (X. S. Li *et al.*, 2020). Radiotherapy, on the other hand, employs ionizing radiation to damage the DNA of cancer cells. These approaches have shown potential in precision cancer therapeutics, especially when combined with nanoparticle-based drug delivery systems such as MOFs, liposomes, and polymeric micelles (Qin *et al.*, 2023).

Nanoparticles have been extensively explored in PDT, with their ability to enhance the efficacy of photosensitizing agents and enable targeted delivery (Lucky *et al.*, 2015). PDT involves the administration of a photosensitizing agent, which accumulates in the tumor,

followed by irradiation with light of a specific wavelength, leading to the activation of the photosensitizer and the generation of ROS, ultimately causing cancer cell apoptosis and necrosis (Correia *et al.*, 2021; X. S. Li *et al.*, 2020). This approach has shown potential in various types of cancer, including bladder cancer (Inoue, 2017), nasopharyngeal cancer (Wildeman *et al.*, 2009), and breast cancer (Y. Yu *et al.*, 2023). The use of nanoscale MOFs has been explored to overcome hypoxia for PDT-primed cancer immunotherapy, demonstrating the ability of PDT to alter the tumor microenvironment and enhance the efficacy of immune checkpoint blockade therapy (Lan *et al.*, 2018). The PDT holds great promise as a non-invasive and selective cancer therapeutic treatment.

The wavelength of light used in photothermal therapy (PTT) is crucial, primarily due to its limited penetration into the skin. Shorter wavelength light carries higher energy but penetrates less deeply, typically reaching depths of less than 3 mm. Conversely, longer wavelengths, such as near-infrared (NIR), can penetrate deeper, reaching over 6 mm into the skin—twice the depth of shorter wavelengths (J. Li *et al.*, 2021). Hence, scientists are directing their attention toward leveraging NIR light-absorbing agents such as transitional metal nanoparticles (Au, and Pd) or organic dyes (indocyanine green), which convert optical energy into heat (Guo *et al.*, 2023; J. Li *et al.*, 2021). This conversion process results in thermal ablation of cancer cells, making NIR a promising tool in cancer treatment (Shirata *et al.*, 2017). This approach has gained attention due to its potential for targeted cancer therapy, with the ability to selectively kill cancer cells while minimizing damage to surrounding healthy tissue (J. Wang *et al.*, 2018). PTT has advantages over traditional treatment methods because of its non-invasiveness, targeted therapy, and minimal side effects.

Additionally, the combination of PTT and PDT which is usually not able to separate has demonstrated synergistic effects in antibacterial and cancer therapy, offering a dual-modal approach for enhanced treatment outcomes (Overchuk *et al.*, 2023; Shirata *et al.*, 2017). The

combination of PTT or PDT with chemotherapy is shown as an auspicious approach for pinpoint therapy (X. S. Li *et al.*, 2020). Moreover, the combination of PTT and PDT with radiotherapy has been proposed as a multi-targeted approach in cancer treatment, aiming to sensitize tumors to radiotherapy and enhance the efficiency of phototherapeutic regimens (Kenny & Marmion, 2019). This combination therapy has the potential to overcome the limitations of each individual modality and improve overall treatment efficacy.

The development of nanoplatforms for dual-modal imaging and combination of PTT and PDT has paved the road for cancer theranostics, offering both diagnostic and therapeutic functionalities (Fu *et al.*, 2022). The combination of PTT and PDT with advanced imaging techniques holds promise for precise and spatiotemporal destruction of tumor tissues, with minimal harm to normal tissues and reduced drug resistance. Recently, MOFs with the high drug loading capacity and the versatility have been developed as the promising nanoplatforms for combining PTT and PDT with imaging technologies (Zheng *et al.*, 2021). MOFs have been explored for their ability to enhance the anticancer efficacy of PTT, PDT, and drug delivery (Zheng *et al.*, 2021). The incorporation of photothermal agents into MOFs with the irradiation of NIR light shows PTT and PDT improving their performance for cancer therapy (Ye *et al.*, 2022; Zheng *et al.*, 2021). Furthermore, with regards to the imaging-guided therapy, MOFs have also been utilized to encapsulate drugs and photothermal agents, enabling tumor-targeted and fluorescence imaging-guided chemo-photothermal therapy (Huiyuan Zhang *et al.*, 2018). It is clear that MOFs are promising theranostic nanoplatforms with magnetic resonance and fluorescent imaging for synergistic phototherapy of cancers, showcasing their multifunctional capabilities in pinpoint cancer treatment (B. Li *et al.*, 2018).

To maximize the potential of the pinpoint therapy such as PTT and PDT, a versatile nanoplatform such as MOFs is favorable. The combination of PTT and PDT with advanced imaging technology such as MRI or fluorescence in a single platform further increase the efficacy and precision of the pinpoint therapy **(Figure 1.3)**.

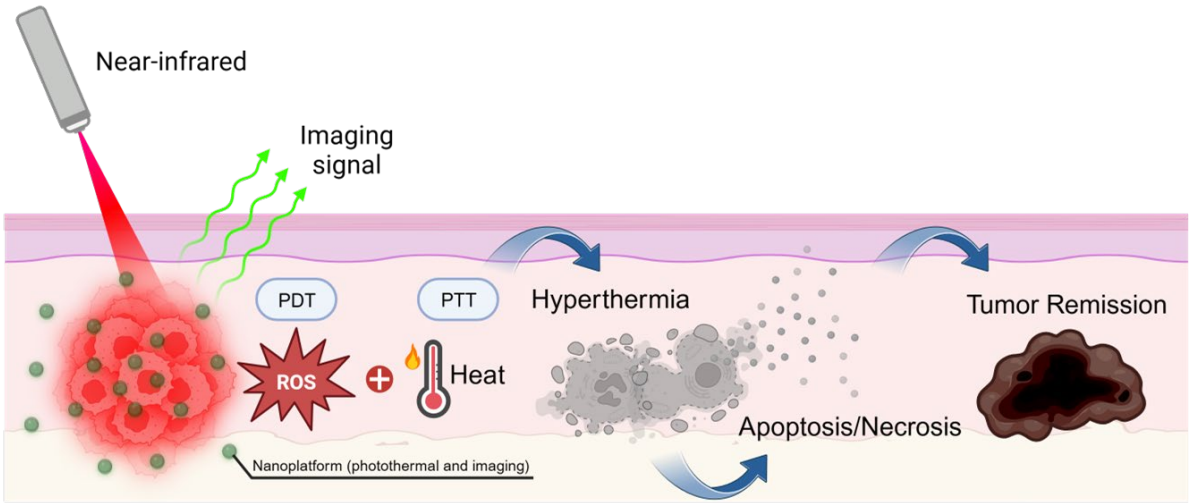

Figure 1.3 The scheme of fluorescence- or MRI-guided pinpoint therapy with PTT and PDT.

1.5 Imaging of tumor

Tumor imaging techniques have indeed showed significant advancements, encompassing various modalities and technologies. Especially, magnetic resonance imaging (MRI) has been at the forefront of these developments, playing a crucial role in tumor imaging, offering various techniques for tumor detection, characterization, and monitoring. To enhance the imaging of tumor, MRI contrast agents are essential for distinguishing tumors from nearby healthy tissues and improving visibility of certain structures or tissues in MRI images. Gadolinium-based nanoparticles (Gd-NPs) are widely used as T_1 agents, as they have been extensively employed as clinical MRI contrast agents (Na *et al.*, 2009). These contrast agents are crucial for improving the sensitivity and resolution of MRI by accelerating the relaxation times of surrounding water protons. However, MRI contrast agents have limitations, including toxicity, short retention time and fast vascular extravasation due to their low molecular weight. Furthermore, safety concerns are associated with the use of contrast agents such as Gd-NPs in MRI, such as the risk of nephrogenic systemic fibrosis (Ishiguchi & Takahashi, 2010). Therefore, while MRI contrast agents offer significant advantages in improving image quality and diagnostic efficiency, their limitations and safety considerations must be carefully addressed in clinical practice.

In addition to MRI, fluorescence imaging has emerged as a valuable tool for intraoperative tumor detection and image-guided surgery, providing real-time visualization of molecular alterations in tumors (K. Wang *et al.*, 2023). The clinical introduction of intraoperative NIR fluorescence imaging has shown promise in increasing the number of complete tumor resections in breast cancer patients undergoing surgery. The rapid development of fluorescence molecular imaging has enabled the specific detection of solid tumors, contributing to improved cancer diagnosis and surgical interventions (K. Wang *et al.*, 2023). The development of fluorescence-guided surgery has been a significant breakthrough,

marginally improving outcomes in brain tumor surgery, highlighting its potential to enhance surgical precision and patient outcomes (Charalampaki *et al.*, 2019). Fluorescence imaging has shown great promise in the specific detection of tumors and image-guided surgery, offering real-time visualization of molecular alterations in tumors. However, similar to MRI contrast agents, it is important to note that most current tracers in both MRI- and fluorescence-based imaging possess some degree of safety concerns, highlighting the need for proper delivery system.

The emerging versatile nanoplatform such as MOFs has been investigated for its imaging capabilities (Munawar *et al.*, 2023). For example, lanthanide europium MOF nanocomposites have been identified as a theranostic nanoplatform for microwave thermo-chemotherapy and fluorescence imaging, offering high quantum efficiency and characteristic emission peak positions for precise tumor imaging (Zhao *et al.*, 2022). Additionally, the use of folic acid-nanoscale gadolinium-porphyrin MOFs has demonstrated dual-modality imaging capabilities, combining fluorescence and MRI for hepatocellular carcinoma (Y. Chen *et al.*, 2019). In this regard, MOFs have been explored for their potential in multimodal imaging-guided synergistic photo-immunotherapy, offering a multifunctional platform for imaging-guided tumor treatment (Fan *et al.*, 2021). The highly biocompatible MIL-100(Fe) has also been reported to exhibit significant MRI contrast effects indicating the intrinsic imaging capability of MIL-100(Fe) (P. Horcajada *et al.*, 2010). Similarly, the NIR-absorbing dye, indocyanine green, is loaded into hyaluronic acid coated MIL-100(Fe) exhibiting not only favorable PTT and PDT effects, but also the clear imaging for tumor through the fluorescence of indocyanine green (H. Liu *et al.*, 2022). Overall, the implementation of versatile nanoplatform such as MIL-100(Fe), can provide the combination of PTT and PDT with advanced imaging technologies via MRI and fluorescence. With additional surface protection with PEG polymers on MIL-100(Fe), such multifaceted nanoplatform hold promise for the cancer theranostics.

1.6 Overview of this dissertation

Despite their promising drug loading and imaging capability, previously developed MOF systems are not ideal theranostic platforms due to their poor serum stability (P. Horcajada *et al.*, 2010). In order to develop a versatile and stable nanoplatform for cancer theranostics, this research aims to design a MIL-100(Fe) based MOF/polymer hybrid. Taking the advantage of effective pinpoint therapy from PTT, we incorporate the palladium nanoparticles (Pd-NPs), which has the highest photothermal conversion efficiency at over 90%, into MIL-100(Fe) (Pd@MIL-100(Fe)) (P. Singh *et al.*, 2023). A distinctive block copolymer, poly(ethylene glycol)-poly(L-aspartic acid) modified with dopamine (PEG-p(Asp-Dopa)), was developed to tackle the surface stabilization of MIL-100(Fe). The stability, biodistribution, PTT efficacy against melanoma, and various imaging approaches for Pd-NPs loaded MIL-100(Fe)/polymer hybrids were demonstrated in this research **(Figure 1.4)**.

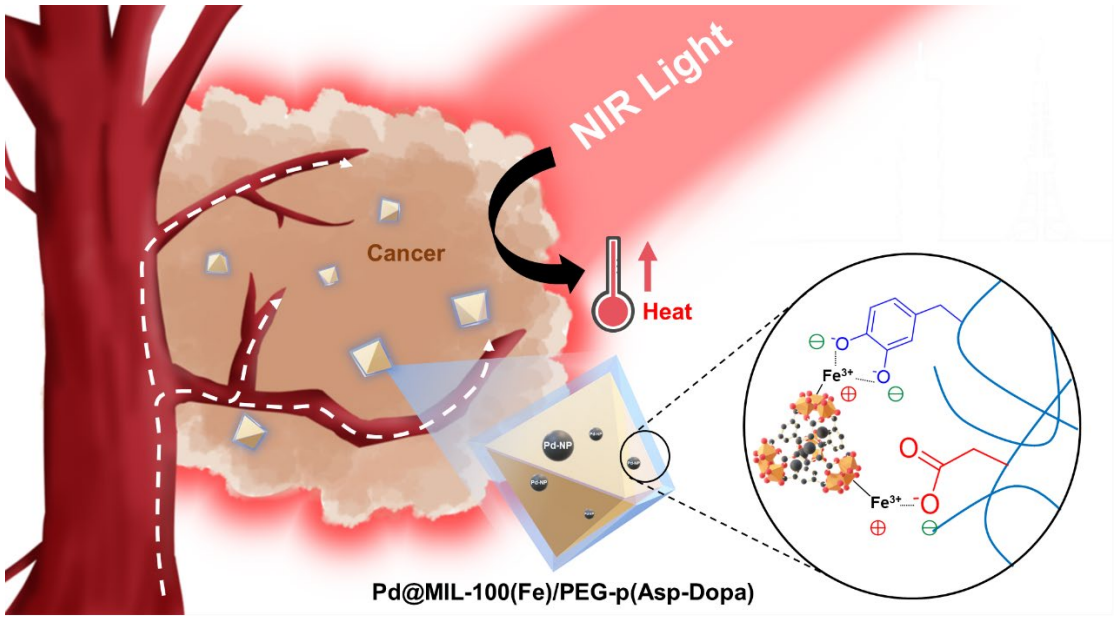

Figure 1.4 The scheme of the photothermal therapy conveyed by Pd@MIL-100(Fe)/PEG-p(Asp-Dopa). The figure was adopted from S. W. Li *et al.* (2023) with the permission.

Chapter 2 delves into the exploration and optimization of various synthesis methods for Pd@MIL-100(Fe), alongside the foundational characterization of this compound. **Chapter 3** focuses on the synthesis of PEG-p(Asp) and PEG-p(Asp-Dopa) block copolymers, providing an in-depth characterization of the resulting Pd@MIL-100(Fe)/polymer hybrids, including aspects like morphology, stability, and photothermal conversion efficiency. In **Chapter 4**, the biodistribution and circulation dynamics of this hybrid system are investigated shedding light on its behavior within the body. This chapter also includes assessments of the system's efficacy in photothermal therapy through *in vitro* experiments on B16F10 cells and *in vivo* antitumor experiments in melanoma-bearing mice, offering insights into the therapeutic potential of Pd@MIL-100(Fe)/polymer hybrids. **Chapter 5** introduces three imaging approaches—loading and conjugation of fluorescent dye, as well as MRI—to showcase the versatility of Pd@MIL-100(Fe)/polymer hybrids as a cancer theranostic platform. Finally, **Chapter 6** offers a comprehensive conclusion, outlining future prospects for the application of block copolymers and MOF/polymer hybrid systems. In this chapter, the remaining challenges and suggests avenues for further enhancements in the current system was addressed.

Chapter 2.

Synthesis of Pd-nanoparticles-loaded MOFs

2.1 Introduction

The conventional synthesis of MOFs, such as MIL-100(Fe), involved solvothermal processes using organic solvents at high temperatures and pressures (Patricia Horcajada *et al.*, 2007). However, for biomedical applications, a biocompatible MIL-100(Fe) has been developed through synthesis in aqueous conditions from iron clusters and BTC organic linkers. Previous studies have successfully demonstrated the facile synthesis of MIL-100(Fe) in water via hydrothermal methods (Simon *et al.*, 2019). Nonetheless, the production of nano-sized MIL-100(Fe) requires microwave-assisted synthesis (Marquez *et al.*, 2012). Alongside MIL-100(Fe), research has revealed that Pd-NPs can be prepared by reducing Pd ions with the presence of surfactants or within a scaffold to precisely control their size (R. W. Liang *et al.*, 2015). This indicates that the well-defined porous structure of MIL-100(Fe) could effectively serve as a scaffold for synthesizing Pd-NPs.

In this chapter, we investigated two distinct approaches for synthesizing MIL-100(Fe), employing both microwave-assisted and hydrothermal methods. Furthermore, we explored two strategies for the preparation of Pd-NPs: de novo (one-pot) and in situ (within MIL-100(Fe)) synthesis. Our focus was on achieving nano-sized Pd-NPs loaded MIL-100(Fe) (Pd@MIL-100(Fe)), necessitating the optimization of parameters in microwave-assisted synthesis. Additionally, we investigated the varying weight ratios between MIL-100(Fe) and Pd to ascertain the optimal photothermal capability of Pd@MIL-100(Fe). Finally, we characterized the resulting Pd@MIL-100(Fe) using powder X-ray diffraction (XRD) and dynamic light scattering (DLS) analyses.

2.2 Materials and methods

2.2.1 Materials

Trimesic acid (H_3BTC) was obtained from Sigma Aldrich (Missouri, USA). Potassium tetrachloropalladate (II) (K_2PdCl_4) was purchased from ThermoFisher Scientific (Waltham, USA). Finally, iron (III) chloride hexahydrate ($FeCl_3 \cdot 6H_2O$) was provided from Merck (New Jersey, USA). L-ascorbic acid was obtained from Tokyo Chemical Industry Co. Ltd. (Tokyo, Japan).

2.2.2 Preparation of MIL-100(Fe) MOFs

The MIL-100(Fe) was prepared with two methods: the water phase synthesis and the microwave-assisted synthesis. Both methods were used and examined to determine the optimal synthesis protocol and parameters. First the facile water phase synthesis was implemented based on the previous synthetization protocol (Simon *et al.*, 2019). In a typical procedure: two different aqueous solutions were prepared: Solution 1 containing 2.5 mmol H_3BTC dissolved in 7.5 mL (1 M) NaOH, and solution 2 containing 3.75 mmol $FeCl_2 \cdot 4H_2O$ dissolved in 32.24 mL deionized water. Solution 1 was added dropwise to Solution 2 under stirring. The molar ratio of Fe:H_3BTC:NaOH is 1.5:1.0:3.0 and the mixture was stirred for 4 h at 35°C. The light-brown solid was recovered by centrifugation at 12,000 x g for 5 minutes and the MIL-100(Fe) was washed once with ethanol and two times by deionized water. The resulting product was stored in deionized water, and a 1 mL sample was oven-dried to ascertain its concentration.

The second method of MIL-100(Fe) preparation was microwave-assisted synthesis which is based on the previous study with major modifications to achieve nano-sized MIL-100(Fe) (Marquez *et al.*, 2012). To synthesize MIL-100(Fe), the Biotage microwave reactor (Biotage Initiator$^+$, Uppsala, Sweden) was used. A 20 mL Biotage microwave reaction vial

contained the solution of $FeCl_3 \cdot 6H_2O$ (0.5, 0.6, 2.0, 4.0 mmol) and H_3BTC (0.3, 0.4, 1.3, or 2.6 mmol) in 20 mL of deionized water. The solution was heated to 130°C and maintained for 2, 3, 4, or 6 min, then quickly cooled down. The centrifugation at 12,000 x g for 5 minutes yielded the orange-colored MIL-100(Fe). The product underwent two washes with water. The MIL-100(Fe) was preserved in a 20 mL water suspension, and the concentration was determined by oven-drying 1 mL of the product.

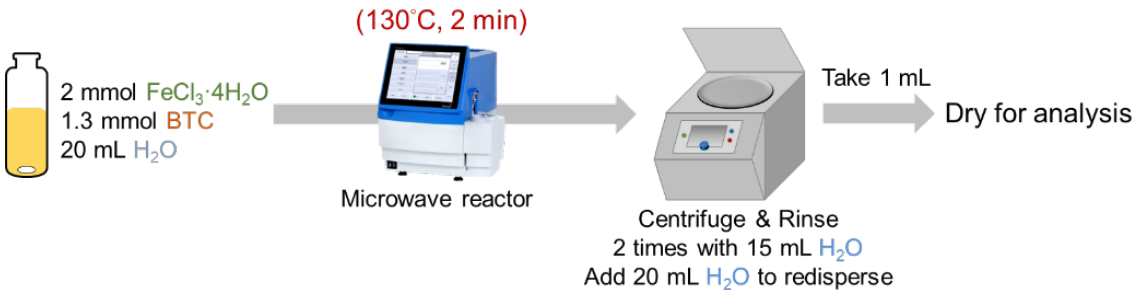

Figure 2.1 Preparation of MIL-100(Fe) via microwave-assisted synthesis.

2.2.3 Synthesis of Pd-NPs inside MIL-100 (Pd@MIL-100) MOFs

The preparation of Pd-NPs loaded MIL-100(Fe) (Pd@MIL-100(Fe)) was accomplished by two methods: the de novo synthesis and the in situ synthesis. In the de novo synthesis, Pd-NPs was synthesized simultaneously with MIL-100(Fe). Briefly, in a 20 mL Biotage microwave reaction vial, $FeCl_3 \cdot 6H_2O$ (4 mmol), H_3BTC (2.6 mmol), and potassium tetrachloropalladate (K_2PdCl_4, 100 mM) were dissolved in 20 mL of deionized water. The solution was heated to 130°C and maintained for 2 min, then quickly cooled down. After washing for 2 times with water, 1 mL of 0.1 M L-ascorbic acid was added dropwise to the solution with stirring. The black solid Pd@MIL-100(Fe) was obtained by centrifugation at 12,000 x g for 5 min. The product was washed with ethanol once followed by water twice.

Another protocol that is adopted from previous research with modifications included the in situ synthetization of Pd-NPs in the MIL-100(Fe) porous structure (R. W. Liang *et al.*, 2015). The following steps were taken to synthesize Pd@MIL-100(Fe) with a mass ratio MIL-100(Fe):Pd of 1:0.0005, 1:0.005, 1:0.05, 1:0.125, and 1:0.25. Initially, 10 mL of the MIL-100(Fe) suspension (10 mg/mL), obtained in the preceding step, was introduced into a 200 mL round bottom flask. Then, 0.01, 0.1, 1, 2.5, and 5 mL of 100 mM potassium tetrachloropalladate (K_2PdCl_4) aqueous solution and 10 mL of water were mixed with the MIL-100(Fe) suspension. The mixture was stirred for 15 min and then 6 mL of ethanol was added. Subsequently, the flask was heated to 90°C and refluxed for 3 h. The product, which had a dark gray color, was washed twice with ethanol and water. The product was stored in 20 mL water. The concentration of the particles was measured by oven-drying 1 mL of the product.

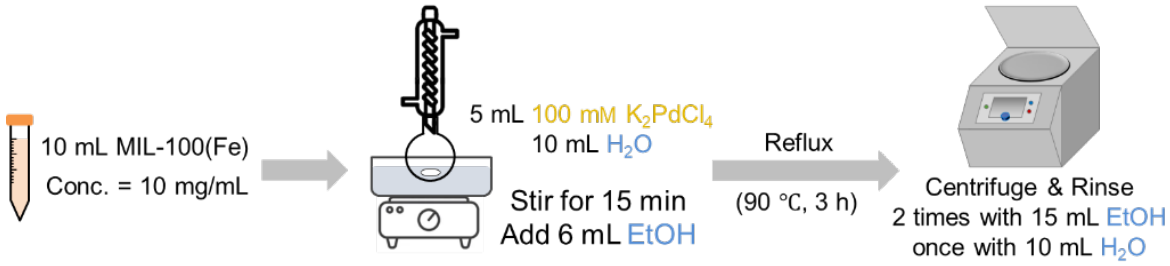

Figure 2.2 Preparation of Pd@MIL-100(Fe) with in situ synthesis

2.2.4 Crystallinity characterization with powder X-ray diffraction

The crystallinity of MIL-100(Fe) and Pd@MIL-100(Fe) was validated using powder X-ray diffraction (XRD) conducted with a MiniFlex600/PTN instrument (Rigaku, Tokyo, Japan). The final products of MIL-100(Fe) and Pd@MIL-100(Fe) were oven-dried and put onto the sample holder for XRD. The power of X-ray was set to 40 kV and 15 mA. The scanning mode was 2θ/θ and the degree of scanning was 2° to 90° with the step size of 0.01°. The XRD raw data was process by Mercury (2021.3, CCDC, Boston, USA). The standard XRD patterns of MIL-100(Fe) (ID: 7102029) was obtained from Crystallography Open Database and Pd-NPs (ID: mp-2) were obtained from The Materials Project (Patricia Horcajada *et al.*, 2007; Jain *et al.*, 2013).

2.2.5 Characterization of particle size

The hydrodynamic diameter of MIL-100(Fe), and Pd@MIL-100(Fe) was determined by dynamic light scattering (DLS) with the Zetasizer Nano-ZS (Malvern Panalytical, Worcestershire, UK). The final product of MIL-100(Fe) and Pd@MIL-100(Fe) were suspended in deionized water at the concentration of about 0.1 mg/mL and loaded into the low-volume quartz cuvette (ZEN2112). Measurements were performed at 25 °C with a 50 mW frequency doubled DPSS Nd:YAG laser (λ=532 nm) at a detection angle of 173°. The average diameter and polydispersity index (PDI) were calculated with cumulant method to represent the characteristics of particle size of MIL-100(Fe) and Pd@MIL-100(Fe).

2.2.6 Optimization of Pd-NPs loading ratio

Pd@MIL-100(Fe) were prepared with a mass ratio MIL-100(Fe):Pd of 1:0.0005, 1:0.005, 1:0.05, 1:0.125, and 1:0.25. The favorable loading ratio of Pd-NPs was determined by the photothermal capability of the Pd@MIL-100(Fe). Both MIL-100(Fe) and Pd@MIL-100(Fe) were diluted to the concentration of 0.5 mg/mL with deionized water. The particle suspensions were transferred to 1.5 mL tubes with 1 mL each. A near infrared (NIR) laser 808 nm was applied at the energy density of 0.6 W/cm^2. The temperature variations were monitored using a digital thermometer (TM-947SD, Lutron, Taipei, Taiwan) connected to a small Pt-100 thermo-resistor positioned inside the tube.

2.2.7 Pd-NPs loading rate

The Pd-NPs loading rate was examined via the determination of Pd level with inductively coupled plasma mass spectrometry (ICP-MS, 7900, Agilent, California, USA). The weight of both MIL-100(Fe) and Pd@MIL-100(Fe) were quantified. Pd@MIL-100(Fe) was diluted to the concentration of 0.5 mg/mL and digested with the aqua regia at 200°C. Subsequently, the digested Pd@MIL-100(Fe) was dissolved with 1% aqua regia and subjected to the ICP-MS analysis to determine the Pd abundance. Indium (In) was used as the internal control during the ICP-MS analysis (Vojtek *et al.*, 2020).

2.3 Results and discussions

2.3.1 Synthetization and characterization of Pd@MIL-100(Fe)

To prepare the nano sized Pd@MIL-100(Fe), we tired different approaches. First, the hydrothermal synthesis, which is the well-established method for synthesizing various MOFs including MIL-100, was implemented (Simon *et al.*, 2019). The de novo synthesis concept was incorporated to easily make Pd@MIL-100(Fe) in one pot. The various initial molar ratio of Fe:Pd was investigated. After hydrothermal synthesis, the Pd@MIL-100(Fe) particles were examined with DLS. In **Figure 2.3**, all molar ratios tested here exhibited large diameter of over 300 nm and high PDI indicating the hydrothermal synthesis was not suitable for making nano sized MIL-100(Fe) for biomedical applications.

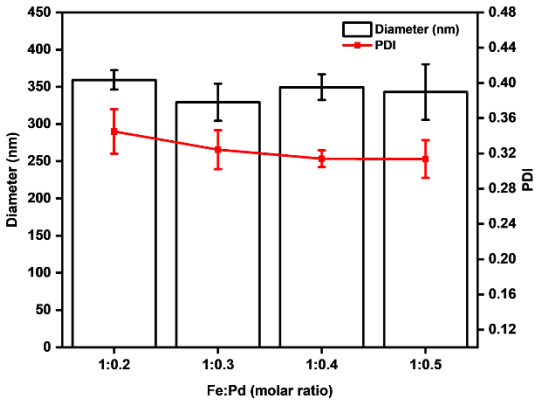

Figure 2.3 The particle size and PDI of Pd@MIL-100(Fe) prepared by hydrothermal synthesis with various Fe:Pd molar ratio. The diameter is shown in bar graph and the PDI in red line.

According to the precious study, the shorter time yet high temperature and high pressure for the growing of MOFs crystal structure is needed to further decrease the particle size of Pd@MIL-100(Fe) (Marquez *et al.*, 2012). Microwave-assisted synthesis was used to achieve rapid heating with the high temperature and high-pressure condition. Similar to the hydrothermal synthesis, we tested for the various molar ratio of Fe:Pd. Interestingly, the results showed that the higher initial amount of Pd was, the smaller particle size was **(Figure 2.4A)**. With the microwave-assisted, the particle size can reach to below 200 nm and PDI less than 0.2 indicating more uniform particle distribution **(Figure 2.4A)** compared to hydrothermal synthesis **(Figure 2.3)**. However, the powder XRD results indicated that although the MIL-100(Fe) was successfully made, the loading of Pd-NPs was very low. The highest initial Pd amount gave the poorest MIL-100(Fe) crystallinity and no observable peak for palladium nanoparticles (Pd-NPs) indicating that Pd ions might interfere the formation of MIL-100(Fe) and probably making free Pd-NPs **(Figure 2.4B)**. The findings from a previous study support this hypothesis showing that Pd-NPs can be formed with microwave-assisted synthesis (Siamaki *et al.*, 2011). Therefore, for preparation of Pd-NPs loaded MIL-100(Fe), the concept of de novo synthesis of Pd@MIL-100(Fe) might not be suitable.

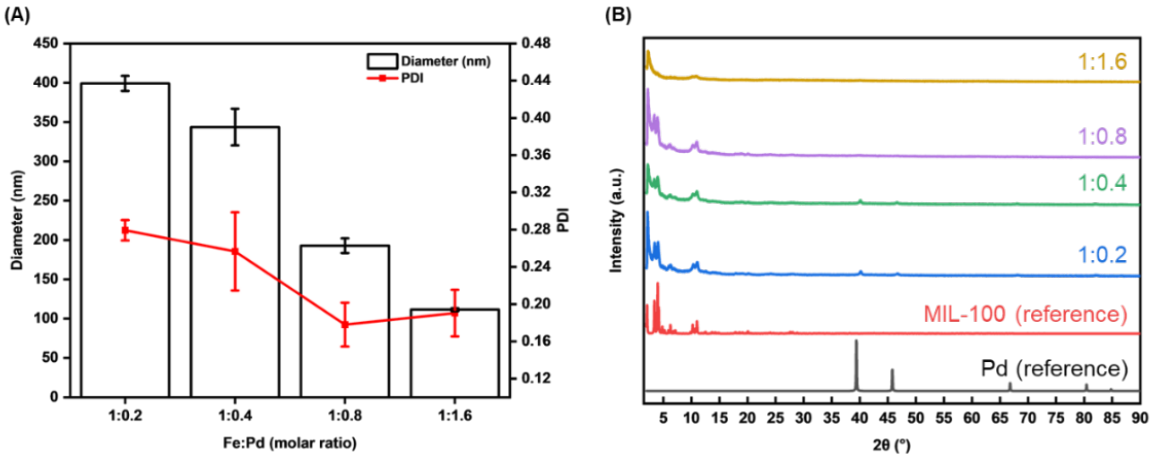

Figure 2.4 Characterization of Pd@MIL-100(Fe) prepared by microwave-assisted synthesis with various Fe:Pd molar ratio. (A) Particle size and PDI of Pd@MIL-100(Fe). The diameter is shown in bar graph and the PDI in red line. (B) Powder XRD peaks of Pd@MIL-100(Fe) with various Fe:Pd molar ratio. The reference peaks for MIL-100(Fe) are shown in red and the reference peaks for Pd are shown in black.

To tackle the issue of low Pd-NPs loading, we separate the synthetization into two steps: synthesis of MIL-100(Fe) and the loading of Pd-NPs. In the previous studies, the porous structure of MOFs such as MIL-100(Fe) was used as the scaffold for the synthesis of biological active nanoparticles and metal nanoparticles (W.-H. Chen *et al.*, 2018; J. W. Wang *et al.*, 2021). The cage-like structure inside the MOFs can not only control the particle size but also capture the synthesized NPs from leaking (J. Yu *et al.*, 2017). Hence, we adopted the in situ synthesis concept of making Pd-NPs inside the MIL-100(Fe). We combined the microwave-assisted synthesis for MIL-100(Fe) preparation and the in situ synthesis of Pd-NPs inside of MIL-100(Fe). First, the parameters of microwave-assisted synthesis were optimized for making nano sized MIL-100(Fe). In the microwave-assisted synthesis for MOFs, the particle size depends on the concentration of initial reactants and the reaction time for the growth of crystal structure (Marquez *et al.*, 2012). Here, we tested four different concentrations including 1, 1/2, 1/6, and 1/8 times of the original concentration (4 mmol of $FeCl_3 \cdot 6H_2O$ and 2.6 mmol of BTC in 20 mL water). The results showed that the1/2 times of the original concentration has the lowest particle size and PDI **(Figure 2.5A)**. Therefore, we selected the1/2 times of the original concentration for the further examinations. Next, various reaction time was also tested including 1, 2, 3, 4, and 6 min. The **Figure 2.5B** indicated a trend of decreasing in particle size as the reaction time became shorter. The smallest particle size around 200 nm was reached in 1, 2, and 3 min of reaction time. Considering the particle size, PDI, and synthesis time, 2 min of reaction time was chosen for further experiments. Based on the initial findings from DLS, we selected the optimized synthesis parameters for the production of MIL-100(Fe) as half of the original concentration (2 mmol of $FeCl_3 \cdot 6H_2O$ and 1.3 mmol of BTC in 20 mL water) and a reaction time of 2 minutes for further exploration.

Subsequently, the Pd-NPs was loaded by the in situ synthesis inside of MIL-100(Fe). In **Figure 2.5C**, the in situ synthesis of Pd-NPs inside of MIL-100(Fe) did not significantly alter the particle size and PDI. To confirm the synthesis of MIL-100(Fe) crystal structure and the loading of Pd-NPs, powder XRD was implemented. Comparing to the reference peaks of MIL-100(Fe) in XRD, the MIL-100(Fe) and Pd@MIL-100(Fe) synthesized in this research showed the similar peaks around 2°-15° confirming the successful synthetization of MIL-100(Fe) **(Figure 2.5D)**. Additionally, by comparing the reference peaks of Pd-NPs in XRD, Pd@MIL-100(Fe) exhibited the similar XRD pattern at approximately 40°, 46°, 66°, 80°, and 85° indicating the successful loading of Pd-NPs inside of the MIL-100(Fe) **(Figure 2.5D)**. Furthermore, the height of the Pd-NPs peaks in Pd@MIL-100 was higher **(Figure 2.5D)** compared to that of the Pd@MIL-100(Fe) prepared by the de novo synthesis **(Figure 2.4B)**. These results indicated the successful preparation of nano sized Pd@MIL-100(Fe) by the two-step preparation developed in this research by the optimized parameters for Pd@MIL-100(Fe) with microwave-assisted synthesis and the concept of in situ synthesis. Considering the low particle size, PDI and short synthesis time, this two-step synthesis protocol for Pd@MIL-100(Fe) was adopted throughout this study for the further experiments.

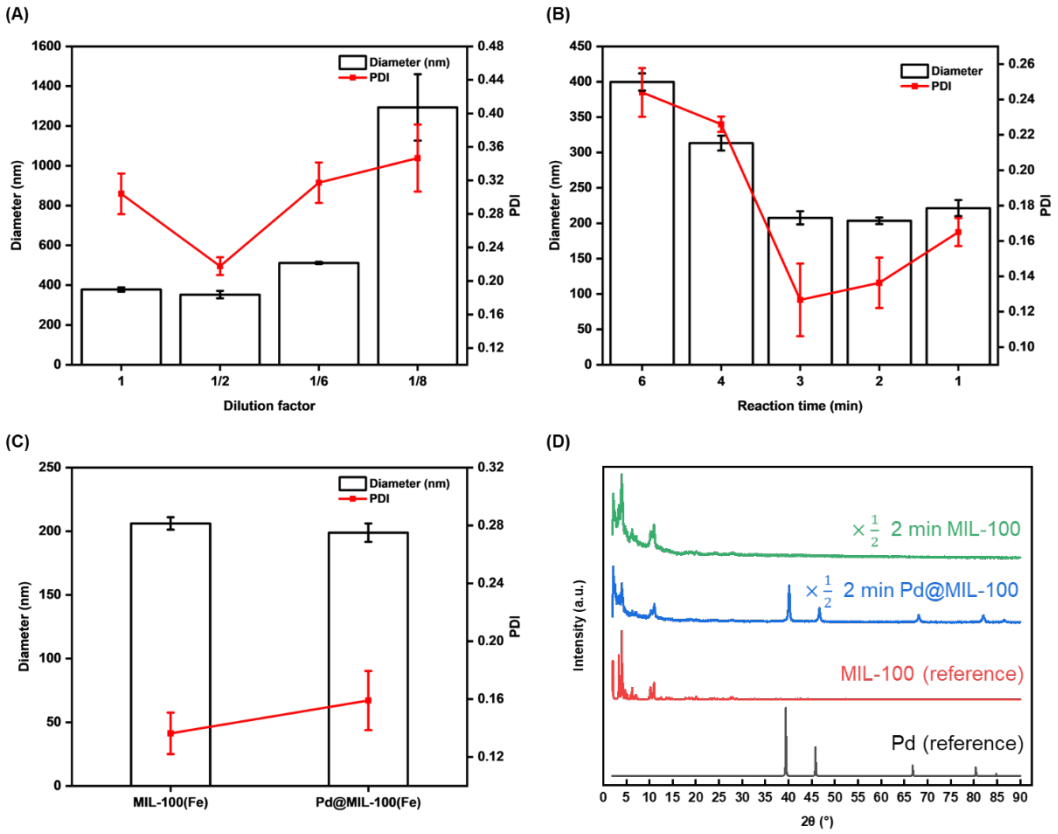

Figure 2.5 Characterization of Pd@MIL-100(Fe) prepared by two-step synthesis. Particle size and PDI of MIL-100(Fe) with various dilution factors (A) and different reaction time (B). (C) Particle size and PDI of MIL-100(Fe) and Pd@MIL-100(Fe). The diameter is shown in bar graph and the PDI in red line. (D) Powder XRD peaks of MIL-100 and Pd@MIL-100(Fe). The reference peaks for MIL-100(Fe) are shown in red and the reference peaks for Pd are shown in black.

2.3.2 Optimization of Pd loading amount

For preparing the Pd@MIL-100(Fe) with best photothermal effect, the initial Pd amount during the in situ synthesis was optimized. We tested the different weight ratio of MIL-100(Fe):Pd during the in situ synthesis of Pd-NPs inside of MIL-100(Fe). After synthetization, the photothermal capability of the Pd@MIL-100(Fe) was examined. Without the loading of Pd-NPs, MIL-100(Fe) showed minimal temperature increases after irradiation of NIR 808 nm light. Similarly, the lowest Pd weight ratio exhibited the negligible photothermal response. There is an increasing trend in photothermal capability as the Pd weight ratio increases **(Figure 2.6)**. However, comparing the weight ratio MIL-100(Fe):Pd, 1:0.125 and 1:0.25, the improvement of photothermal effect by increasing the initial Pd amount reached the plateau **(Figure 2.6)**. With the highest photothermal capability, we chose the weight ratio MIL-100(Fe):Pd of 1:0.25 to be used in the following experiments. In the Pd@MIL-100(Fe) synthesized with weight ratio MIL-100(Fe):Pd of 1:0.25, the temperature reached over 25°C of changes after 5 min of NIR 808 nm light irradiation and the temperature was maintained until the end of the irradiation. This result indicated that Pd@MIL-100(Fe) exhibited favorable photothermal effects with the irradiation of NIR 808 nm light.

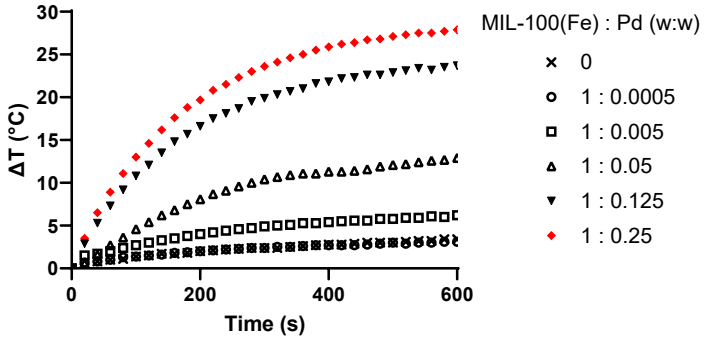

Figure 2.6 Photothermal effects of Pd@MIL-100(Fe) synthesized with different initial weight ratio of MIL-100(Fe):Pd. MIL-100(Fe) was shown with 0. The particles were suspended in 1 mL water with the irradiation of NIR 808 nm light at the energy density of 0.6 W/cm^2. The figure was adopted from S. W. Li *et al.* (2023) with the permission.

To understand the actual Pd loading rate inside of Pd@MIL-100(Fe), ICP-MS was applied to quantify the Pd level of Pd@MIL-100(Fe). The mass of Pd@MIL-100(Fe) denoted as $\boldsymbol{M_{Pd@MIL-100(Fe)}}$ was measured by oven dried the particles. Subsequently, the particles underwent digestion with aqua regia, and the Pd concentration was determined through ICP-MS. The Pd mass was computed utilizing the atomic mass of Pd = 106.42. The mass of Pd inside the Pd@MIL-100(Fe) was represented as $\boldsymbol{M_{Pd}}$ while the initially added Pd mass was shown as $\boldsymbol{M_{Pd\ added}}$. The results showed that about 17.7% the mass of Pd@MIL-100(Fe) was composed of Pd-NPs. After in situ synthesis of Pd-NPs inside of MIL-100(Fe), about 85.9% the mass of initially added Pd was successfully loaded and captured inside the MIL-100(Fe). In accordance with the results in XRD shown in **Figure 2.5D**, the results in **Table 2.1** also confirm the successful loading of Pd-NPs. The Pd-NPs inside of Pd@MIL-100(Fe) provided significant photothermal effects enabling the potential for biomedical applications in the following studies.

Table 2.1 Percentage of Pd loading in MIL-100(Fe).

$\frac{M_{Pd}}{M_{Pd@MIL-100(Fe)}}$	$\frac{M_{Pd}}{M_{Pd\ added}}$
17.7%	85.9%

2.4 Summary

The preparation of Pd@MIL-100(Fe) was accomplished in the two-step process including the microwave-assisted synthesis for nano sized MIL-100(Fe), and followed by the in situ synthesis for making Pd-NPs inside of MIL-100(Fe) porous structure. The parameters for microwave-assisted synthesis were optimized as half of the original concentration (2 mmol of $FeCl_3 \cdot 6H_2O$ and 1.3 mmol of BTC in 20 mL water) with 2 min of reaction time to achieve the 200 nm-sized MIL-100(Fe) with great crystallinity. Additionally, the high loading of Pd-NPs was confirmed with both XRD and ICP-MS. The significant photothermal capability was observed with the as-synthesized Pd@MIL-100(Fe) reaching over 25°C of temperature changes after 5 min of NIR 808 nm light irradiation indicating the sufficient quality and potential for the subsequent experiments.

Chapter 3.

Preparation of Pd@MIL-100/polymer hybrids

3.1 Introduction

One of the main challenges in utilizing MOFs *in vivo* revolves around the release of metal ions and the reactive nature of their surface, leading to potential instability under physiological conditions (P. Horcajada *et al.*, 2010). MIL-100(Fe) stands out as one of the biocompatible MOFs investigated for drug delivery systems. However, its bioactive surface and propensity for aggregation in physiological environments have limited its application. To overcome this challenge, a solution lies in employing a poly(ethylene glycol) (PEG) polymer-based coating, known for its stabilizing effect on surfaces. The application of polymeric coatings presents an appealing avenue to enhance stability (Cabral *et al.*, 2018).

In this chapter, we proposed a PEG-poly(aspartic acid) (PEG-p(Asp))-based block copolymer system to stabilize the surface of MIL-100(Fe), forming MOF/polymer hybrids. The carboxylates present on the side chain of PEG-p(Asp) are capable of complexing with Fe found on the MIL-100(Fe) surface **(Figure 3.1)** (S. Wang *et al.*, 2021). To enhance this complexation, we partially modified the carboxylates with dopamine (Dopa), which contains catechol groups that establish a stronger interaction with Fe on the MIL-100(Fe) surface **(Figure 3.1)** (Porter *et al.*, 2010). Furthermore, we demonstrated the application of the MIL-100/polymer hybrid as a synthesis scaffold for palladium nanoparticles (Pd-NPs) in photothermal therapy, serving as a model delivery platform for cancer theranostics. The synthesis of Pd-NPs loaded MIL-100(Fe) MOF/polymer hybrids involved coating with both PEG-p(Asp) and dopamine-modified PEG-p(Asp) (PEG-p(Asp-Dopa)). Characterization of the resulting hybrids, namely Pd@MIL-100(Fe)/PEG-p(Asp) and Pd@MIL-100(Fe)/PEG-p(Asp-Dopa), was performed using powder XRD, DLS, and transmission electron microscopy (TEM). Additionally, tests were conducted to evaluate the serum stability of Pd@MIL-100(Fe)/polymer hybrids. Finally, the photothermal conversion efficiency and photothermal stability of both Pd@MIL-100(Fe) and its polymer hybrids was determined.

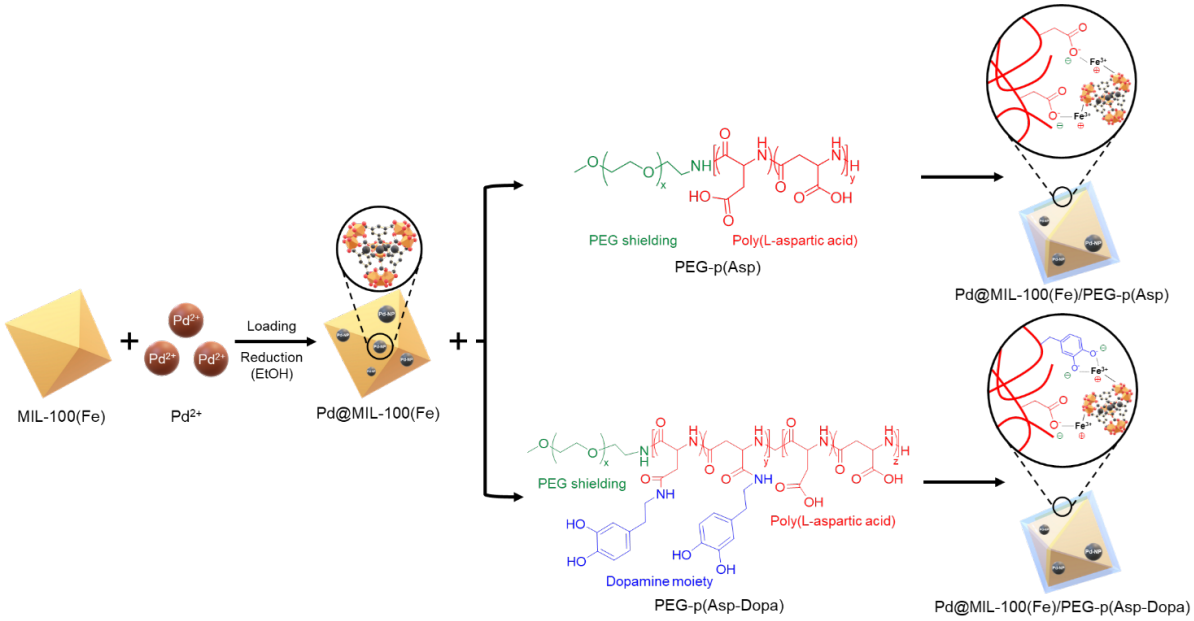

Figure 3.1 The design of Pd@MIL-100(Fe)/polymer hybrids. The figure was adopted from S. W. Li *et al.* (2023) with the permission.

3.2 Materials and methods

3.2.1 Materials

Sigma Aldrich (Missouri, USA) provided dopamine hydrochloride, while NOF Corporation (Tokyo, Japan) supplied *α*-methoxy-*ω*-amino-poly(ethylene glycol) (MeO-PEG-NH2; Mw = 12,000 g mol−1) and β-benzyl L-aspartic acid N-carboxyanhydride (BLA-NCA). Tokyo Chemical Industry Co. Ltd. (Tokyo, Japan) supplied dichloromethane (CH2Cl2) and 4-(4,6-dimethoxy-1,3,5-triazin-2-yl)-4-methylmorpholinium chloride (DMTMM). Additionally, ThermoFisher Scientific (Waltham, USA) provided phosphate-buffered saline (PBS).

3.2.2 Synthesis of poly(ethylene glycol)-poly(L-aspartic acid)

The synthesis of poly(ethylene glycol)-poly(L-aspartic acid) (PEG-p(Asp)) was conducted with a modified procedure based on previously established methods (P. W. Chen *et al.*, 2023). PEG-p(Asp) was synthesized through the ring-opening polymerization of BLA-NCA in an aqueous environment (Grazon *et al.*, 2020). Initially, MeO-PEG-NH_2 (500 mg, Mw = 12,000) was dissolved in 10 mL 50 mM $NaHCO_3$ solution (pH = 8.5). Since the targeting degree of polymerization is set to 40, to this solution, BLA-NCA (500 mg) was added while stirring vigorously within an ice bath. The reaction mixture underwent a 12-hour incubation period, after which dialysis (molecular weight cut-off (MWCO) = 6,000-8,000) against water was performed before lyophilization. The lyophilized material was reconstituted in dichloromethane and precipitated using diethyl ether to obtain purified PEG-poly(benzyl-L-aspartate) (PEG-pBLA). The resulting precipitate was vacuum-dried for 3 hours. Verification of the polymerization process was conducted using proton nuclear magnetic resonance (^{1}H NMR) (JNM ECS-400, JEOL Ltd., Tokyo, Japan) in DMSO-d_6 at 80°C. Subsequently, PEG-pBLA was dissolved in a 10 mL 0.5 N NaOH solution and stirred for 1 hour in a 37°C water bath to remove the benzyl protection group. The resulting mixture underwent purification by

dialysis (MWCO = 6,000-8,000) against pure water, followed by lyophilization to yield PEG-p(Asp) in the form of a white, fluffy powder. Characterization of PEG-p(Asp) was conducted using ^{1}H-NMR in D_2O at room temperature. The synthesis scheme is illustrated in **Figure 3.2**.

3.2.3 Modification of dopamine on PEG-p(Asp)

By coupling with DMTMM, the modification of PEG-p(Asp) with dopamine (Dopa) was achieved (D'Este *et al.*, 2014). Oxygen-free water, prepared by subjecting water to low-pressure sonication for 10 minutes, was employed to prevent the self-polymerization of dopamine. Dopamine hydrochloride was subsequently added to 20 mL of oxygen-free water at 3 equivalents to p(Asp), and an excess of DMTMM coupling reagent was introduced to the p(Asp). The resulting mixture underwent stirring for 6 hours and was then purified by dialysis (MWCO = 6,000-8,000) against oxygen-free water. Following lyophilization, PEG-p(Asp-Dopa) was obtained as a white fluffy powder. Successful coupling was confirmed through 1H-NMR analysis in both DMSO-d_6 and D_2O. The synthesis scheme is illustrated in **Figure 3.2**.

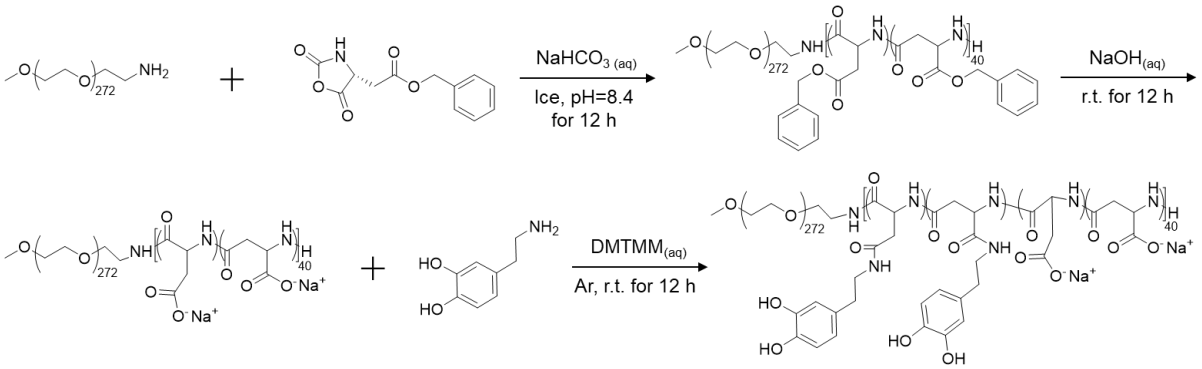

Figure 3.2 The synthesis scheme of PEG-p(Asp) and PEG-p(Asp-Dopa) block copolymers. The figure was adopted from S. W. Li *et al.* (2023) with the permission.

3.2.4 Synthesis of Pd@MIL-100(Fe)/polymer hybrids

Pd@MIL-100(Fe)/polymer hybrids, comprising Pd@MIL-100(Fe)/PEG-p(Asp) and Pd@MIL-100(Fe)/PEG-p(Asp-Dopa), were synthesized through a refluxing process. Each polymer was dissolved in 10 mL of a 70% ethanol aqueous solution. Subsequently, Pd@MIL-100(Fe) with a concentration of 1 mg/mL was blended with the respective polymer solutions. The Pd@MIL-100(Fe) and polymers were mixed at weight ratio Pd@MIL-100(Fe):polymers of 1:2. After stirring for 5 min, the mixture was subjected to refluxing at 80°C for 12 h. Subsequently, the Pd@MIL-100(Fe)/polymer hybrids were obtained by centrifugation at 16,000 x g and washed once with ethanol followed by water twice. The final Pd@MIL-100(Fe)/polymer hybrids products were obtained as black-colored solutions.

3.2.5 Crystallinity characterization with powder X-ray diffraction

The crystalline structure of Pd@MIL-100(Fe), Pd@MIL-100(Fe)/PEG-p(Asp), and Pd@MIL-100(Fe)/PEG-p(Asp-Dopa) was verified using powder X-ray diffraction (XRD) with a MiniFlex600/PTN instrument (Rigaku, Tokyo, Japan). The final products of Pd@MIL-100(Fe) and Pd@MIL-100(Fe)/polymer hybrids underwent oven-drying and were then placed onto the sample holder for XRD analysis. The X-ray settings were 40 kV and 15 mA. The scanning mode employed was 2θ/θ, with a scanning range from 2° to 90° and a step size of 0.01°. The raw XRD data were processed using Mercury software (2021.3, CCDC, Boston, USA). The standard XRD patterns of MIL-100(Fe) (ID: 7102029) was obtained from Crystallography Open Database and Pd-NPs (ID: mp-2) were obtained from The Materials Project (Patricia Horcajada *et al.*, 2007; Jain *et al.*, 2013).

3.2.6 Characterization of particle size

The hydrodynamic diameter of Pd@MIL-100(Fe)/PEG-p(Asp) and Pd@MIL-100(Fe)/PEG-p(Asp-Dopa) was determined using dynamic light scattering (DLS) with the Zetasizer Nano-ZS instrument (Malvern Panalytical, Worcestershire, UK). The final products of Pd@MIL-100(Fe)/polymer hybrids were dispersed in deionized water at an approximate concentration of 0.1 mg/mL and introduced into a low-volume quartz cuvette (ZEN2112). Measurements were conducted at 25°C with a 50 mW frequency doubled DPSS Nd:YAG laser (λ=532 nm) at a detection angle of 173°. The average diameter and Polydispersity Index (PDI) were calculated using the cumulant method to describe the particle size characteristics of Pd@MIL-100(Fe)/PEG-p(Asp) and Pd@MIL-100(Fe)/PEG-p(Asp-Dopa).

3.2.7 Characterization of surface charge

The surface charge of MIL-100(Fe), Pd@MIL-100(Fe), and Pd@MIL-100(Fe)/polymer hybrids was assessed through ζ-potential measurements using a Zetasizer Nano-ZS instrument (Malvern Panalytical, Worcestershire, UK). The particles were diluted to a concentration of 0.1 mg/mL in deionized water and introduced into folded capillary zeta cells (DTS1070) with a volume of 1 mL. The ζ-potential was recorded at 25°C with default settings.

3.2.8 Characterization with transmission electron microscopy

The morphology of Pd@MIL-100(Fe)/polymer hybrids was examined using transmission electron microscopy (TEM). Before the TEM analysis, both Pd@MIL-100(Fe)/PEG-p(Asp) and Pd@MIL-100(Fe)/PEG-p(Asp-Dopa) were washed once with water and then diluted to a concentration of approximately 0.05 mg/mL with deionized water. The resulting solution was deposited onto a 400-mesh copper grid. TEM images were captured using JEM-1400 (JEOL, Tokyo, Japan).

3.2.9 Characterization with energy dispersive spectroscopy

Elemental mapping analysis of Pd@MIL-100(Fe)/polymer hybrids was conducted using energy dispersive spectroscopy (EDS). Prior to the EDS analysis, both Pd@MIL-100(Fe)/PEG-p(Asp) and Pd@MIL-100(Fe)/PEG-p(Asp-Dopa) were washed once with water and then diluted to a concentration of approximately 0.05 mg/mL with deionized water. The resulting solution was deposited onto a 400-mesh copper grid. EDS analysis was carried out using JEM-2100F (JEOL Ltd., Tokyo, Japan).

3.2.10 Composition examination

To analyze the composition of Pd@MIL-100(Fe) and Pd@MIL-100(Fe)/polymer hybrids, thermogravimetric analysis (TGA) was performed using the EXSTAR TG/DTA 6200 thermogravimetric analyzer (Hitachi High-Tech Science, Tokyo, Japan) under a nitrogen atmosphere. The TGA procedure involved heating from 30°C to 550°C at a rate of 5°C/min with smart temperature ramping.

3.2.11 Analysis of Photothermal capability

Solutions containing Pd@MIL-100(Fe) and Pd@MIL-100(Fe)/polymer hybrids (0.5 mg/mL) were prepared and loaded into 2.0 mL PE microtubes with 1 mL of each solution. The solutions were exposed to NIR 808 nm light with a power of 1.5 J/s for 600 s, followed by natural cooling. Temperature variations were monitored using a digital thermometer (TM-947SD, Lutron, Taipei, Taiwan) connected to a small Pt-100 thermo-resistor inside the tube. The photothermal conversion efficiency (η) was determined using a macroscopic model that accounts for the heating of the system, including particles, solution, and container (Breitenborn *et al.*, 2019). The model includes the heat generation and the dissipation. The change of temperature during NIR irradiation is represented by the energy balance equation **(Equation**

3.1):

$$\sum_i m_i C_i \frac{dT}{dt} = E_{abs} - E_{loss} \quad (3.1)$$

where E_{abs} is the heat generation by the Pd-NPs in the MIL-100(Fe), E_{loss} is the heat dissipation, T is the temperature, and t is the time. Additionally, m_i and C_i are the mass and specific heat capacity of each component i in the system (i.e., Pd@MIL-100(Fe) or Pd@MIL-100(Fe)/polymer hybrids, deionized water, and 2.0 mL PE micro tubes). To represent the E_{abs} and E_{loss}, the energy absorption and dissipation in **Equation 3.1** can be expressed as follows:

$$E_{abs} = P(1 - 10^{-A_\lambda})\eta \quad (3.2)$$

$$E_{loss} = hS[T(t) - T_0] \quad (3.3)$$

where P is the NIR laser power, A_λ is the absorbance of the solution at the laser wavelength, η is the photothermal conversion efficiency, h is the heat transfer coefficient, S is the surface area of the solution, and T_0 is the ambient temperature. By substitution E_{abs} and E_{loss} into **Equation 3.1**, it can be rewritten as follows:

$$\frac{dT}{dt} = \frac{P(1-10^{-A_\lambda})\eta}{\sum_i m_i C_i} - \frac{hS}{\sum_i m_i C_i}[T(t) - T_0] \quad (3.4)$$

Here we define the two constant A and B as follow:

$$A = \frac{P(1-10^{-A_\lambda})\eta}{\sum_i m_i C_i} \quad (3.5)$$

$$B = \frac{hS}{\sum_i m_i C_i} \quad (3.6)$$

where A represents the rate of energy absorption while B indicates the rate of heat dissipation. By substituting A and B into **Equation 3.4**, the equation can be rewritten as:

$$\frac{dT}{dt} = A - \mathrm{B}[T(t) - T_0] \quad (3.7)$$

By integrating the **Equation 3.7** over time (from 0 to t), the temperature changes from an arbitrary initial temperature value $T_{initial}$ can be represented as follows:

$$T(t) = T_0 + \frac{A}{B}(1 - e^{-Bt}) + (T_{initial} - T_0)e^{-Bt} \quad (3.8)$$

To calculate the photothermal conversion efficiency, time constant method was used (Breitenborn *et al.*, 2019). The value of B, heat dissipation rate, was obtained by fitting **Equation 3.8** to the cooling phase curve with $A = 0$ and $T_{initial} = T_{Max}$ as constraints, where T_{Max} is the highest temperature measured just after the NIR 808 nm laser irradiation. Then, the value of A, energy absorption rate, was acquired by fitting **Equation 3.8** to the curve of heating phase with B and $T_{initial} = T_0$ as constants where T_0 is the temperature measured before NIR 808 nm laser irradiation. For the three solutions including Pd@MIL-100(Fe), and two Pd@MIL-100(Fe)/polymer hybrids examined in this research, the mass of MOF particles was neglectable compared to that of the PE tube and water. The heat capacity of water (4.18 $Jg^{-1}\ K^{-1}$) is much higher than that of PE (1.33 $Jg^{-1}\ K^{-1}$). Therefore, the mass and heat capacity of the entire solutions can be assumed as water. Furthermore, the absorbance values (A_λ) at the NIR laser wavelength (808 nm) were measured using a multi-well plate reader (Spark, Tecan, Männedorf, Switzerland) with the following values: 0.274 for Pd@MIL-100(Fe), 0.294 for Pd@MIL-100(Fe)/PEG-p(Asp), and 0.285 for Pd@MIL-100(Fe)/PEG-p(Asp-Dopa). The photothermal conversion efficiency (η) can be calculated using the following equation:

$$\eta = \frac{A\sum_i m_i C_i}{P(1-10^{-A_\lambda})} \quad (3.9)$$

The photothermal performance of the MOF/polymer hybrids at varying concentrations was assessed by dispersing them in 100 µL of water at concentrations of 0.1, 0.3, and 0.5 mg/mL. An 808 nm NIR laser was employed at an energy density of 0.6 W/cm^2, and the temperature was recorded every 5 seconds for a duration of 10 minutes using an automated digital thermometer (TM-947SD, Lutron, Taipei, Taiwan).

3.2.12 Photothermal stability analysis

The photothermal stability of the MOF/polymer hybrids was evaluated by examining their ability to consistently heat the solution through 5 cycles. Pd@MIL-100(Fe) and MOF/polymer hybrids were suspended in 2 mL of water at a concentration of 0.5 mg/mL in 2 mL microtubes. Temperature changes were recorded every 5 seconds using a digital thermometer (TM-947SD, Lutron, Taipei, Taiwan) attached to a small Pt-100 thermo-resistor inside the tube. Subsequently, the MOF solutions were exposed to NIR 808 nm light (0.6 W/cm^2) for 5 minutes and allowed to cool naturally for 10 minutes. This heating and cooling cycle was repeated 5 times, and the photothermal stability was confirmed by assessing the photothermal capability after the 5 repeated cycles.

3.2.13 Aqueous stability analysis

The stability of MIL-100(Fe) and Pd@MIL-100(Fe)/polymer hybrids was assessed based on average hydrodynamic diameter and PDI using dynamic light scattering (DLS). Initially, short-term stability under various solvent conditions was investigated. The particles were washed once with water and then resuspended at a concentration of 0.5 mg/mL in water, PBS with 35 mg/mL BSA, or DMEM containing 10% FBS. The suspensions were incubated in a 37°C incubator for 6 hours, and hydrodynamic diameter and PDI were monitored at 0 hours, 1 hour, 2 hours, 3 hours, and 6 hours. Additionally, long-term stability analysis of MIL-100(Fe) and Pd@MIL-100(Fe)/polymer hybrids was conducted in PBS with 10% FBS over 7 days. After washing with water, the particles were resuspended at a concentration of 0.5 mg/mL in PBS with 10% FBS and incubated at 37°C for 7 days. Both size and PDI were monitored using DLS to assess stability.

3.3 Results and discussions

3.3.1 Preparation of polymer

To provide the ability to complex with MIL-100(Fe), PEG-p(Asp) block copolymer was designed. The carboxylate on the aspartic acid can complex with the free Fe on the surface of MIL-100(Fe). To prepare the PEG-p(Asp), first the PEG-pBLA was synthesized with ring opening polymerization in aqueous phase according to the previous study (Grazon *et al.*, 2020). The degree of polymerization of PEG-pBLA was assessed with ^{1}H-NMR in DMSO-d_6. The NMR peaks in the range of 7-8 ppm indicted the protons on the benzyl protection groups while the peaks at about 3.5 ppm represented the protons in the PEG **(Figure 3.3A)**. By normalization of the peak area between benzyl protection groups and PEG, we can calculate that about 40 units of BLA was presented per PEG molecule. After deprotection, PEG-p(Asp) was obtained. PEG-p(Asp) is not soluble in DMSO, but it dissolved easily in water. Hence, the PEG-p(Asp) was examined with ^{1}H-NMR in D_2O. The peaks for the protection groups (7-8 ppm) disappeared in PEG-p(Asp) indicating the successful removal of the benzyl protection groups **(Figure 3.3B)**. In order to enhance the bonding strength between the polymer and MOFs, PEG-p(Asp) was modified by incorporating dopamine, which possesses catechol groups capable of forming strong complexes with Fe ions (Porter *et al.*, 2010). The dopamine was conjugated to the carboxyl groups of aspartic acid. The yielding PEG-p(Asp-Dopa) was examined with ^{1}H-NMR in both DMSO-d_6 and D_2O. The peaks shown around 7-8 ppm represented the protons on the catechol groups of dopamine indicating the successful conjugation of PEG-p(Asp-Dopa) **(Figure 3.3C and D)**. After integrating the peak, about 24 units of Dopa were presented per PEG indicating that about 60% of carboxylate was conjugated with Dopa. The synthesized PEG-p(Asp) and PEG-p(Asp-Dopa) were utilized in the fabrication of Pd@MIL-100(Fe)/polymer hybrids.

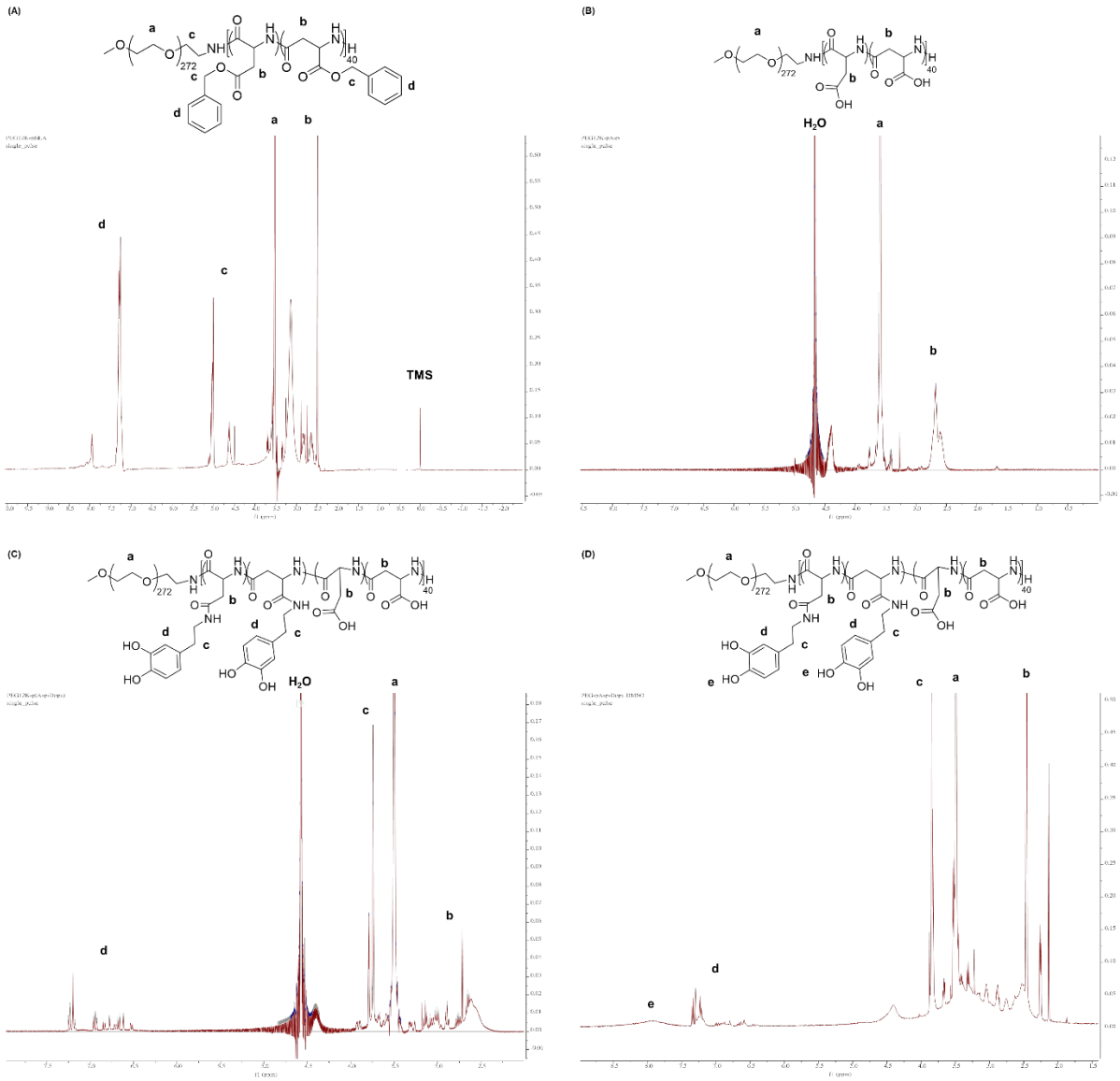

Figure 3.3 The ^{1}H-NMR spectrum for (A) PEG-pBLA measured in DMSO-d_6 at 80°C, (B) PEG-p(Asp) measured in D_2O at 25°C, (C) PEG-p(Asp-Dopa) measured in D_2O at 25°C, and (D) PEG-p(Asp-Dopa) measured in DMSO-d_6 at 80°C. The figure was adopted from S. W. Li *et al.* (2023) with the permission.

3.3.2 Characterization of Pd@MIL-100/polymer hybrids

The Pd@MIL-100(Fe)/polymer hybrids were prepared with refluxing. To analyze the crystallinity of the MOFs and MOFs/polymer hybrids that synthesized here, we implemented powder XRD. In **Figure 3.4**, all the MOFs that we synthesized presented the similar pattern with the MIL-100(Fe) reference peaks indicating that both loading of Pd-NPs and the formation of polymer hybrids did not alter the crystal structure of MIL-100(Fe). Additionally, the reference peaks of Pd-NPs were also observed in both Pd@MIL-100 and Pd@MIL-100/polymer hybrids indicating the successful loading of Pd-NPs. The coating of polymers onto Pd@MIL-100(Fe) did not affect the structure of Pd@MIL-100(Fe) indicating the suitability for the subsequent experiments.

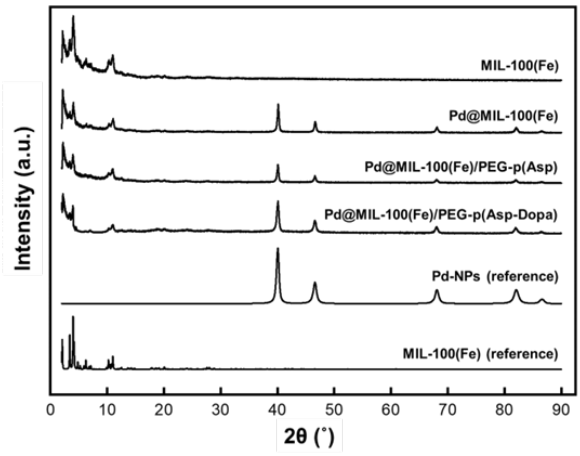

Figure 3.4 The powder X-ray diffraction (XRD) patterns of MIL-100(Fe), Pd@MIL-100(Fe), Pd@MIL-100(Fe)/PEG-p(Asp), and Pd@MIL-100(Fe)/PEG-p(Asp-Dopa). The reference peaks corresponding to Pd nanoparticles (Pd-NPs) and MIL-100(Fe) are indicated in the bottom two lines for comparison. The figure was adopted from S. W. Li *et al.* (2023) with the permission.

For a comprehensive understanding of MOFs and MOF/polymer hybrids, we conducted particle size distribution analysis using DLS first on different length of p(Asp) and PEG. The results showed that both 40 and 60 units of Asp exhibited a similar size distribution **(Figure 3.5A)**. Therefore, we chose 40 units of Asp for the following experiments. Additionally, the various lengths of PEG, including 12K and 20K, with 40 units of Asp, also showed a similar size distribution. Hence, we chose 40 units of Asp with a PEG length of 12K for the following experiments **(Figure 3.5B)**. Subsequently, an analysis of the size distribution of MIL-100(Fe), Pd@MIL-100(Fe), and Pd@MIL-100(Fe)/polymer hybrids, revealed smaller size distributions in the Pd@MIL-100(Fe)/polymer hybrids **(Figure 3.6)**. While the loading of Pd-NPs had no impact on the diameter, the formation of Pd@MIL-100(Fe)/polymer hybrids notably reduced particle size **(Figure 3.7)**. Particularly, Pd@MIL-100/PEG-p(Asp-Dopa) exhibited the smallest particle size. Accordingly, previous research has indicated that MIL-100(Fe) is prone to aggregation and larger sizes in the absence of surface protection (P. Horcajada *et al.*, 2010). The sizes of the two hybrids including Pd@MIL-100(Fe)/PEG-p(Asp) and Pd@MIL-100(Fe)/PEG-p(Asp-Dopa) measured at 170 ± 7 nm and 153 ± 6 nm, respectively, were smaller compared to Pd@MIL-100(Fe) at 209 ± 5 nm **(Table 3.1)**. The observed decrease in hydrodynamic diameters can be attributed to the formation of a PEG shield, effectively impeding inter-particle aggregation (Akbarzadehlaleh *et al.*, 2021).

To verify the surface protection conferred by PEG block copolymers, we conducted the measurements of the surface charge, known as zeta (ζ)-potential. The ζ-potential distributions revealed a clear shift towards the positive direction (right) for the Pd@MIL-100(Fe)/polymer hybrids compared to Pd@MIL-100(Fe) **(Figure 3.8)**. The surface charge of MIL-100(Fe) and Pd@MIL-100(Fe) was approximately -39.2 ± 0.7 mV and -28.3 ± 0.7 mV, respectively, suggesting that the in situ synthesis of Pd-NPs influenced the surface charge of MIL-100(Fe) **(Table 3.1)**. In contrast, both hybrids including Pd@MIL-100(Fe)/PEG-p(Asp) and Pd@MIL-

100(Fe)/PEG-p(Asp-Dopa) exhibited a ζ-potential of -17.0 ± 0.4 mV and -17.3 ± 0.4 mV, respectively, which are even lower than that of Pd@MIL-100(Fe) **(Table 3.1)**. The reduced ζ-potential in Pd@MIL-100(Fe)/polymer hybrids compared to Pd@MIL-100(Fe) indicates the presence of a PEG shielding effect (Shi *et al.*, 2021).

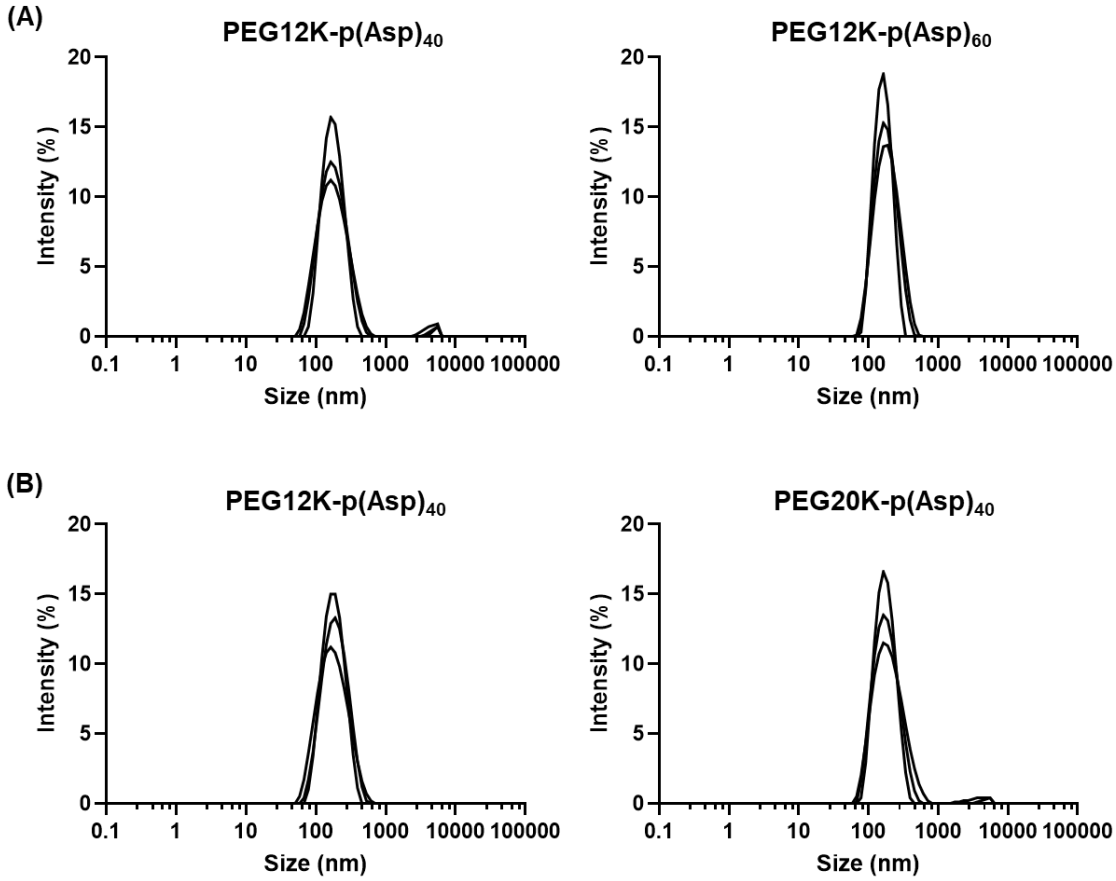

Figure 3.5 The size distribution of Pd@MIL-100(Fe)/polymer hybrids coated with different length of (A) p(Asp) and (B) PEG.

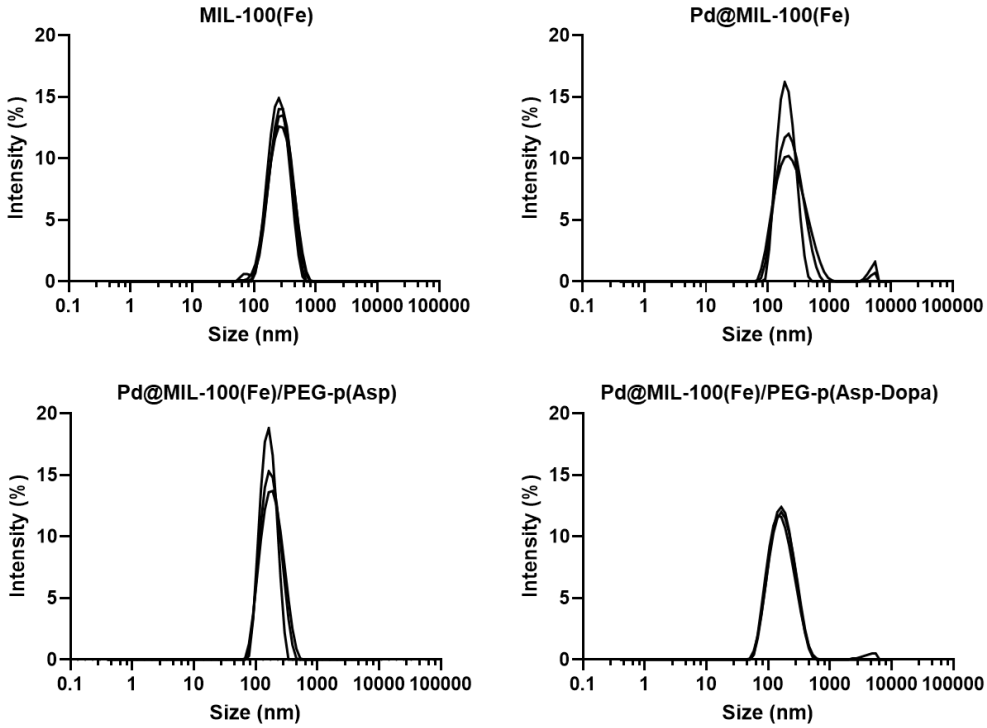

Figure 3.6 The size distribution of MIL-100(Fe), Pd@MIL-100(Fe), Pd@MIL-100(Fe)/PEG-p(Asp), and Pd@MIL-100(Fe)/PEG-p(Asp-Dopa). The data was sown as intensity percentage. The figure was adopted from S. W. Li *et al.* (2023) with the permission.

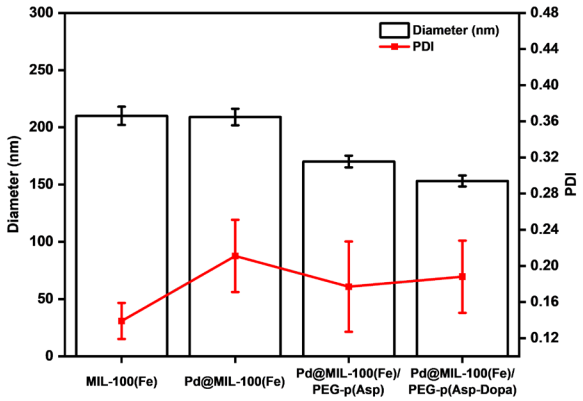

Figure 3.7 The hydrodynamic diameter and PDI of MIL-100(Fe), Pd@MIL-100(Fe), Pd@MIL-100(Fe)/PEG-p(Asp), and Pd@MIL-100(Fe)/PEG-p(Asp-Dopa). The diameter is shown in bar graph and the PDI in red line.

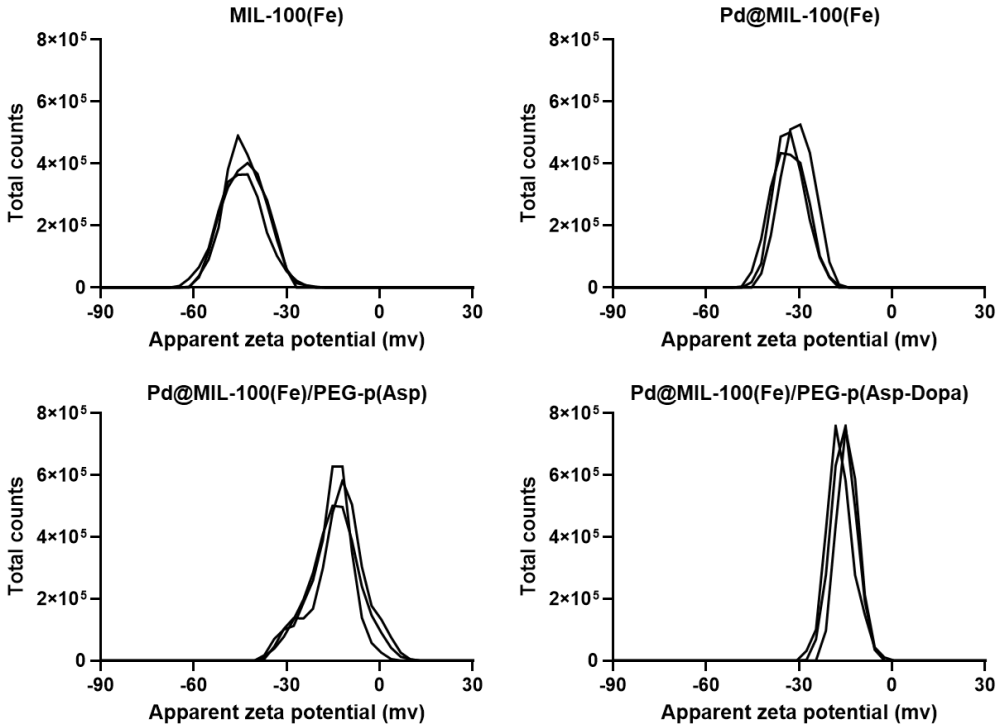

Figure 3.8 The ζ-potential distribution of MIL-100(Fe), Pd@MIL-100(Fe), Pd@MIL-100(Fe)/PEG-p(Asp), and Pd@MIL-100(Fe)/PEG-p(Asp-Dopa).

Table 3.1 Size and ζ-potential of MIL-100(Fe), Pd@MIL-100(Fe), Pd@MIL-100(Fe)/PEG-p(Asp), and Pd@MIL-100(Fe)/PEG-p(Asp-Dopa) (n = 3). The table was adopted from S. W. Li *et al.* (2023) with the permission.

Particles	Diameter (nm) ± SD	PDI ± SD	ζ-Potential (mV) ± SD
MIL-100(Fe)	210 ± 8	0.139 ± 0.02	-39.2 ± 0.7
Pd@MIL-100(Fe)	209 ± 5	0.211 ± 0.04	-28.3 ± 0.7
Pd@MIL-100(Fe)/PEG-p(Asp)	170 ± 7	0.177 ± 0.05	-17.0 ± 0.4
Pd@MIL-100(Fe)/PEG-p(Asp-Dopa)	153 ± 6	0.188 ± 0.04	-17.3 ± 0.4

With the data from hydrodynamic diameter and ζ-potential, it was known that the surface protection of Pd@MIL-100(Fe) by polymers can decrease the particle size by forming the PEG shielding. However, it was still unknown that the reason why PEG shielding could decrease the particle size of Pd@MIL-100(Fe). Here, TEM was used to reveal the morphology of these MOF and MOF/polymer hybrid particles to gain insights into the morphological changes after surface protection. **Figure 3.9** showed that in consistent to the previous research, Pd@MIL-100(Fe) exhibited a highly aggregated morphology (P. Horcajada *et al.*, 2010). After surface protection by PEG-p(Asp) and PEG-p(Asp-Dopa) the degree of aggregation was significantly reduced. The size of Pd@MIL-100(Fe)/polymer hybrids shown in **Figure 3.9** exhibited the similar particle size measured with DLS in aqueous condition while the Pd@MIL-100(Fe) formed larger clumps in TEM images indicating that PEG shielding provided by the PEG-p(Asp) and PEG-p(Asp-Dopa) has the potential to prevent the aggregation. Furthermore, to examine the composition of the Pd@MIL-100(Fe)/polymer hybrids, we implemented TEM-EDS method to perform element mapping analysis. The results showed that the C, O, and Fe elements were colocalized indicating the structure of MIL-100(Fe) and polymers **(Figure 3.10)**. The Pd element was found to concentrate inside of Fe element confirming the successful loading of Pd-NPs that was in accordance with the XRD results **(Figure 3.4 and Figure 3.10)**.

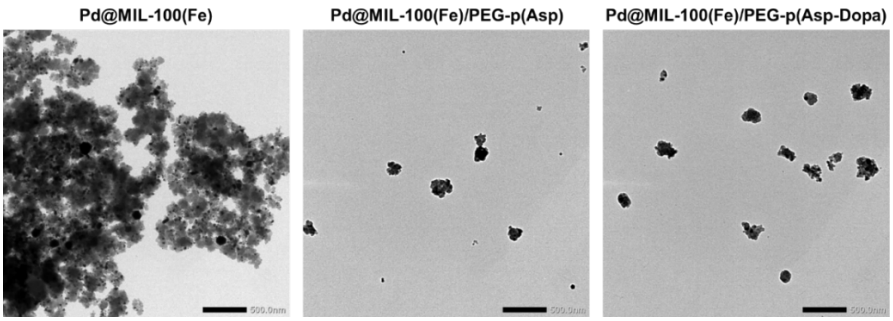

Figure 3.9 Representative TEM images of Pd@MIL-100(Fe), Pd@MIL-100(Fe)/PEG-p(Asp), and Pd@MIL-100(Fe)/PEG-p(Asp-Dopa) taken with the scale at 500 nm. The figure was adopted from S. W. Li *et al.* (2023) with the permission.

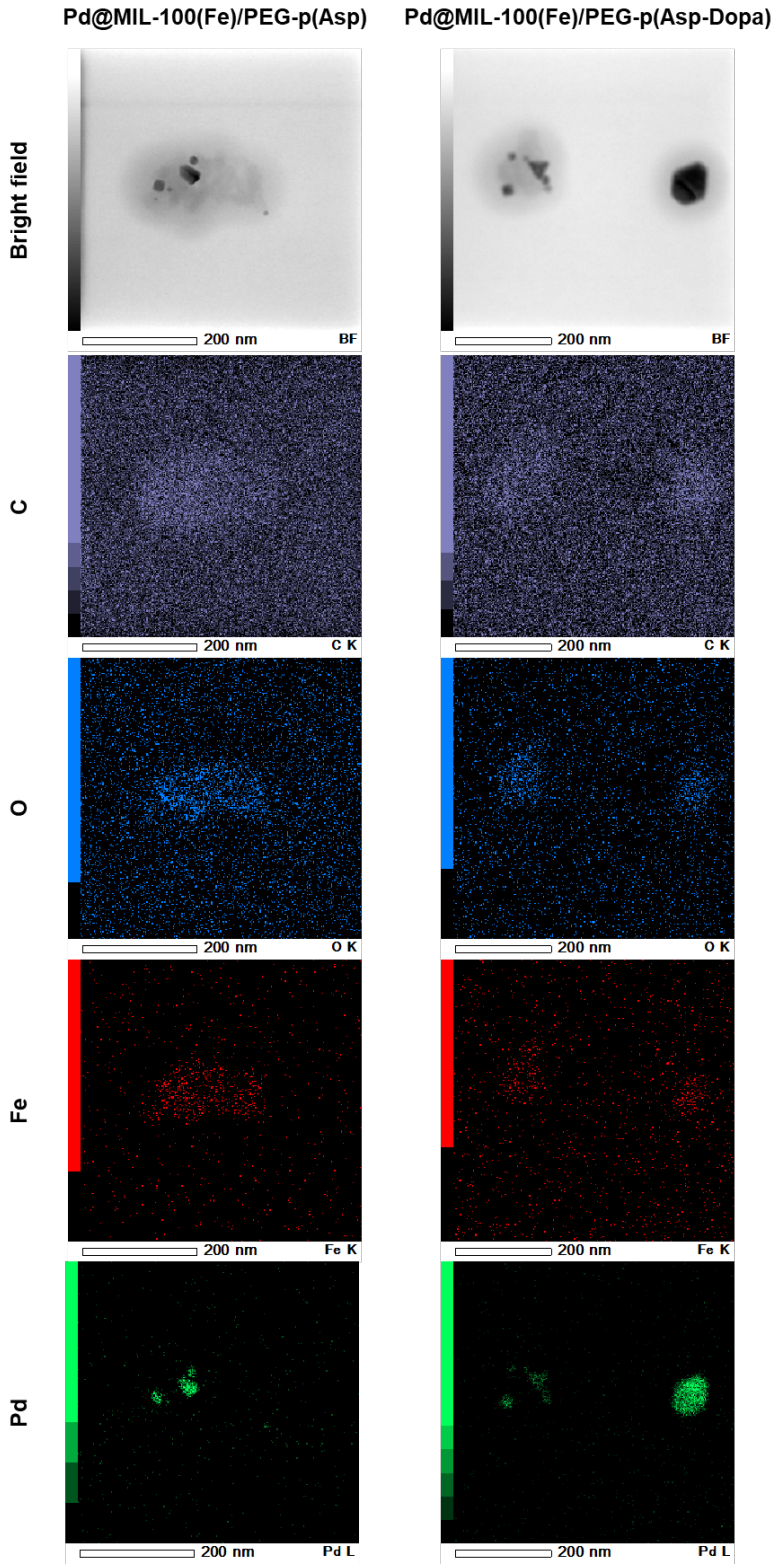

Figure 3.10 TEM-EDS element mapping analysis of Pd@MIL-100(Fe)/PEG-p(Asp), and Pd@MIL-100(Fe)/PEG-p(Asp-Dopa) for C, O, Fe, and Pd elements. C is shown in pruple, O in blue, Fe in red, and Pd in green. The figure was adopted from S. W. Li *et al.* (2023) with the permission.

To gain a thorough understanding of the composition of both Pd@MIL-100(Fe) and the MOF/polymer hybrids, we utilized thermal gravimetric analysis (TGA). The findings from **Table 2.1** by ICP-MS unveiled a Pd content of 17% within Pd@MIL-100(Fe) relative to its weight, constituting approximately 86% of the initial feeding amount. This data confirmed the efficient incorporation of Pd-NPs within the MOF structure. Furthermore, our TGA results demonstrated a similarity between the TGA curve of our microwave-assisted synthesized MIL-100(Fe) and the conventionally prepared MIL-100(Fe). The curve displayed the first drop around 300°C, indicating structural decay of the MOF, followed by a subsequent drop at 400°C, attributed to the iron reduction (Simon *et al.*, 2019). The introduction of Pd-NPs within the MIL-100(Fe) slightly altered its TGA curve, presenting a decay at a lower temperature. This shift could be attributed to potential interference caused by the Pd-NPs within the MOF structure, affecting the degradation process **(Figure 3.11A)**. Upon comparing the observed weight loss in the TGA curves of MIL-100(Fe) and Pd@MIL-100(Fe), the Pd content was estimated to be approximately 12%, which closely aligns with the Pd content quantified by ICP-MS. This consistency across analytical techniques confirms the accuracy of the Pd content determination. Furthermore, the TGA analysis revealed that the weight loss attributed to the polymer coating of both Pd@MIL-100(Fe)/polymer hybrids approximated 8% in weight within the Pd@MIL-100(Fe)/polymer hybrids. **(Figure 3.11A)**. In **Figure 3.11B**, BTC showed a huge drop of weight at about 300°C. While the PEG started to decay at about 380°C, the decay of p(Asp) and p(Asp-Dopa) appeared at early stage of heating around 200°C and 270°C, respectively **(Figure 3.11B)**. This data corroborates the presence and proportion of the polymer coating on the hybrid structures.

The successful preparation of Pd@MIL-100(Fe) and Pd@MIL-100(Fe)/polymer hybrids has been verified through a range of analytical methods. These analyses, including XRD, DLS, ζ-potential, and elemental mapping, highlight their robust crystalline structure and effective loading of Pd-NPs. TEM imaging has provided compelling visual evidence, revealing notable enhancements in particle morphology. This improvement signifies a reduced level of aggregation, a positive outcome following the implementation of protective surface measures. Furthermore, the TGA results serve as a dual confirmation, affirming the successful synthesis of Pd@MIL-100(Fe)/polymer hybrids. These results provided the understanding of the particles' morphology and composition. Such validation lays a groundwork for subsequent experiments.

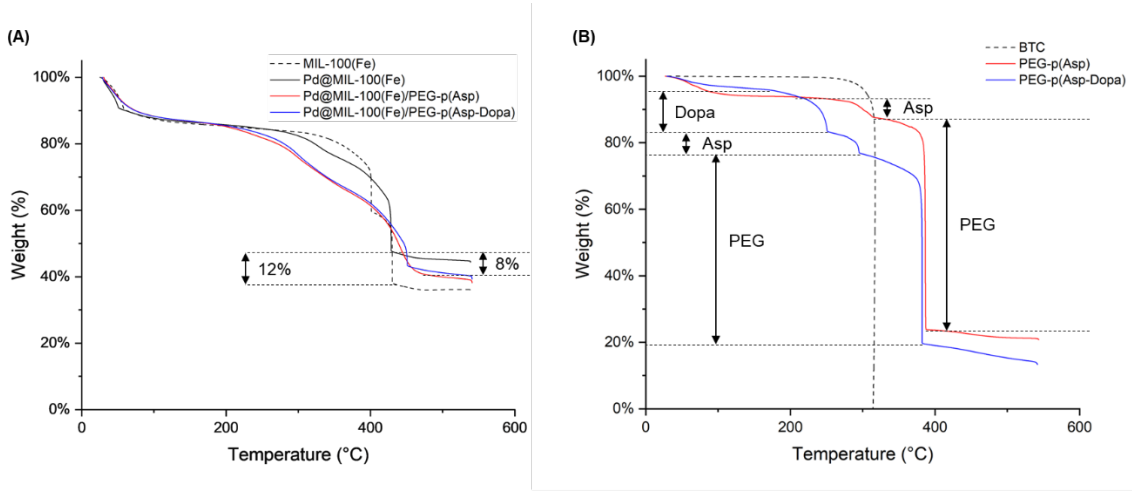

Figure 3.11 The TGA of (A) MIL-100(Fe), Pd@MIL-100(Fe), Pd@MIL-100(Fe)/PEG-p(Asp), and Pd@MIL-100(Fe)/PEG-p(Asp-Dopa), (B) BTC, PEG-p(Asp), and PEG-p(Asp-Dopa). The figure was adopted from S. W. Li *et al.* (2023) with the permission.

3.3.3 Photothermal capability of Pd@MIL-100(Fe)/polymer hybrids

Following the characterization of particle morphology and composition, our attention turned to elucidating the photothermal capability of Pd@MIL-100(Fe) and Pd@MIL-100(Fe)/polymer hybrids. To comprehensively explore and characterize the photothermal capability of both Pd@MIL-100(Fe) and Pd@MIL-100(Fe)/polymer hybrids, the photothermal conversion efficiency (η) was determined through the application of the time constant method. The results, as illustrated in **Figure 3.12**, depicted a consistent heating and cooling profile across all particles. The determined photothermal conversion efficiencies (η) for Pd@MIL-100(Fe), Pd@MIL-100(Fe)/PEG-p(Asp), and Pd@MIL-100(Fe)/PEG-p(Asp-Dopa) were 87.0%, 88.7%, and 88.8%, respectively **(Figure 3.12)**. These comparable values indicate that the incorporation of MOF/polymer hybrids does not undermine the intrinsic photothermal capabilities of Pd@MIL-100(Fe).

A significant observation emerges when contrasting our Pd@MIL-100(Fe)/PEG-p(Asp-Dopa) with a photothermal conversion efficiency of 88.8% to previously documented porous Pd-NPs with an efficiency of 93.4% (Xiao *et al.*, 2014). The congruence in performance underscores that the incorporation of Pd-NPs into MIL-100(Fe) and the consequent formation of MOF/polymer hybrids have negligible effects on the photothermal capacity of Pd-NPs. Moreover, the nanoparticles engineered in this study, encompassing Pd@MIL-100(Fe) and Pd@MIL-100(Fe)/polymer hybrids, exhibited a remarkable photothermal conversion efficiency surpassing 85%, outperforming other reported nanoparticles, such as their carbon-based counterparts (H. Liu *et al.*, 2020). This high photothermal efficiency, as revealed in **Figure 3.12**, solidifies the potential of Pd@MIL-100(Fe) and its hybrids as effective photothermal agents.

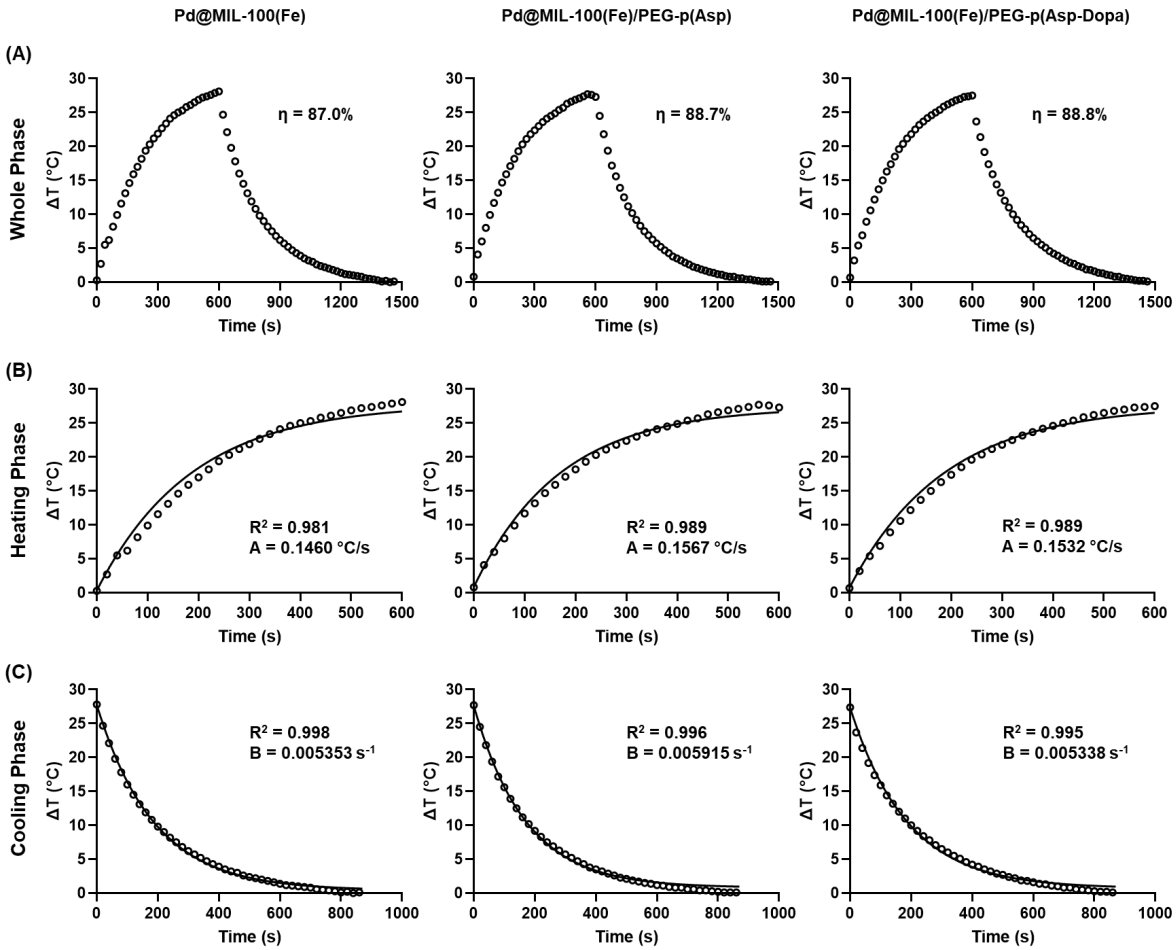

Figure 3.12 Determination of the photothermal conversion efficiency (η) for Pd@MIL-100(Fe), Pd@MIL-100(Fe)/PEG-p(Asp), and Pd@MIL-100(Fe)/PEG-p(Asp-Dopa). The photothermal effects, encompassing both the heating and cooling phases, were depicted. The NIR 808 nm laser, emitting at a power of 1.5 J/s, was administered for a duration of 600 seconds, after which the solution was allowed to cool naturally. Parameter A was derived by fitting non-linear regression to the heating stage curve, while parameter B was obtained from fitting the curve of the cooling stage. The figure was adopted from S. W. Li *et al.* (2023) with the permission.

Pd-NPs have been shown to be an excellent photothermal agent due to their high efficiency and stability in converting light into heat (P. Singh *et al.*, 2023). They can retain their photothermal effects after repeated heating and cooling cycles. Pd@MIL-100(Fe) and Pd@MIL-100(Fe)/polymer hybrids also exhibit high photothermal stability that is similar to Pd-NPs. They can consistently increase the temperature by more than 25°C even after five cycles of heating and cooling **(Figure 3.13)**. These results indicate that Pd@MIL-100(Fe) and Pd@MIL-100(Fe)/polymer hybrids are suitable candidates for photothermal applications, as they have comparable performance and stability to Pd-NPs.

To delve deeper into the photothermal capabilities of Pd@MIL-100(Fe) and Pd@MIL-100(Fe)/polymer hybrids, varying concentrations of these nanoparticles suspended in water were scrutinized, with MIL-100(Fe) lacking Pd serving as a control. All Pd-containing MIL-100(Fe) particles exhibited comparable photothermal responses under NIR 808 nm light exposure for 10 minutes at an energy density of 0.6 W/cm^2, aligning with the findings from the photothermal conversion efficiency assessment **(Figure 3.12 and Figure 3.14)**. Previous studies have shown that temperatures above 42°C, or 5°C higher than the normal body temperature (37°C), can induce hyperthermia and cause cell death (Horseman *et al.*, 2022; X. S. Li *et al.*, 2020). Our findings reveal that even at the lowest concentration of 0.1 mg/mL, all Pd-containing MIL-100(Fe) particles achieve a 5°C temperature increase within 3 minutes.

It has been reported that Pd-NPs are excellent photothermal agents with high efficiency, stability and biocompatibility (Rubio-Ruiz *et al.*, 2018; Xiao *et al.*, 2014). Consistent with these reports, our Pd@MIL-100(Fe)/polymer hybrids showed high photothermal potential, with the ability to heat up by more than 20°C making them not only suitable as photothermal agents but also showing the potential for therapeutic applications.

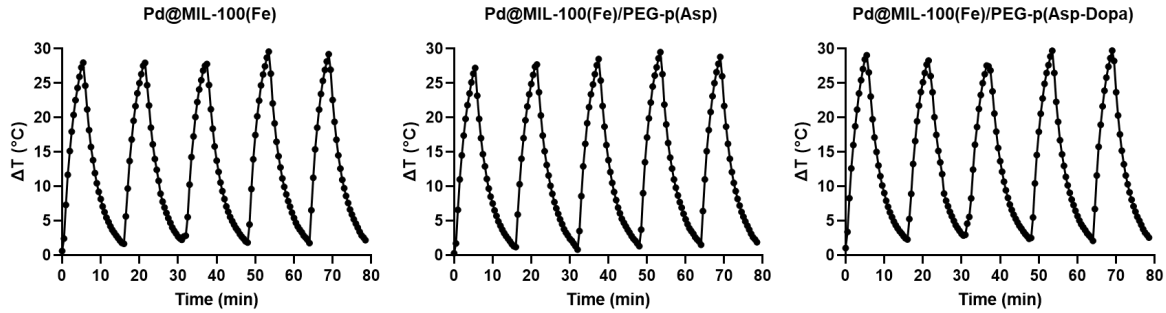

Figure 3.13 Photothermal stability of Pd@MIL-100(Fe), Pd@MIL-100(Fe)/PEG-p(Asp), and Pd@MIL-100(Fe)/PEG-p(Asp-Dopa). The particles were heated with NIR 808 nm light with the energy density of 0.6 W/cm^2 for 5 min and cooled naturally for 10 min. The heating and cooling cycle was conducted for 5 times.

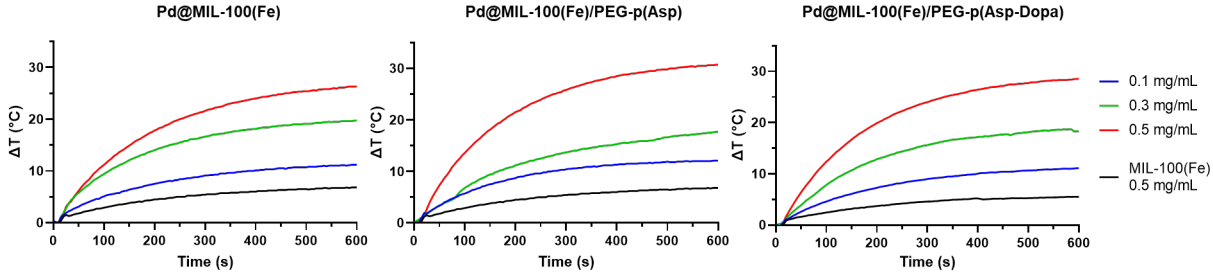

Figure 3.14 Photothermal capability of Pd@MIL-100(Fe), Pd@MIL-100(Fe)/PEG-p(Asp), and Pd@MIL-100(Fe)/PEG-p(Asp-Dopa) at various concentrations (0.1. 0.3, and 0.5 mg/mL). The particles were heated with NIR 808 nm light with the energy density of 0.6 W/cm^2. The control group shown in black line was 0.5 mg/mL MIL-100(Fe). The figure was adopted from S. W. Li *et al.* (2023) with the permission.

3.3.4 Stability of Pd@MIL-100/polymer hybrids

Prior studies have noted the propensity of MIL-100(Fe) particles to aggregate in aqueous solutions; however, in biological environments, they may adsorb proteins, leading to the formation of a protective protein corona (Kush *et al.*, 2020; Simon-Yarza *et al.*, 2016). To be useful as the therapeutic application, beside the photothermal capability, the aqueous stability, especially in physiological condition, of the nanoparticles is crucial. Therefore, the short-term (6 hours) and long-term (7 days) stability of MOF and MOF/polymer hybrids in physiological condition was tested. First the short-term stability was tested in water and phosphate-buffered saline (PBS) with 35 mg/mL bovine serum albumin (BSA), which mimics biological conditions. The hydrodynamic diameter and PDI were monitored for 6 h. Notably, Pd@MIL-100(Fe) particles exhibited a tendency to aggregate in both water and PBS with BSA, as evidenced by an increase in size and PDI **(Figure 3.15A)**. While Pd@MIL-100(Fe)/PEG-p(Asp) also displayed signs of aggregation, the extent was less pronounced compared to Pd@MIL-100(Fe) **(Figure 3.15A)**. In contrast, Pd@MIL-100(Fe)/PEG-p(Asp-Dopa) demonstrated robust stability, remaining dispersed in both water and PBS with BSA, as reflected by consistent size and low PDI **(Figure 3.15A)**. Notably, Pd@MIL-100(Fe)/PEG-p(Asp-Dopa) maintained stability even in media containing serum, further affirming its suitability for physiological applications **(Figure 3.15A)**.

To delve deeper into the analysis of physiological stability, we implemented a long-term stability assessment last for 7 days under PBS with 10% FBS at 37°C. Within a mere 2 days of incubation, Pd@MIL-100(Fe) exhibited swift aggregation, resulting in an average diameter exceeding 400 nm and a polydispersity index (PDI) surpassing 0.8 **(Figure 3.15B)**. In contrast, Pd@MIL-100(Fe)/PEG-p(Asp) exhibited improved stability compared to Pd@MIL-100(Fe), maintaining a relatively consistent average diameter around 170 nm **(Figure 3.15B)**. Nevertheless, its PDI gradually increased over time, surpassing 0.6 after 5 days. Remarkably,

Pd@MIL-100(Fe)/PEG-p(Asp-Dopa) maintained both its average diameter at approximately 155 nm and a PDI around 0.3, even after the full 7-day duration **(Figure 3.15B)**. The noticeable outcome underscored the substantial improvement in stability achieved by incorporating PEG-p(Asp-Dopa) onto Pd@MIL-100(Fe), demonstrating minimal fluctuations in size and PDI over the entire 7-day timeframe compared to Pd@MIL-100(Fe) and Pd@MIL-100(Fe)/PEG-p(Asp). These findings provide compelling evidence of the robust serum stability of Pd@MIL-100(Fe)/PEG-p(Asp-Dopa) within a PBS solution containing 10% FBS over the 7-day evaluation period.

The observation of Pd@MIL-100(Fe) without surface stabilization revealed a tendency for aggregation in the aqueous environment, which is highlighted in the stability analysis **(Figure 3.15)**. Accordingly, the TEM images presented in **Figure 3.9** visually emphasized this phenomenon. Additionally, in physiological conditions, various metal ions, including Fe, Zn, Cu, Ca, Na, etc., are presented. MIL-100(Fe) is composed of Fe and BTC organic linkers through coordination. The presence of other metal ions may replace the Fe in MIL-100(Fe) through ligand exchange, ultimately leading to its decomposition (Ding *et al.*, 2019). Previous research indicates that water molecules can also attack the coordination between Fe and BTC, resulting in the gradual destabilization (T. N.-M. Le *et al.*, 2021). Furthermore, in the physiological environment, proteins can adsorb onto the surface of MIL-100(Fe), leading to destabilization and clearance from blood circulation. In our research, engineered PEG block copolymers effectively and stably protect the surface of MIL-100(Fe) **(Figure 3.15)**. Steric stabilization through the long PEG chain shields the surface of MIL-100(Fe) from easy attack by other metal ions in the serum. Furthermore, the polymer coatings can modulate the formation of a protein corona, preventing capture by the liver or reticuloendothelial system (Cabral *et al.*, 2023). Therefore, the surface stabilization of Pd@MIL-100(Fe) by PEG-p(Asp-Dopa) effectively safeguards the surface, ensuring particle stabilization.

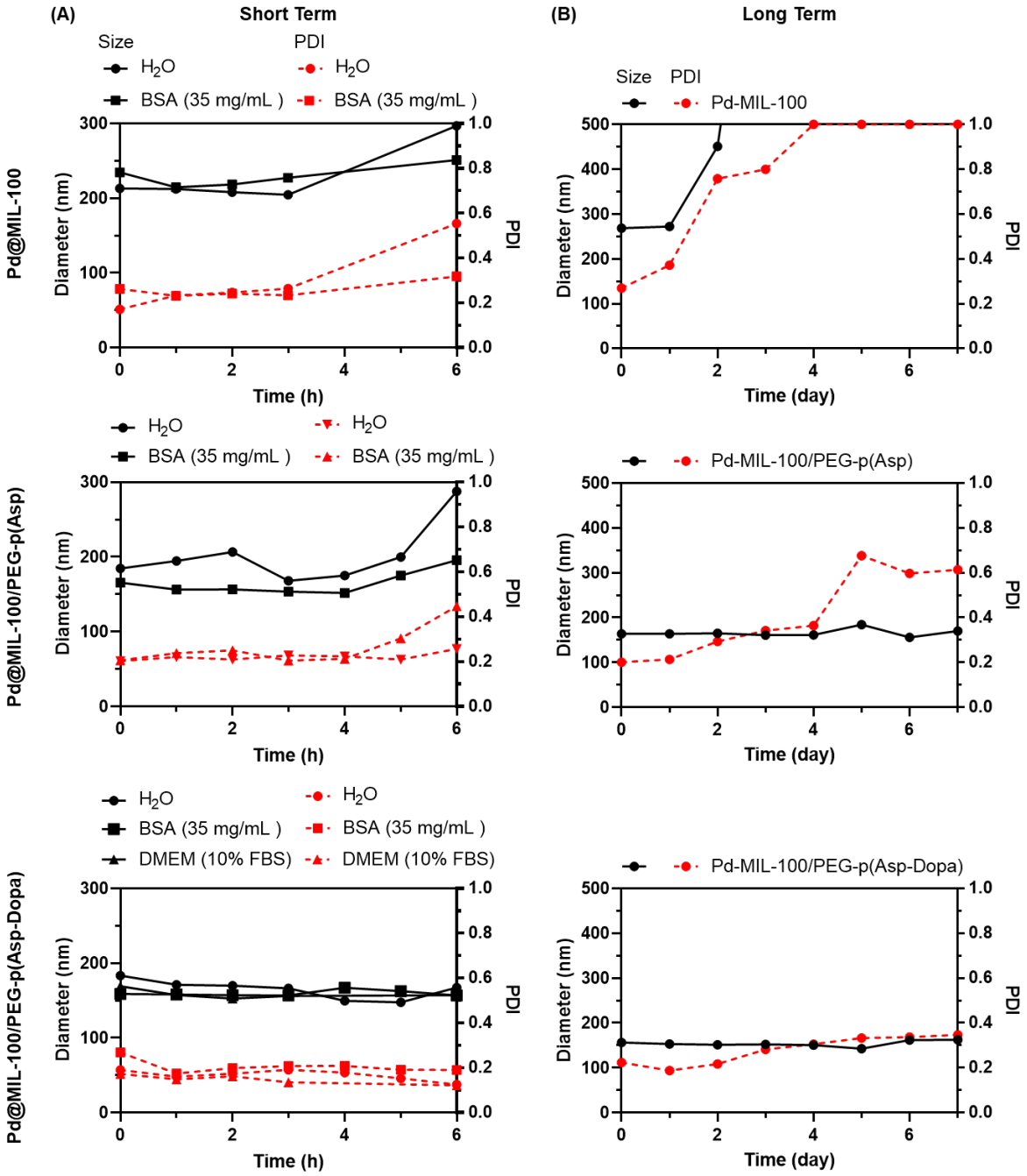

Figure 3.15 The aqueous stability of Pd@MIL-100(Fe), Pd@MIL-100(Fe)/PEG-p(Asp), and Pd@MIL-100(Fe)/PEG-p(Asp-Dopa) tested in (A) short term for 6 h in various aqueous conditions and (B) long term for 7 days in PBS with 10% FBS. The diameters were shown in black lines and PDI in red lines. The figure was adopted from S. W. Li *et al.* (2023) with the permission.

3.4 Summary

Two distinct surface protection strategies were explored for Pd@MIL-100(Fe): employing a PEG-p(Asp) block copolymer and its modification with dopamine to create a PEG-p(Asp-Dopa) derivative. PEG-p(Asp) was intricately designed with carboxylates on the aspartic acid side chain to form the complex with Fe ions, while PEG-p(Asp-Dopa) was engineered with a catechol group on the dopamine side chain to enhance the complexation with Fe ions. The rationale behind these polymers was to augment stability and shield the surface by the PEG block. Both polymers were integrated with Pd@MIL-100(Fe) to protect the surface, resulting in the Pd@MIL-100(Fe)/polymer hybrids. These hybrids exhibited reduced diameter and as confirmed by TEM images, displayed a superiorly dispersed morphology after the surface stabilization via the block copolymers. Moreover, their aqueous and serum stability was confirmed, demonstrating enhanced stability in both short-term and long-term tests. Particularly noteworthy was the remarkable serum stability of Pd@MIL-100(Fe)/PEG-p(Asp-Dopa), maintaining a consistent diameter of approximately 155 nm and a low PDI of about 0.3 over a 7-day period. The photothermal conversion efficiency (η) of Pd@MIL-100 and Pd@MIL-100(Fe)/polymer hybrids achieved 85%, closely matching that of Pd-NPs. Furthermore, these hybrids showcased robust photothermal stability and capability, even at low concentrations (0.1 mg/mL). Demonstrating a temperature increase of over 5°C in less than 3 min at the 0.1 mg/mL concentration, combined with their favorable serum stability, the Pd@MIL-100(Fe)/polymer hybrids emerged not only as potent photothermal agents but also as promising candidates for cancer therapeutics.

Chapter 4.

Biological evaluation of Pd@MIL-100/polymer hybrids

4.1 Introduction

Among the non-invasive targeted cancer therapies, PTT stands out for its potential to eradicate cancer while minimizing harm to surrounding healthy tissues. Transition metal nanoparticles exhibit a notably high photothermal conversion rate (Lv *et al.*, 2021), with palladium nanoparticles (Pd-NPs) demonstrating exceptional performance in converting NIR light into heat (Bian *et al.*, 2021; Peng *et al.*, 2022). Furthermore, the synthesis of Pd-NPs within MOF structures from palladium ions using alcohol as a reductive agent has been proposed, making Pd-NPs an ideal candidate to explore the capability of MIL-100(Fe) as a platform for generating and delivering photothermal nanoparticles (Y. Li *et al.*, 2022).

The skin cancers such as melanoma that usually appear near the surface of the skin are readily reachable by NIR light. In the context of melanoma, intrinsic and acquired resistance remains a major obstacle in curative treatment (La *et al.*, 2020). Furthermore, the management of patients with metastatic melanoma, refractory to initial therapy, remains challenging with poor overall prognosis and limited therapeutic options (Schwab *et al.*, 2016). Due to the unmet medical needs and the suitability for PTT, melanoma, particularly B16F10 melanoma cancer cell line, was chosen in this study for assessing the therapeutic efficacy of Pd@MIL-100(Fe)/polymer hybrids both *in vivo* and *in vitro*.

In this chapter, initially, the cellular uptake of Pd@MIL-100(Fe) and its polymer hybrids was commenced using ICP-MS followed by the biocompatibility assay and photothermal killing assay through the cellular viability tests. Moreover, the dynamics of blood circulation and biodistribution of these nanoparticles were investigated with ICP-MS. B16F10 melanoma-bearing mice were employed to assess the therapeutic efficacy of Pd@MIL-100(Fe)/PEG-p(Asp-Dopa). Following this, toxicity assessments were conducted by quantifying serum biomarkers.

4.2 Materials and methods

4.2.1 Materials

Phosphate buffered saline (PBS), trypsine/EDTA solution, CM-H_2DCFDA, and Hoechst® 33342 solution were obtained from ThermoFisher Scientific (Waltham, USA). High glucose Dulbecco's Modified Eagle's Medium (DMEM) was acquired from Sigma-Aldrich (St. Louis, MO, USA). Penicillin/streptomycin stock solution was purchased from Fujifilm Wako (Osaka, Japan). Cell counting kit-8 (CCK8) was purchased from Dojindo Laboratory (Kumamoto, Japan). CellBanker was acquired from Takara (Kyoto, Japan). Isofluorane was purchased from Pfizer (New York, NY, USA).

4.2.2 Cell lines and animal model

The melanoma cancer cell line, B16F10, was obtained from Cell Bank, Riken BioResource Center (Kyoto, Japan). The B16F10 cells were cultured under high glucose DMEM (4500 mg/L glucose, L-glutamine, sodium pyruvate, and sodium bicarbonate) supplemented with 10% FBS and 100 U/mL penicillin-streptomycin in 37°C incubator with 95% air, and 5% CO_2. The passage of the cells was performed with trypsine/EDTA solution (0.025% trypsin and 0.01% EDTA in PBS) every 3-4 days whenever the cells reached about 80% confluency. The frozen stock of the cell lines was prepared with CellBanker. The *in vivo* animal experiments were performed on 5-week-old female black mouse, C57BL/6j which were purchased from The Jackson Laboratory (Kanagawa, Japan). All animal experiments conducted during this research were authorized by The University of Tokyo adhering to the Guidelines for the Care and Use of Laboratory Animals (approval number: A2023E005-01).

4.2.3 Determination of cellular uptake with ICP-MS

Melanoma cancer cells, B16F10, were selected as the model for both *in vitro* and *in vivo* investigations of photothermal therapy (PTT). Cellular uptake of the hybrid materials was assessed through the quantification of Pd abundance using Inductively Coupled Plasma Mass Spectrometry (ICP-MS) with indium (In) serving as the internal standard. In 6-well plates, B16F10 cells were seeded at a density of 2×10^5 cells per well in DMEM with 10% FBS and allowed to grow overnight at 37°C. Following an 18-hour incubation, cells were washed three times with PBS, and the cell pellet was collected through trypsinization. Subsequently, Pd@MIL-100(Fe) and Pd@MIL-100(Fe)/polymer hybrids were added to the wells at concentrations of 0.1 and 0.5 mg/mL. The cell pellets were then digested with aqua regia at 200°C, and the extent of cellular uptake was determined by measuring Pd abundance via ICP-MS (Vojtek *et al.*, 2020).

4.2.4 In vitro cytotoxicity assessment

Cell viability was assessed using the CCK-8 assay to determine cytotoxicity. B16F10 melanoma cancer cells were seeded in a 96-well plate at a density of 9,000 cells per well. Various concentrations (ranging from 0.003 to 1 mg/mL) of Pd@MIL-100(Fe), Pd@MIL-100(Fe)/PEG-p(Asp), and Pd@MIL-100(Fe)/PEG-p(Asp-Dopa) were added, with PBS serving as the control. Following a 24-hour incubation at 37°C, CCK-8 solution was introduced into each well and incubated for an additional hour. Cellular viability was assessed by measuring the absorbance at 450 nm using a multi-well plate reader (Spark, Tecan, Männedorf, Switzerland).

The photothermal killing assay was conducted similarly. B16F10 cells were seeded in a 96-well plate at a density of 9,000 cells per well. Various concentrations (ranging from 0.003 to 1 mg/mL) of Pd@MIL-100(Fe), Pd@MIL-100(Fe)/PEG-p(Asp), and Pd@MIL-

100(Fe)/PEG-p(Asp-Dopa) were introduced to the wells. After 24 hours, an NIR 808 nm laser was applied to each well at an energy density of 0.6 W/cm^2 for 10 minutes, maintaining the initial cell temperature at around 30°C using a thermal plate. Subsequently, CCK-8 was added to each well and incubated for 1 hour. Cellular viability was determined by measuring the absorbance at 450 nm using a multi-well plate reader (Spark, Tecan, Männedorf, Switzerland).

4.2.5 Intracellular reactive species analysis

The B16F10 melanoma cancer cells were initially seeded onto a glass-bottom 8-well chamber slide at a density of 50,000 cells per well. After cell attachment, Pd@MIL-100(Fe) was introduced into the wells at a concentration of 0.5 mg/mL. To serve as controls, PBS was included as a negative control, while a 10 mM H_2O_2 solution was utilized as a positive control. Twenty-four hours post-incubation, the cells were washed with PBS twice. Before staining with CM-H_2DCFDA according to the manufacturer's guidelines, an NIR 808 nm laser was applied to each well at an energy density of 0.6 W/cm^2 for 10 minutes. The nucleus was stained with Hoechst® 33342. Images of the cellular components were captured using confocal laser scanning microscopy (LSM-780, Zeiss, Oberkochen, Germany). The images were taken using an excitation wavelength of 405 nm and an emission wavelength of 450 nm to visualize the cell nuclei. Additionally, an excitation wavelength of 488 nm and an emission wavelength of 520 nm were employed to visualize the CM-H_2DCFDA, indicating the intracellular reactive oxygen species (ROS).

4.2.6 Plasma clearance and tumor accumulation in mouse model

Hello, this is Bing. I can help you with rewriting and revising your text. Here is a possible version:

Using a 29G needle, we injected 50 μL of B16F10 melanoma cells (1×10^6 cells/mouse) subcutaneously into C57BL/6j black mice. After about a week, the tumor volume reached over 50 mm^3. We then injected Pd@MIL-100(Fe), Pd@MIL-100(Fe)/PEG-p(Asp), or Pd@MIL-100(Fe)/PEG-p(Asp-Dopa) intravenously through the tail vein at a Pd dose of 2.5 mg/kg. We anesthetized the mice with isoflurane 24 h later and collected blood samples from the orbital sinus at 0, 1, 2, 3, 6, 12, and 24 h. We euthanized the mice after 24 h and harvested and weighed the tumor, kidney, liver, and spleen tissues. We digested all the tissues with aqua regia at 200°C and dissolved them in 1% aqua regia. We measured the Pd concentration in each sample by ICP-MS (7900, Agilent, California, USA) using In as the internal standard (Vojtek *et al.*, 2020). The half-life of Pd@MIL-100(Fe)/PEG-p(Asp-Dopa) was estimated with the 2-phase exponential decay. The first phase (fast-decaying phase, S_{Fast}) was represented as **Equation 4.1**:

$$S_{Fast} = (Y_0 - P) \times F \times 0.01 \quad (4.1)$$

where Y_0 is the Y value when time is zero, P is the Y value at infinite times, and F is the fraction of the span (from Y_0 to P). The second phase (slow-decaying phase, S_{Slow}) was depicted as **Equation 4.2** and the 2-phase decaying curve was shown as **Equation 4.3**:

$$S_{Slow} = (Y_0 - P) \times (100 - F) \times 0.01 \quad (4.2)$$

$$Y = P + S_{Fast} \times e^{-\alpha t} + S_{Slow} \times e^{-\beta t} \quad (4.3)$$

where t is time, α is rate constant for the fast-decaying phase while β is rate constant for the slow decaying phase. The half-life of two phases was obtained by curve fitting to **Equation 4.3**.

4.2.7 In vivo antitumor efficacy

We used C57BL/6j black mice and B16F10 melanoma cells to evaluate the antitumor effect of Pd@MIL-100(Fe)/PEG-p(Asp-Dopa) *in vivo*. **Figure 4.1** shows the design of the animal experiments. We injected 50 μL of 1 × 10^6 cells/mouse subcutaneously with a 29G needle. After about a week, the tumor volume grew over 50 mm^3. We then randomly assigned the mice to four groups of five mice each. Two groups received intravenous injections of PBS or Pd@MIL-100(Fe)/PEG-p(Asp-Dopa) at a Pd concentration of 25 mg/kg, without NIR 808 nm laser irradiation. The other two groups received the same injections and were irradiated with NIR 808 nm laser at 1 W/cm^2 for 30 min, 24 h after injection. We measured the tumor temperature every 5 seconds with a digital thermometer (TM-947SD, Lutron, Taipei, Taiwan) and a small Pt-100 thermo-resistor. We also took thermal images at 0, 1, and 5 min during irradiation with a thermal camera (FLIR ONE Gen 3, Teledyne FLIR, Oregon, USA). We recorded the tumor volume, body weight, and survival of the mice every 2 days for 25 days. Tumor volume was calculated using **Equation 4.4**:

$$V = \frac{1}{2} L \times W^2 \tag{4.4}$$

where V is the size, L is the length, and W is the width of the tumor.

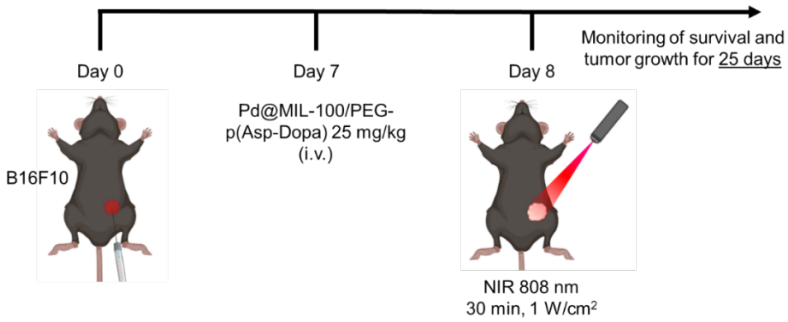

Figure 4.1 The design and timeline of animal experiments.

4.2.8 Analysis of serum biomarkers

We evaluated the biocompatibility of Pd@MIL-100(Fe)/PEG-p(Asp-Dopa) *in vivo* using C57BL/6j black mice. We randomly assigned the mice to two groups of three mice each and injected them intravenously with PBS or Pd@MIL-100(Fe)/PEG-p(Asp-Dopa) at a Pd dose of 25 mg/kg through the tail vein. We anesthetized the mice with isoflurane and collected 200 μL of blood from the orbital sinus 24 h later. We incubated the blood samples at room temperature for 10 min and centrifuged them at 1,500 x g for 10 min at 4°C to obtain the serum from the supernatant. We then measured the serum levels of alanine aminotransferase (ALT), aspartate aminotransferase (AST), creatinine (CRE), blood urea nitrogen (BUN), and total protein (TP) using 10 μL of serum and Fuji DRI-CHEM slides (Fujifilm, Tokyo, Japan) with DRI-CHEM NX700 (Fujifilm, Tokyo, Japan).

4.2.9 Statistics analysis

The results are presented as mean ± standard deviation (SD). Statistical analyses and non-linear regressions were performed using GraphPad Prism 9 (Dotmatics, Massachusetts, USA). To determine statistical significance, we used the one-way analysis of variance (ANOVA) with Tukey's post-hoc test, unless otherwise specified. Kaplan-Meier survival analysis was utilized to assess the survival curve in the anti-tumor experiments. A p-value below 0.05 was deemed statistically significant.

4.3 Results and discussions

4.3.1 Cellular uptake of Pd@MIL-100/polymer hybrids in melanoma

The choice of a suitable cancer model is crucial for assessing the photothermal therapeutic efficacy of our Pd@MIL-100(Fe)/polymer hybrid system. Skin cancers, particularly those located on the skin's surface, were identified as an ideal target, as they are readily accessible to NIR light, making photothermal therapy effective (Huang *et al.*, 2021). Melanoma, a highly aggressive skin cancer, was specifically selected for our study due to its surface location and clinical significance. The B16F10 melanoma cancer cell line derived from C57BL/6j mice served as the *in vitro* and *in vivo* model for evaluating the therapeutic potential of Pd@MIL-100(Fe)/polymer hybrids.

Prior to initiating any *in vitro* and *in vivo* experiments, it is imperative to examine whether the nanoparticles can effectively enter the cells. Therefore, the cellular uptake of Pd@MIL-100(Fe) and Pd@MIL-100(Fe)/polymer hybrids was investigated in B16F10 cells to evaluate their intracellular delivery capability. The findings indicated that all MOFs particles exhibited uptake to a certain extent, suggesting their potential applicability in photothermal therapy **(Figure 4.2)**. Notably, the introduction of surface protection via PEG-p(Asp-Dopa) led to a significant two-fold increase in cellular uptake **(Figure 4.2)**. The cellular uptake of nanoparticles is commonly facilitated through various mechanisms, including endocytosis, macro-pinocytosis, phagocytosis, etc. The preferred route depends largely on the particle size, with endocytosis typically accommodating particles up to about 150-200 nm, while larger particles (more than 200 nm) often enter cells through macro-pinocytosis and phagocytosis, processes commonly observed in macrophages (Figueiredo Borgognoni *et al.*, 2018).

In our chosen melanoma model cell line, B16F10, macro-pinocytosis and phagocytosis capabilities are limited. Therefore, when particle aggregation results in sizes exceeding 200 nm, cellular uptake may be impeded. As illustrated in the stability results **(Figure 3.15)**, both

Pd@MIL-100(Fe) and Pd@MIL-100(Fe)/PEG-p(Asp) experienced rapid destabilization and aggregation beyond 200 nm within 4 hours. In contrast, due to the steric stabilization imparted by PEG, Pd@MIL-100(Fe)/PEG-p(Asp-Dopa) remained stable at sizes between 150-160 nm over 6 hours. Hence, the increased internalization of PEG-p(Asp-Dopa)-modified Pd@MIL-100(Fe)/polymer hybrids by B16F10 cells can be ascribed to their enhanced stability and diminished particle size. This underscores the significance of surface protection in optimizing cellular uptake for potential applications in photothermal therapy.

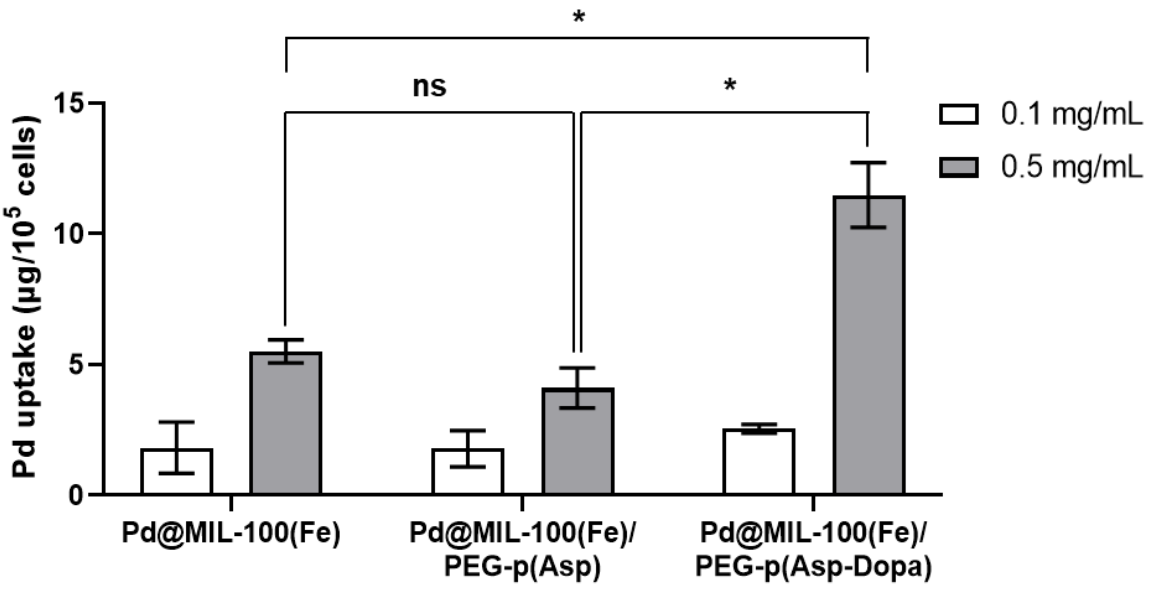

Figure 4.2 Determination of cellular uptake in B16F10 for Pd@MIL-100(Fe) and Pd@MIL-100(Fe)/polymer hybrids as Pd level with ICP-MS. The figure was adopted from S. W. Li *et al.* (2023) with the permission. (Data are presented as mean ± SD; n = 3; ns indicated not significant; * indicated $p < 0.05$)

4.3.2 Cytotoxicity of Pd@MIL-100/polymer hybrids in melanoma

In the previous section, we established that both Pd@MIL-100(Fe) and Pd@MIL-100(Fe)/polymer hybrids can efficiently accumulate within cells, presenting potential for photothermal therapy (PTT). However, this raises concerns regarding cytotoxicity and biocompatibility. To address these concerns, we conducted an assessment of cytotoxicity and the photothermal killing effect in vitro through a cell viability study. Initially, the materials were examined without NIR 808 nm irradiation. The results indicated that Pd@MIL-100(Fe) and Pd@MIL-100(Fe)/hybrids exhibited no significant toxic effects, maintaining cell viability over 80%, even at the highest concentration (1 mg/mL) without irradiation. This underscores their excellent biocompatibility **(Figure 4.3A)**, consistent with prior reports highlighting the biocompatibility of MIL-100(Fe) and Pd materials (Czarnomysy *et al.*, 2021; P. Horcajada *et al.*, 2010).

To assess the photothermal killing effects, NIR 808 nm irradiation was administered at an energy density of 0.6 W/cm2 for 10 minutes. The temperature of Pd@MIL-100(Fe) and Pd@MIL-100(Fe)/polymer hybrids increased in a dose-dependent manner for all tested systems, encompassing naked Pd@MIL-100(Fe), Pd@MIL-100(Fe)/PEG-p(Asp), and Pd@MIL-100(Fe)/PEG-p(Asp-Dopa) **(Figure 4.3B)**. The achieved temperatures correspond to different hyperthermia categories: 40-41°C (long-term low-temperature hyperthermia) at 0.03 mg/mL, 45-50°C (moderate-temperature hyperthermia) at 0.1 mg/mL, and temperatures exceeding 50°C (thermal ablation) starting at 0.5 mg/mL **(Figure 4.3B)** (Overchuk *et al.*, 2023).

As a result, cell viability experienced a significant decrease from 0.1 mg/mL (representing moderate-temperature hyperthermia), reaching complete cell death in cancer cells at 0.5 mg/mL (indicating thermal ablation) for all particles **(Figure 4.3A)**. Both Pd@MIL-100(Fe) and Pd@MIL-100(Fe)/polymer hybrids exhibited notable resilience in cells, accompanied by substantial photothermal killing effects **(Figure 4.3A)**. These findings align

with reported photothermal therapy (PTT) efficacy for Pd-NPs, underscoring their potential for substantial cancer cell ablation (Phan *et al.*, 2020; Xiao *et al.*, 2014).

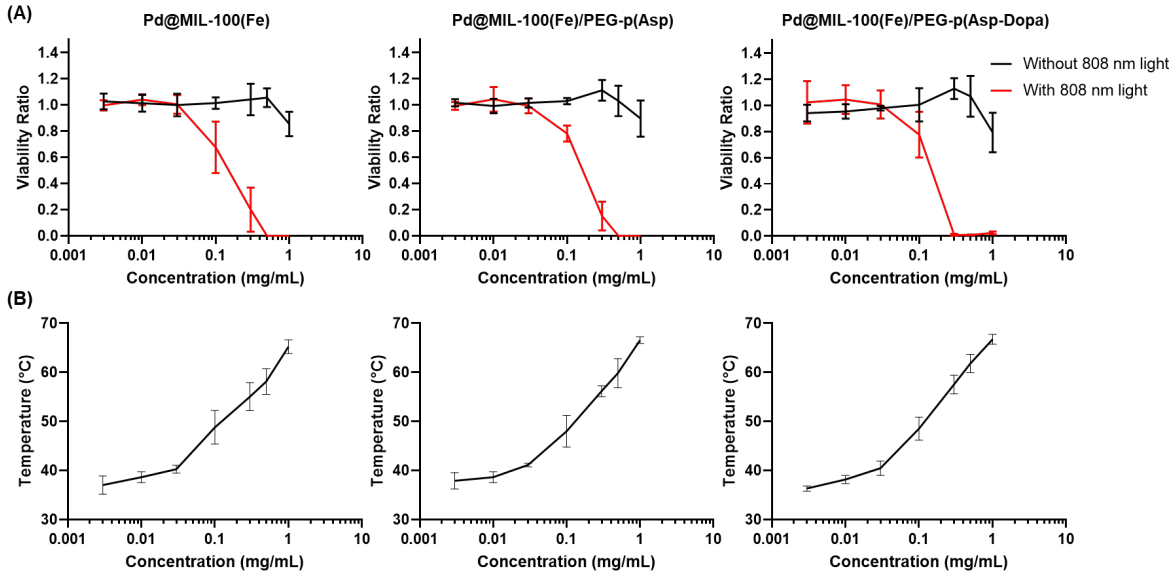

Figure 4.3 Cellular viability of B16F10 after treatment of Pd@MIL-100(Fe) and Pd@MIL-100(Fe)/polymer hybrids at various concentrations. (A)The viability of cells treated solely with MOFs, without exposure to NIR 808 nm light irradiation, is depicted in the black line. Meanwhile, the red line represents the viability of cells treated with MOFs and subjected to NIR 808 nm light irradiation. (B) The temperature changes during NIR irradiation of Pd@MIL-100(Fe) and Pd@MIL-100(Fe)/polymer hybrids at various concentrations. The figure was adopted from S. W. Li *et al.* (2023) with the permission. (Data are presented as mean ± SD; n = 6)

The use of NIR 808 nm light to activate Pd-NPs is recognized for inducing photothermal effects, but the contribution of photodynamic effects is equally significant (Y. Liu *et al.*, 2020). During the irradiation of Pd-NPs, the production of reactive oxygen species (ROS) accompanies the heat generation, forming a dual-action mechanism (W. Zhang *et al.*, 2023). This combined effect of heat and ROS can effectively impede the proliferation of cancer cells. In our investigation, Pd@MIL-100(Fe) exhibited robust photothermal effects capable of restraining cancer cell growth **(Figure 4.3)**. Additionally, the generation of intracellular ROS of Pd@MIL-100(Fe) after NIR 808 nm light irradiation was confirmed in the preliminary data **(Figure 4.4)**. According to the previous research, the anticancer properties observed in both Pd@MIL-100(Fe) and Pd@MIL-100(Fe)/polymer hybrids potentially originate from a blend of photothermal and photodynamic effects (Overchuk *et al.*, 2023). These effects tend to act synergistically and are challenging to segregate due to their simultaneous occurrence. Our findings affirm that the photothermal effect of Pd-NPs remains intact following their encapsulation within MIL-100(Fe) and subsequent surface coating with polymers. These promising *in vitro* outcomes serve as a strong foundation, warranting further exploration of Pd@MIL-100(Fe)/polymer hybrids for potential PTT in mouse models.

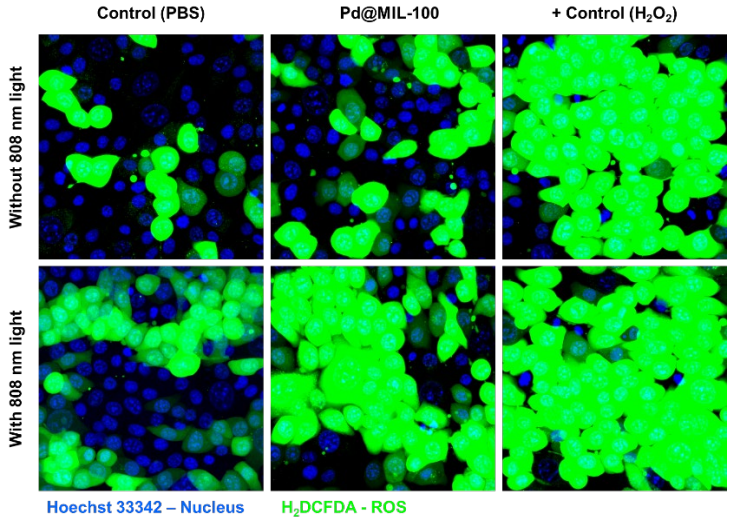

Figure 4.4 The intracellular ROS in B16F10 cell stained with H_2DCFDA. H_2O_2 (10 mM) was used as positive control. Pd@MIL-100(Fe) was treated at 0.5 mg/mL.

4.3.3 Biodistribution of Pd@MIL-100/polymer hybrids

Before evaluating the anti-tumor potential of Pd@MIL-100(Fe)/polymer hybrids in a mouse model, it was crucial to investigate the pharmacokinetics of both Pd@MIL-100(Fe) and Pd@MIL-100(Fe)/polymer hybrids. Initially, we examined the plasma clearance of Pd@MIL-100(Fe)/polymer hybrids following intravenous injection. In this study, B16F10 tumor-bearing mice were administered an intravenous injection of Pd@MIL-100(Fe)/polymer hybrids at a concentration of 2.5 mg/kg based on Pd content. The experiment involved quantifying Pd levels in the plasma using ICP-MS at 1, 2, 3, 6, 12, and 24 hours post-injection. Remarkably, the Pd levels in the blood for Pd@MIL-100(Fe) dropped to below 3% of the injected dose (ID) per milliliter of plasma just 1 hour after injection **(Figure 4.5A)**. While the incorporation of PEG-p(Asp) on Pd@MIL-100(Fe) slightly enhanced the Pd levels in plasma, suggesting partial protection, it was insufficient for prolonging blood circulation **(Figure 4.5A)**. In contrast, the incorporation of Dopa moieties in Pd@MIL-100(Fe)/PEG-p(Asp-Dopa) substantially prolonged circulation compared to both Pd@MIL-100(Fe) and Pd@MIL-100(Fe)/PEG-p(Asp) **(Figure 4.5A)**. The half-life of Pd@MIL-100(Fe)/PEG-p(Asp-Dopa) in the bloodstream was determined by fitting the pharmacokinetic data to an exponential decay curve. In this study, we utilized a two-phase exponential decay function for curve fitting. This model assumes two distinct phases during the drug circulation following administration (Zuna & Holt, 2017). The initial phase, referred to as the α phase, represents the distribution of drugs into tissues, while the subsequent β phase indicates the removal of drugs after reaching equilibrium (Cabral *et al.*, 2023). As a result, there are 2 half-lives, the first half-life (fast-decaying phase) corresponds to the first drop in the plasma concentration and was estimated to be approximately 48 minutes. Moreover, the second half-life (slow-decaying phase) is around 12.5 h. The goodness of fit, as indicated by the coefficient of determination (R squared), is approximately 0.88. The longer circulation could be attributed to the surface stabilization by PEG-p(Asp-Dopa) on Pd@MIL-

100(Fe).

Upon the injection of MOF/polymer hybrids, particles accumulated in tissues such as the liver, spleen, tumor, and kidneys, while also being scavenged by the reticuloendothelial system, leading to the initial decline in blood levels of the hybrids. Upon reaching equilibrium, characterized by factors like tissue saturation or the formation of a protein corona reducing the uptake rate, the uptake of MOF/polymer hybrids decreased. Consequently, the hybrids were gradually taken up by tissues and eliminated from the body, representing the second, more prolonged phase of decay compared to the initial phase (Cabral *et al.*, 2023). Our blood circulation results, as depicted in this study, highlight that the MOF/polymer hybrids undergo rapid distribution to tissues within a short timeframe, exhibiting a first half-life of 48 minutes. After reaching equilibrium, the MOF/polymer hybrids circulate in the blood at lower concentrations for an extended period, indicating a second half-life of 12.5 hours **(Figure 4.5)**.

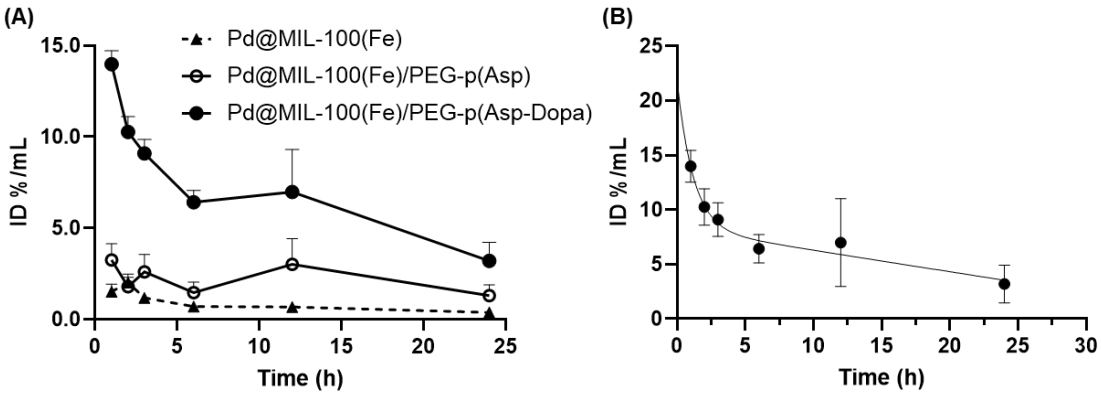

Figure 4.5 The blood circulation dynamics of Pd@MIL-100(Fe) and Pd@MIL-100/polymer hybrids. (A) The dynamics of MOFs were monitored as Pd level by ICP-MS for 24 h. (B) The two-phase exponential decay curve fitting to the Pd@MIL-100(Fe)/PEG-p(Asp-Dopa). The figure was adopted from S. W. Li *et al.* (2023) with the permission. (Data are presented as mean ± SD; n = 3)

The improved circulation within the bloodstream could potentially enhance the accumulation of nanoparticles in tumors through the enhanced permeability and retention effect (Wu, 2021). To assess this accumulation, tumors were gathered 24 hours post-injection, and the Pd levels were determined using ICP-MS. The Pd accumulation in tumors for Pd@MIL-100(Fe) was found to be below 0.05% of the injected dose (ID) per gram of tissue which is consistent to the previous study showing low tumor accumulation of MIL-100(Fe) **(Figure 4.6)** (Simon-Yarza *et al.*, 2016). A slightly elevated Pd accumulation was noted in Pd@MIL-100(Fe)/PEG-p(Asp) compared to Pd@MIL-100(Fe) **(Figure 4.6)**. Conversely, intravenous administration of Pd@MIL-100(Fe)/PEG-p(Asp-Dopa) exhibited significantly increased Pd accumulation at approximately 1.6% ID per gram of tissue, potentially facilitated by enhanced permeability and retention effects **(Figure 4.6)** (Fang *et al.*, 2020). It is essential to highlight that nanoparticle systems with surface reactivity, such as carbon-coated FeCo nanoparticles, often necessitate surface stabilization via polymeric coatings to enhance biodistribution (Song *et al.*, 2020). Similarly, PEG-p(Asp-Dopa) was introduced to stabilize the surface of Pd@MIL-100(Fe) aimed to improve the biodistribution. The Pd@MIL-100(Fe)/PEG-p(Asp-Dopa) exhibited improved tumor delivery further showcased the enhanced stabilization within the MOF/polymer hybrid system.

Furthermore, alongside tumor accumulation, the distribution of Pd@MIL-100(Fe) and Pd@MIL-100(Fe)/polymer hybrids across vital organs was investigated. After a 24-hour interval post-injection, the kidney, liver, and spleen were collected, and their Pd levels were assessed using ICP-MS. Prior research has indicated the inclination of MIL-100(Fe) towards liver accumulation (Simon-Yarza *et al.*, 2016). In **Figure 4.7**, we noted considerable accumulation of Pd@MIL-100(Fe) in the liver, approximating to roughly 45% ID per gram of tissue. Nevertheless, following the coating of PEG-p(Asp) and PEG-p(Asp-Dopa) on Pd@MIL-100(Fe), there was a significant reduction in liver accumulation, decreasing to

approximately 40% and 25% ID per gram of tissue, respectively **(Figure 4.7)**. Interestingly, in liver Pd@MIL-100(Fe)/PEG-p(Asp-Dopa) displayed the lowest accumulation. Conversely, all particles exhibited comparable spleen accumulation, ranging from 40% to 50% ID per gram of tissue **(Figure 4.7)**. This phenomenon might be owing to the natural tendency of the spleen to trap nanoparticles exceeding 150 nm in size, as previously identified in studies (Cabral *et al.*, 2018; Moghimi *et al.*, 2012). Research has highlighted the liver and spleen as primary sites for capturing and decomposing MIL-100(Fe) particles (Simon-Yarza *et al.*, 2016). Pd@MIL-100(Fe)/polymer hybrids also displayed accumulation in these organs. However, the hybrids coated with PEG-p(Asp-Dopa) exhibited a noteworthy reduction in liver accumulation **(Figure 4.7)**, potentially linked to their superior stability observed *in vitro*. The significant different accumulation behaviors between liver and spleen may attribute to the biological differences in liver and spleen.

Nanoparticles larger than 150 nm commonly face non-selective accumulation in the spleen due to mechanical entrapment in the splenic interendothelial slits (Cabral *et al.*, 2018). Conversely, liver accumulation is typically facilitated by the reticuloendothelial system and the scavenging receptor-assisted pathway (Cabral *et al.*, 2023). In this study, the particle size of Pd@MIL-100(Fe) is approximately 200 nm. The surface stabilization of Pd@MIL-100(Fe) by PEG-p(Asp) and PEG-p(Asp-Dopa) reduced the size to around 170 nm and 150 nm, respectively. While the coating of PEG-p(Asp-Dopa) decreased the particle size, the fate of entrapment in the spleen remains unavoidable, similar to Pd@MIL-100(Fe) and Pd@MIL-100(Fe)/PEG-p(Asp), owing to the 150 nm size. However, the robust surface protection of Pd@MIL-100(Fe) by PEG-p(Asp-Dopa) introduces an additional layer of steric protection through the PEG chain, effectively preventing binding to scavenging receptors (Cabral *et al.*, 2023). Due to reduced binding to scavenging receptors, the liver accumulation of Pd@MIL-100(Fe)/PEG-p(Asp-Dopa) decreased compared to both naked Pd@MIL-100(Fe) and less

stable Pd@MIL-100(Fe)/PEG-p(Asp). The extended circulation in the bloodstream, as depicted in **Figure 4.5**, coupled with the diminished liver accumulation illustrated in **Figure 4.7**, underscores the substantial role of surface stabilization provided by PEG-p(Asp-Dopa) in leading to higher accumulation of Pd@MIL-100(Fe) in tumor **(Figure 4.6)**.

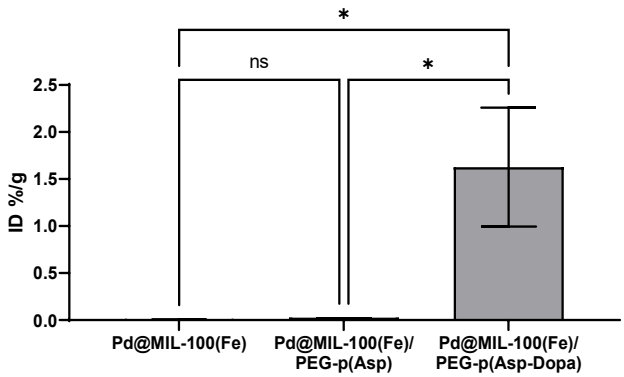

Figure 4.6 The tumor accumulation of Pd@MIL-100(Fe) and Pd@MIL-100(Fe)/polymer hybrids in B16F10 melanoma. The accumulation of MOFs was determined by ICP-MS as Pd level. The figure was adopted from S. W. Li *et al.* (2023) with the permission. (Data are presented as mean ± SD; ns indicated not significant; * indicated $p < 0.05$; n = 3 mice per group)

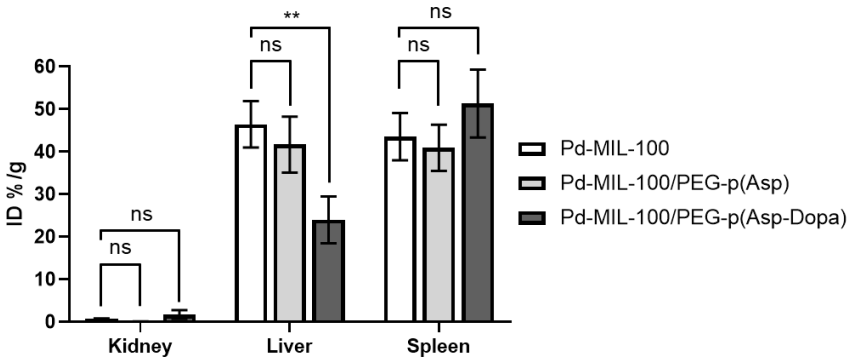

Figure 4.7 The biodistribution of Pd@MIL-100(Fe) and Pd@MIL-100(Fe)/polymer hybrids in B16F10 melanoma. The accumulation of MOFs was determined by ICP-MS as Pd level. The figure was adopted from S. W. Li *et al.* (2023) with the permission. (Data are presented as mean ± SD; ns indicated not significant; ** indicated $p < 0.01$; n = 3 mice per group)

4.3.4 Antitumor capability against melanoma

Due to its superior stability and remarkable tumor accumulation, Pd@MIL-100(Fe)/PEG-p(Asp-Dopa) was selected for further investigation of its potential photothermal therapeutic capabilities in tumor-bearing mice. To assess the capability of photothermal therapy, we intravenously injected Pd@MIL-100(Fe)/PEG-p(Asp-Dopa) at a dose of 25 mg/kg (based on Pd content) through tail vein to B16F10 melanoma bearing C57BL/6 mice while PBS was served as the negative control. After 24 hours of the injections, we irradiated the tumors with NIR 808 nm light at an energy density of 1 W/cm^2 for 30 minutes. The mice that were treated with PBS only, tumors rapidly grew from 50 mm^3 to over 2000 mm^3 within 15 days **(Figure 4.8)**. Similarly, in the mice received Pd@MIL-100(Fe)/PEG-p(Asp-Dopa) without NIR light irradiation, the tumor grew aggressively. Furthermore, extended NIR irradiation in the mice treated with PBS resulted in similarly fast tumor growth to PBS-treated mice **(Figure 4.8)**. Conversely, NIR-irradiated and Pd@MIL-100(Fe)/PEG-p(Asp-Dopa) treated mice demonstrated substantial tumor ablation, suppressing tumor growth without observable adverse effects **(Figure 4.8 and Figure 4.9)**. Fifteen days after irradiation, 2 out of 5 mice that treated with the MOF/polymer hybrid and NIR 808 nm irradiation exhibited complete responses. Additionally, the Pd@MIL-100(Fe)/PEG-p(Asp-Dopa)-treated and NIR-irradiated mice exhibited the prolonged surviving time compared to PBS only, PBS with NIR as well as Pd@MIL-100(Fe)/PEG-p(Asp-Dopa) without NIR **(Figure 4.10)**. Moreover, all the treatments did not affect the body weight indicating no observable systemic adverse effect and the safety of the interventions **(Figure 4.9)**.

Coating MOFs with polymers has emerged as a promising avenue to enhance drug delivery efficiency (X. Zhang *et al.*, 2021). In our study, we successfully addressed concerns related to the stability of MOFs with the formation of MOF/polymer hybrids in physiological environments, leading to effective delivery to tumors and triggering potent photothermal

effects *in vivo*. Our findings underscore that the surface stabilization of PEG-p(Asp-Dopa) on Pd@MIL-100(Fe) played important role in enhanced blood circulation and tumor accumulation and thus achieving therapeutic levels of Pd for photothermal therapy. However, comparing to previous polymeric drug delivery systems including micelles loading cisplatin and DACHPt, which exhibit several hours of half-life, the Pd@MIL-100(Fe)/polymer hybrids we developed still have room for improvement in terms of both blood circulation and tumor accumulation (Cabral & Kataoka, 2014; Cabral *et al.*, 2005). Hence, although our data demonstrate tumor ablation by delivering of sufficient Pd, more advancements in enhancing tumor targeting may potentially allow for the use of lower doses or shorter irradiation periods.

One plausible approach for improving stability and blood circulation involves optimizing the lengths of block polymer segments to achieve more effective PEG shielding and stronger binding with the MOF surface. Additionally, exploring a higher incorporation rate of Dopa might enhance the stability of MOF/polymer hybrids in the bloodstream. There is also potential in exploring the incorporation of tumor-targeting ligands onto the MOFs (Bajracharya *et al.*, 2022). However, the ligand presentation and the optimized density for eliciting the desired targeting effect should be considered (Mi *et al.*, 2020). For instance, a past study utilizing MIL-100(Fe) loading gold-nanorod with MCP-1 conjugation for targeting exhibited no enhancement in therapeutic effectiveness, indicating that modification with ligands alone might not be enough (Chien *et al.*, 2021). Combining block copolymers with ligands could potentially offer both stabilization and tumor-targeting capabilities, likely resulting in improved tumor accumulation and therapeutic effects (Elmehrath *et al.*, 2023). To fully investigate the potential of ligand-conjugated PEG-p(Asp-Dopa) stabilized MOF/polymer hybrids for cancer theranostics, more investigation is needed.

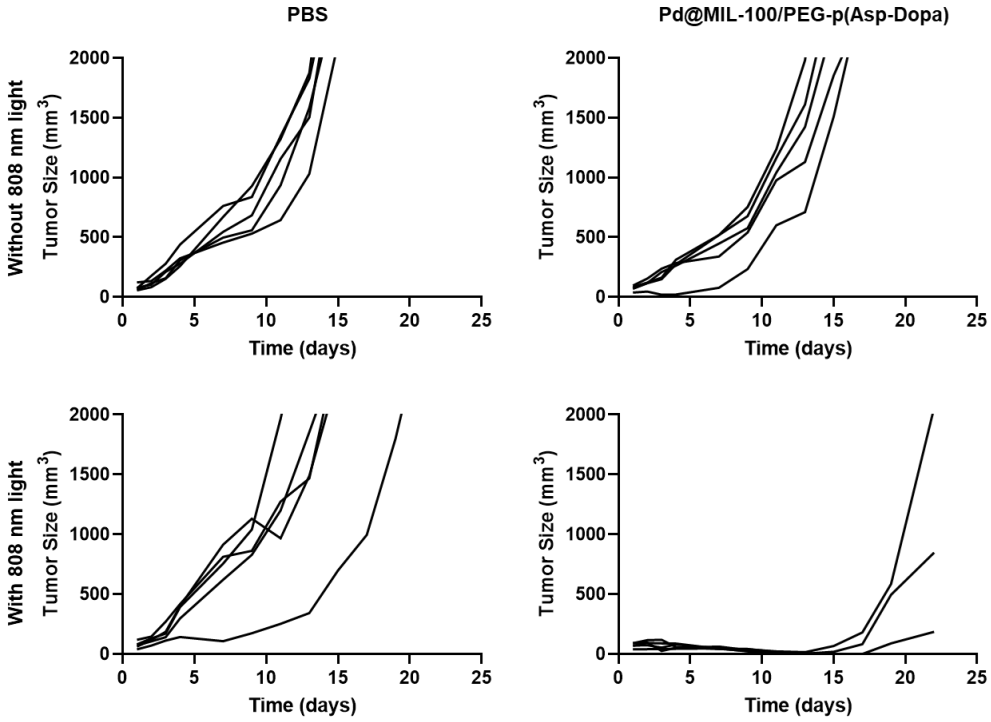

Figure 4.8 Antitumor efficacy assessment in B16F10 melanoma bearing mice. The size of tumors for each treatment (PBS and Pd@MIL-100(Fe)/PEG-p(Asp-Dopa) with or without NIR light irradiation) and mouse was plotted individually (n = 5 for each group). Intravenous injection of 25 mg/kg Pd@MIL-100(Fe)/PEG-p(Asp-Dopa) was applied once (day 5 post inoculation, concentration based on Pd) was administered to B16F10 melanoma bearing mice. The irradiation of NIR 808 nm light (1 W/cm^2, 30 min) was applied 1 day after injection. PBS was used as the control. The tumor size was monitored every 2 days for 25 days. The figure was adopted from S. W. Li *et al.* (2023) with the permission.

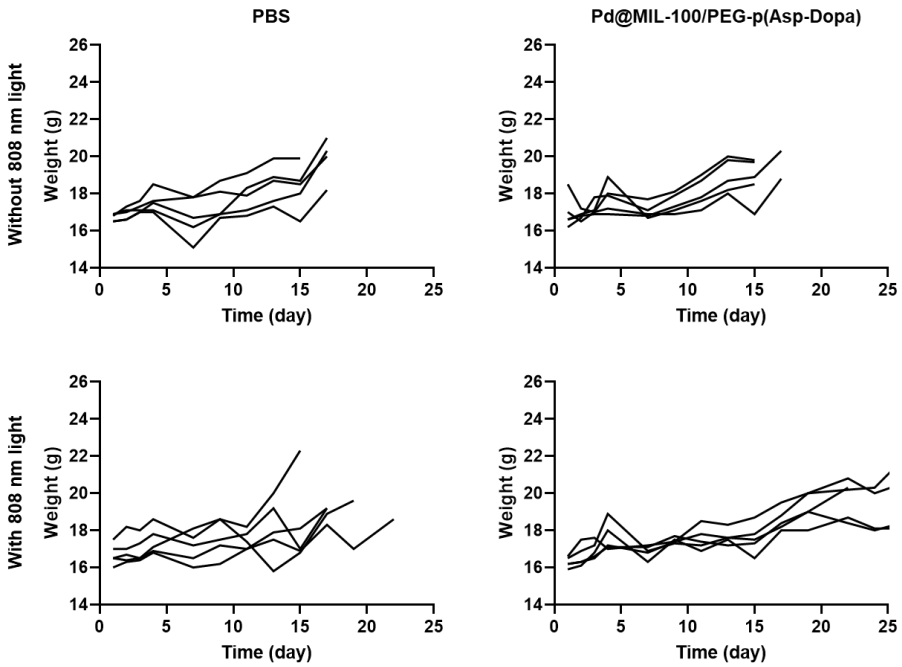

Figure 4.9 The body weight of mice with various treatments (PBS and Pd@MIL-100(Fe)/PEG-p(Asp-Dopa) with or without NIR light irradiation). The body weight was monitored every 2 days for 25 days. Each line represents an individual mouse (n = 5). The figure was adopted from S. W. Li *et al.* (2023) with the permission.

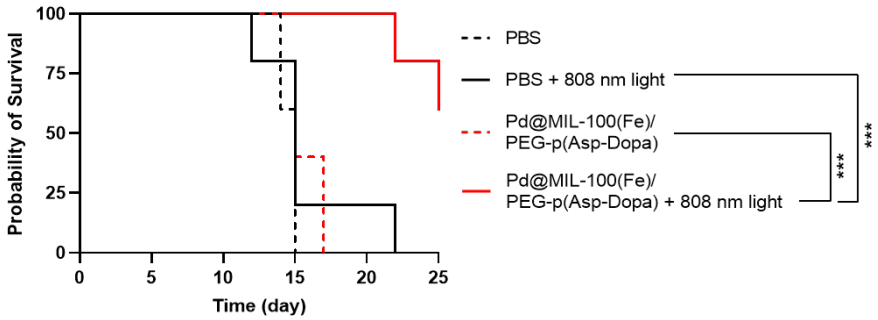

Figure 4.10 The survival curve of mice treated with PBS and Pd@MIL-100(Fe)/PEG-p(Asp-Dopa) with or without NIR light irradiation. The black lines indicated control (PBS) while red lines represented Pd@MIL-100(Fe)/PEG-p(Asp-Dopa) treated mice. The mice treated without NIR 808 nm light were shown in solid lines while mice treated with NIR 808 nm laser was depicted in dashed lines. The figure was adopted from S. W. Li *et al.* (2023) with the permission. (Data are presented as mean ± SD; *** indicated $p < 0.005$; p values are calculated via Kaplan-Meier survival analysis; n = 5 mice per group)

Additionally, the assessment of temperature changes within the tumor during NIR 808 nm light irradiation was conducted using both a digital thermometer and a thermal camera. This investigation aimed to comprehensively evaluate the photothermal effects within tumor tissues induced by Pd@MIL-100(Fe)/PEG-p(Asp-Dopa) as a potent anticancer photothermal therapy agent. B16F10 tumor-bearing mice received intravenous injections of 25 mg/kg (based on Pd content) Pd@MIL-100(Fe)/PEG-p(Asp-Dopa). Subsequently, NIR 808 nm irradiation at 1 W/cm² for 30 minutes was applied, and the temperature changes were recorded. The results demonstrated that different from PBS-treated group, Pd@MIL-100(Fe)/PEG-p(Asp-Dopa) significantly increased the temperature within the tumors. Specifically, tumors treated with PBS exhibited a temperature rise up to 42°C during irradiation, whereas those treated with Pd@MIL-100(Fe)/PEG-p(Asp-Dopa) experienced a remarkable increase surpassing 50°C **(Figure 4.11)**. Thermal imaging further emphasized these findings, showcasing a substantial elevation in temperature to 51.6°C in tumors subjected to treatment of Pd@MIL-100(Fe)/PEG-p(Asp-Dopa), while tumors with PBS reached 42.3°C **(Figure 4.12)**. Interestingly, similar to a previous study utilizing gold nanorods embedded in MIL-100(Fe), which succeeded in increasing the temperature within the tumors to higher than 50°C with NIR light at the energy density of 1 W/cm^2, our results demonstrated the capability to escalate the temperature of tumors over 50°C (Chien *et al.*, 2021). This achievement strongly correlates with the observed tumor ablation and remission in our antitumor experiments **(Figure 4.8)**. Moreover, the maintenance of elevated temperatures even after 30 minutes of irradiation underscores the sustained and effective photothermal impact of Pd@MIL-100(Fe)/PEG-p(Asp-Dopa) in destructing tumor tissues. This sustained high temperature following the NIR 808 nm irradiation further supports the efficacy of MOF/polymer hybrids for inhibiting tumor growth, solidifying its potential as a robust photothermal therapeutic strategy.

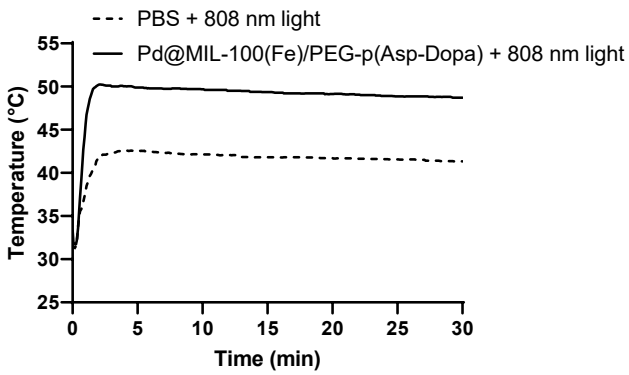

Figure 4.11 The intratumoral temperature of B16F10 melanoma bearing mice. After 1 day of the intravenous injection of PBS (control, solid line) and Pd@MIL-100(Fe)/PEG-p(Asp-Dopa) (25 mg/kg, based on Pd, dashed line), NIR 808 nm light was applied for 30 min (1 W/cm^2). The figure was adopted from S. W. Li *et al.* (2023) with the permission.

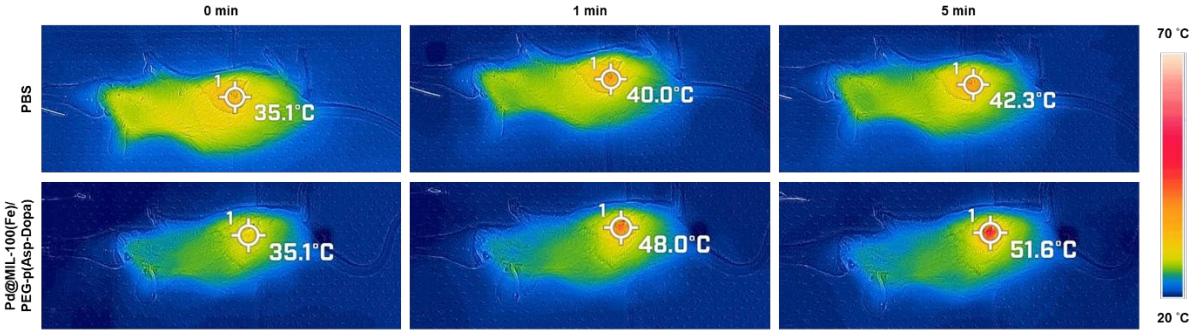

Figure 4.12 The thermal images of B16F10 melanoma bearing mice. The images were taken during the irradiation of NIR 808 nm light shown in Figure 4.11. The figure was adopted from S. W. Li *et al.* (2023) with the permission.

4.3.5 In vivo Toxicity of Pd@MIL-100/PEG-p(Asp-Dopa) hybrids

Assessing the biocompatibility of nanoparticles intended for cancer treatment is a pivotal aspect. In order to explore the toxicity of MOF/polymer hybrids, we evaluated the sereum level of several biomarkers, such as aspartate aminotransferase (AST) and alanine aminotransferase (ALT) to evaluate toxicity in liver, blood urea nitrogen (BUN) and creatinine (CRE) to assess the function of kidney, and total protein (TP) for determination of general toxic responses. In **Figure 4.13**, our analysis did not reveal discrepancy between PBS-treated group and the mice treated with 25 mg/kg of Pd@MIL-100(Fe)/PEG-p(Asp-Dopa) (based on Pd). These comparable biomarkers underscore the safety of Pd@MIL-100(Fe)/PEG-p(Asp-Dopa).

Additionally, through *in vitro* and *in vivo* assessments, both Pd@MIL-100(Fe) and Pd@MIL-100(Fe)/polymer hybrids revealed low toxicities in the previous sections. The examination of cell viability indicated negligible cellular toxicity in the absence of NIR 808 nm light irradiation, showing the concept that these nanomaterials pose minimal risk to cell viability under normal physiological conditions without the external triggering stimulus of NIR irradiation **(Figure 4.3)**. Moreover, mice treated with Pd@MIL-100(Fe)/PEG-p(Asp-Dopa) in conjunction with NIR 808 nm light exhibited no adverse responses. The maintenance of comparable body weights among mice across all treatment groups further supports the concept of minimal risk associated with these materials **(Figure 4.9)**. The absence of significant fluctuations in body weight signifies the absence of systemic adverse reactions.

Previous studies have shown the safety of MIL-100(Fe) and Pd-NPs (Quijia *et al.*, 2021; N. Singh *et al.*, 2021). Additionally, high lethal dose 50 (LD_{50}) values reported for individual components used in Pd@MIL-100(Fe)/polymer hybrids, including Fe (30,000 mg/kg), trimesic acid (8,400 mg/kg), Pd-NPs (2,700 mg/kg), and PEG (22,000 mg/kg) further affirm the low risk of acute toxicity associated with each constituent (Egorova & Ananikov, 2017; Q. Yang *et al.*, 2016). Despite the relatively high dose (25 mg/kg based on Pd) administered in mice, with

these findings, PEG-p(Asp-Dopa)-coated Pd@MIL-100 still proved its high biocompatibility even at high dose. Nevertheless, further improvements for Pd@MIL-100(Fe)/polymer hybrids in tumor tissue accumulation could potentially yield better antitumor effects at lower dosages. This research paves the road for advancements in cancer treatment strategies based on MOFs as the drug delivery system.

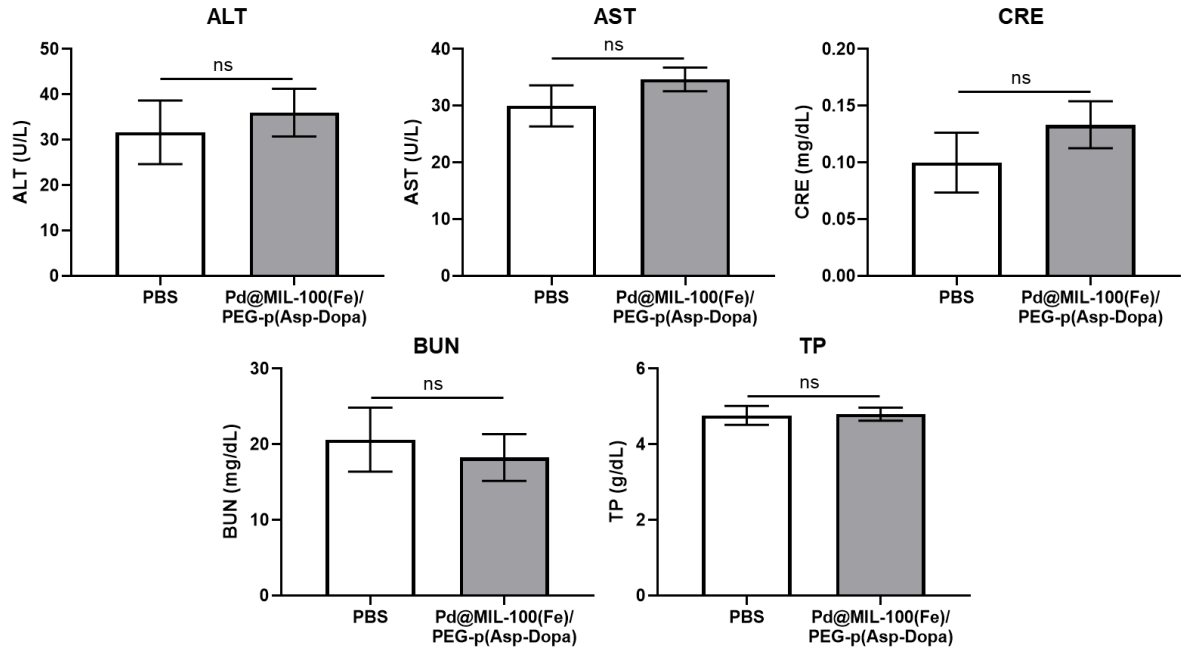

Figure 4.13 The toxicity assay in C57BL/6j mice. The level of serum alanine aspartate aminotransferase (AST), aminotransferase (ALT), blood urea nitrogen (BUN), creatinine (CRE), and total protein (TP) was quantified at 24 h post intravenous injection of PBS and 25 mg/kg Pd@MIL-100(Fe)/PEG-p(Asp-Dopa) (based on Pd). The figure was adopted from S. W. Li *et al.* (2023) with the permission. (Data are presented as mean ± SD; ns indicated not significant; *p* values are calculated via t-test; n = 3 mice per group)

4.4 Summary

The Pd@MIL-100(Fe)/polymer hybrids were evaluated for their photothermal therapeutic potential. Melanoma B16F10, representing a highly aggressive form of skin cancer and a clinically relevant target for photothermal therapy, was chosen as the primary model. Through cellular uptake analysis, it became evident that the incorporation of PEG-p(Asp-Dopa) on Pd@MIL-100(Fe) significantly enhanced its accumulation within B16F10 cells. *In vitro* cellular viability assays demonstrated the substantial photothermal killing effects of Pd@MIL-100(Fe)/polymer hybrids, with no detectable toxicity observed in the absence of NIR 808 nm light irradiation. Notably, the introduction of Pd@MIL-100(Fe)/PEG-p(Asp-Dopa) not only extended the circulation period in blood but also increased tumor accumulation while mitigating accumulation in the liver. This underscored the pivotal role of surface stabilization through PEG block copolymer such as PEG-p(Asp-Dopa) to facilitate pharmacokinetics. Upon administration of Pd@MIL-100(Fe)/PEG-p(Asp-Dopa) and irradiating with NIR 808 nm light, significant inhibition of B16F10 melanoma tumor growth was observed, with complete eradication in 2 out of 5 mice. Moreover, the survival of these mice was significantly prolonged, indicating the effectiveness of PTT facilitated by Pd@MIL-100(Fe)/PEG-p(Asp-Dopa). Additionally, across all treatment groups, the body weights of the mice remained comparable. Further, the biomarkers evaluated, such as ALT, AST, CRE, BUN, and TP, showed no discernible changes after Pd@MIL-100(Fe)/PEG-p(Asp-Dopa) injection, affirming the low health risk and high biocompatibility. Although the effective dosage utilized was relatively high at 25 mg/kg (based on Pd), these results strongly advocate for the efficacy of PEG-p(Asp-Dopa) as an effective surface protection strategy for Pd@MIL-100(Fe). It not only enhances tumor accumulation but also demonstrates antitumor capabilities without any observable adverse effects. The future improvements on the MOF/polymer hybrids formulation based on this research warrant the better antitumor efficacy at lower dosages.

Chapter 5.

Imaging capability of Pd@MIL-100/polymer hybrid

5.1 Introduction

In the realm of cancer theranostics, three crucial components stand out: tumor targeting, precise therapy, and imaging capabilities. In **Chapter 4**, Pd@MIL-100(Fe)/PEG-p(Asp-Dopa) exhibited improved tumor accumulation and successful PTT against melanoma B16F10 tumors, without any observable adverse effects. Consequently, in order to showcase Pd@MIL-100(Fe)/polymer hybrids as a versatile cancer theranostic platform, we introduced three imaging technologies into the Pd@MIL-100(Fe)/polymer hybrids.

MRI stands as a potent tumor imaging tool, especially when contrast agents like Gd-NPs are introduced, amplifying the contrast between tumors and surrounding healthy tissues. MIL-100(Fe) displays promising potential as an MRI contrast agent (P. Horcajada *et al.*, 2010). Fluorescence-based imaging methods are equally established for real-time drug tracking in the bloodstream and tumor imaging (K. Wang *et al.*, 2023). Common fluorescent dyes like fluorescein isothiocyanate (FITC), cyanine 5 (Cy5), and indocyanine green have been widely used for cancer imaging (Mieog *et al.*, 2022). In this study, we explore both MRI- and fluorescence-based imaging technologies with Pd@MIL-100(Fe)/polymer hybrids showcasing its potential to be the versatile cancer theranostic platform.

In this chapter, beginning by determining the MRI relaxivity of Pd@MIL-100(Fe) and its polymer hybrids. Next, Cy5 was conjugated to PEG-p(Asp-Dopa) and coated onto Pd@MIL-100(Fe) for real-time particle tracking in blood circulation. Additionally, FITC was loaded into Pd@MIL-100(Fe), followed by surface stabilization with block copolymers. These FITC-loaded hybrids were used to track particles within B16F10 cancer cells. Finally, IVIS was employed to visualize the FITC-loaded hybrids within tumors and other tissues for tumor imaging.

5.2 Materials and methods

5.2.1 Materials

Fluorescein isothiocyanate (FITC) sodium salt was obtained from Tokyo Chemical Industry Co. Ltd. (Tokyo, Japan). Phosphate-buffered saline (PBS), trypsin/EDTA solution, and Hoechst® 33342 solution were sourced from ThermoFisher Scientific (Waltham, USA). High-glucose Dulbecco's Modified Eagle's Medium (DMEM) and Cyanine 5 (Cy5) NHS ester were obtained from Sigma-Aldrich (St. Louis, MO, USA). The penicillin/streptomycin stock solution was procured from Fujifilm Wako (Osaka, Japan). CellBanker was acquired from Takara (Kyoto, Japan). Isoflurane was obtained from Pfizer (New York, NY, USA). PD-10 desalting columns packed with Sephadex G-25 resin were purchased from Cytiva (Washington, D.C., USA).

5.2.2 Cell lines and animal model

The B16F10 melanoma cancer cell line was procured from the Cell Bank at Riken BioResource Center (Kyoto, Japan). The cells were cultured in high-glucose DMEM (4500 mg/l glucose, L-glutamine, sodium pyruvate, and sodium bicarbonate), supplemented with 10% FBS and 100 U/mL penicillin-streptomycin, in a 37°C incubator with 95% air and 5% CO2. Passage of the cells was performed every 3-4 days, using trypsin/EDTA solution (0.025% trypsin and 0.01% EDTA in PBS), when the cells reached approximately 80% confluency. Frozen cell stocks were prepared using CellBanker.

In vivo experiments were conducted on 5-week-old female C57BL/6j black mice, obtained from The Jackson Laboratory (Kanagawa, Japan). All animal experiments conducted during this research were authorized by The University of Tokyo adhering to the Guidelines for the Care and Use of Laboratory Animals (approval number: A2023E005-01).

5.2.3 Synthesis of fluorescent Pd@MIL-100/polymer hybrid

To facilitate the tracking of Pd@MIL-100 and Pd@MIL-100/polymer hybrids, FITC and Cy5 was employed as a labeling agent. For FITC labeling, Pd@MIL-100 with a concentration of 1 mg/mL was combined with FITC sodium salt at a weight ratio of Pd@MIL-100:FITC of 1:10 in water. The mixture underwent overnight stirring at room temperature. FITC-labeled Pd@MIL-100 was meticulously washed five times with water to remove any residual free FITC, and the remaining free FITC was assessed using a multi-well plate reader (Spark, Tecan, Männedorf, Switzerland) with an excitation wavelength of 488 nm and an emission wavelength of 520 nm. The resulting FITC-loaded Pd@MIL-100 was then coated with the polymers outlined in *section 3.2.4*.

For Cy5 labeling, Cy5 NHS ester was dissolved in DMF at a concentration of 20 mg/mL. PEG-p(Asp-Dopa) polymers were dissolved in a 50 mM $NaHCO_3$ solution (pH = 8.5) and mixed with Cy5 NHS ester at a molar ratio of polymer to Cy5 of 1:3. The mixture was stirred for 12 hours. The resulting Cy5-labeled PEG-p(Asp-Dopa) polymers were purified using PD-10 desalting columns. The purified Cy5-labeled PEG-p(Asp-Dopa) polymers were collected by lyophilization, yielding a blue-colored fluffy powder. Subsequently, these Cy5-labeled PEG-p(Asp-Dopa) polymers were coated onto Pd@MIL-100 as outlined in *section 3.2.4*.

5.2.4 Characterization of fluorescent Pd@MIL-100/polymer hybrid

The hydrodynamic diameter and polydispersity index (PDI) of fluorescent Pd@MIL-100/polymer hybrid were determined using dynamic light scattering (DLS) with the Zetasizer Nano-ZS instrument (Malvern Panalytical, Worcestershire, UK). The hybrids were dispersed in deionized water at an approximate concentration of 0.1 mg/mL and loaded into a low-volume quartz cuvette (ZEN2112). Measurements were carried out at 25°C with a 50 mW frequency-doubled DPSS Nd:YAG laser (λ=532 nm) at a detection angle of 173°. The average diameter

and PDI were calculated using the cumulant method to describe the particle size characteristics.

Furthermore, the intensity of fluorescent Pd@MIL-100/polymer hybrid was assessed. The hybrids, dispersed in deionized water at an approximate concentration of 0.1 mg/mL, were introduced into a quartz 96-well plate at a volume of 100 μL. The fluorescence intensity was measured with a multi-well plate reader (Spark, Tecan, Männedorf, Switzerland) using an excitation wavelength of 488 nm and an emission wavelength of 520 nm for FITC and an excitation wavelength of 633 nm and an emission wavelength of 670 nm.

5.2.5 Determination of MRI capability

To determine the relaxivity of MOFs and MOF/polymer hybrids that were synthesized in this study, the longitudinal (R_1, s^{-1}) and transverse (R_2, s^{-1}) relaxation rate constants was quantified by using a 0.47 T minispec mq20 NMR analyzer (^1H, 19.95 MHz, 36.5°C, Bruker, Massachusetts, USA). Before the assessment of relaxivity, ICP-MS (7900, Agilent, California, USA) was used to quantify the concentrations of Fe and Pd in all samples. Next, Milli-Q water was used to reconstitute the samples and the samples were diluted to 1-, 0.5-, 0.25-, and 0.125-fold from the original solution (10 mg/mL, based on the weight of particles). The inversion recovery method was employed to measure the longitudinal relaxation time (T_1, s), and the Carr-Purcell-Meiboom-Gill (CPMG) method was utilized for obtaining the transverse relaxation time (T_2, s). The resulting R_1 ($1/T_1$) and R_2 ($1/T_2$) values were plotted against the Fe concentration, and the r_1 and r_2 relaxivities ($s^{-1}mM^{-1}$) were determined through linear regression analysis.

5.2.6 In vitro cellular uptake

Melanoma cancer cells, B16F10, were cultured in a glass-bottom 8-well chamber slide, with 20,000 cells seeded per well. Following an overnight incubation, FITC-loaded MOF/polymer hybrids were added at a final concentration of 0.5 mg/mL. After 24 hours, cells were washed three times with PBS to remove residual free FITC-loaded MOFs, and the cell nuclei were stained with Hoechst® 33342. Following a 10-minute staining period, cells were washed again three times with PBS. An additional 200 μL PBS was added before subjecting the cells to confocal laser scanning microscopy (LSM-780, Zeiss, Oberkochen, Germany). Images of the cells were captured with an excitation wavelength of 405 nm and an emission wavelength of 450 nm for imaging the nucleus, and with an excitation wavelength of 488 nm and an emission wavelength of 520 nm for visualizing the FITC-loaded MOFs.

5.2.7 Monitoring dynamics in blood circulation

The blood circulation dynamic of Cy5 labeled Pd@MIL-100/PEG-p(Asp-Dopa) was monitored with multiphoton confocal scanning microscopy, A1R MP^+ (Nikon, Tokyo, Japan). The Cy5 labeled Pd@MIL-100/PEG-p(Asp-Dopa) was suspended in PBS at the concentration of 1 mg/mL. The C57BL/6j black mouse was anesthetized with isoflurane and the 30G needle connected to a loop with a 1 mL syringe was inserted into the tail vein. The ear lobe of the mouse was mounted to a 50 mm glass bottom dish. A 40× water lens was connected to the A1R MP^+. The location of the vein and artery was focused. After starting the scanning with the excitation wavelength of 633 nm and an emission wavelength of 670 nm, 100 μL Cy5 labeled Pd@MIL-100/PEG-p(Asp-Dopa) was intravenously injected. The dynamic was monitored for 12 h. The fluorescence intensity was measured with NIS element software (Nikon, Tokyo, Japan).

5.2.8 Fluorescent Pd@MIL-100/polymer hybrid imaging by IVIS

To evaluate the tumor targeting of FITC labeled Pd@MIL-100/polymer hybrid, *in vivo* fluorescence imaging was performed using an IVIS spectrum system (Perkinelmer, Connecticut, USA). B16F10 cells (1×10^6 cells/mouse) were implanted subcutaneously in C57BL/6j black mice. When the tumor volume reached about 50 mm^3, the mice were intravenously injected with 100 μL of 1 mg/mL FITC labeled Pd@MIL-100/polymer hybrid solution. After 24 h, the fluorescence images of the mice were acquired with IVIS using an excitation wavelength of 488 nm and an emission wavelength of 520 nm with exposure time of 1 minute. Then, the mice were euthanized, and the tumor, liver, kidney, spleen, heart, and lung were harvested and imaged with IVIS.

5.3 Results and discussions

5.3.1 Determination of MRI capability

In this investigation, our focus was on enhancing the imaging capabilities of Pd@MIL-100(Fe), exploring its potential for MRI and fluorescence imaging techniques. Initially, we assessed its applicability as an MRI contrast agent, building upon prior findings that MIL-100(Fe) itself can serve this purpose (P. Horcajada *et al.*, 2010). To examine the inherent MRI potential, we suspended MIL-100(Fe), Pd@MIL-100(Fe), and Pd@MIL-100(Fe)/polymer hybrids in water at a concentration of 1 mg/mL and conducted preliminary MRI scans on these solutions. The initial results displayed variations in both T_1 and T_2 weighted images among MIL-100(Fe), Pd@MIL-100(Fe), and Pd@MIL-100(Fe)/polymer hybrids **(Figure 5.1)**. Further, we determined the relaxivity to ascertain the potential of these hybrids as contrast agents. **Figure 5.2 and Table 5.1** revealed that MIL-100(Fe), Pd@MIL-100(Fe), Pd@MIL-100(Fe)/PEG-p(Asp), and Pd@MIL-100(Fe)/PEG-p(Asp-Dopa) exhibited similar r_1 and r_2 relaxivity values, approximately ranging between 0.2-0.5 s^{-1} mM^{-1}. These values signify their promising utility as MRI contrast probes, aligning closely with the reported relaxivity values for Cu-based MOFs that are considered as the potential MRI contrast agents (B. Li *et al.*, 2018). Consequently, the MIL-100(Fe)-based systems developed in this study present as a promising MRI contrast agent.

Table 5.1 Relaxivity for MIL-100(Fe), Pd@MIL-100(Fe), Pd@MIL-100(Fe)/PEG-p(Asp), and Pd@MIL-100(Fe)/PEG-p(Asp-Dopa). The table was adopted from S. W. Li *et al.* (2023) with the permission.

Materials	r_1 (s^{-1} mM^{-1})	r_2 (s^{-1} mM^{-1})
MIL-100(Fe)	0.31	0.58
Pd@MIL-100(Fe)	0.19	0.50
Pd@MIL-100(Fe)/PEG-p(Asp)	0.18	0.31
Pd@MIL-100(Fe)/PEG-p(Asp-Dopa)	0.20	0.33

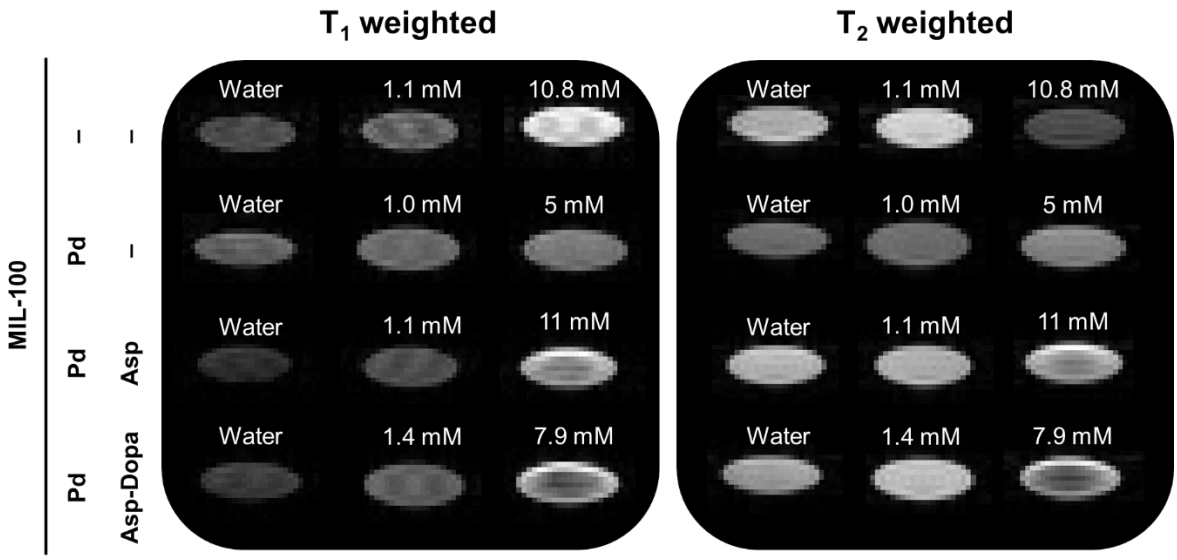

Figure 5.1 The preliminary MRI images of MIL-100(Fe), Pd@MIL-100(Fe), and Pd@MIL-100(Fe)/polymer hybrids. The MRI images was taken with the Bruker AVANCE™ III. The concentration labled on the images indicated the Fe level determined with ICP-MS.

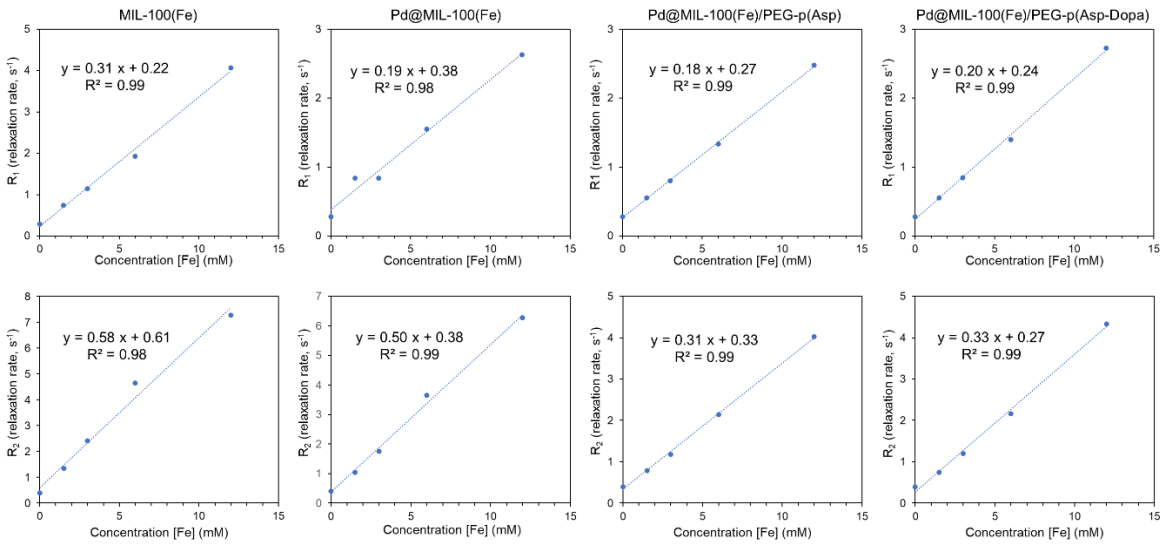

Figure 5.2 The calculated relaxivity of MIL-100(Fe), Pd@MIL-100(Fe), and Pd@MIL-100(Fe)/polymer hybrids. The figure was adopted from S. W. Li *et al.* (2023) with the permission.

5.3.2 Characterization of fluorescent Pd@MIL-100/polymer hybrid

In addition to the MRI imaging technique, the fluorescent imaging technique was studied in Pd@MIL-100(Fe). To equip the fluorescent imaging capability to the Pd@MIL-100(Fe), there are two compartments that can be utilized to carry fluorescent signal: MOF and polymer. Therefore, we implemented two approaches: the loading of fluorescent dye, FITC, into Pd@MIL-100(Fe), and the conjugation of fluorescent dye, Cy5, onto the PEG-p(Asp-Dopa) polymers to demonstrate the versatility of Pd@MIL-100(Fe)/polymer hybrids in imaging. We first characterized the hydrodynamic diameter and the fluorescent intensity of the nanoparticles made from the two approaches.

From the results of diameter, the particles size of FITC loaded Pd@MIL-100(Fe) is similar to non-loaded Pd@MIL-100(Fe) **(Figure 5.3)**. Consistently, after the surface protection of PEG-p(Asp) or PEG-p(Asp-Dopa), the FITC loaded Pd@MIL-100(Fe)/polymer hybrids exhibited the same diameter to their non-loaded compartments **(Figure 5.3)**. Additionally, the Pd@MIL-100(Fe)/PEG-p(Asp-Dopa)-Cy5 also exhibited the similar particle size compared to that of the non-Cy5-labeled MOF/polymer hybrids **(Figure 5.3)**. These data indicated that the loading of FITC into Pd@MIL-100(Fe) and the conjugation of Cy5 to PEG-p(Asp-Dopa) did not affect the size of these nanoparticles.

Furthermore, the fluorescent intensity of these nanoparticles was investigated. The signals of FITC and Cy5 in water and Pd@MIL-100(Fe) were about 30 RFU indicating low fluorescent background **(Table 5.2)**. After loading of FITC, both Pd@MIL-100(Fe) and Pd@MIL-100(Fe)/polymer hybrids exhibited the fluorescent intensity of more than 1500 RFU that is 50-fold higher compared to non-loaded ones **(Table 5.2)**. Similarly, the Pd@MIL-100(Fe)/PEG-p(Asp-Dopa)-Cy5 showed the fluorescent intensity of more than 2000 RFU **(Table 5.2)**. These results indicated the imaging potential of these fluorescent MOF/polymer hybrids.

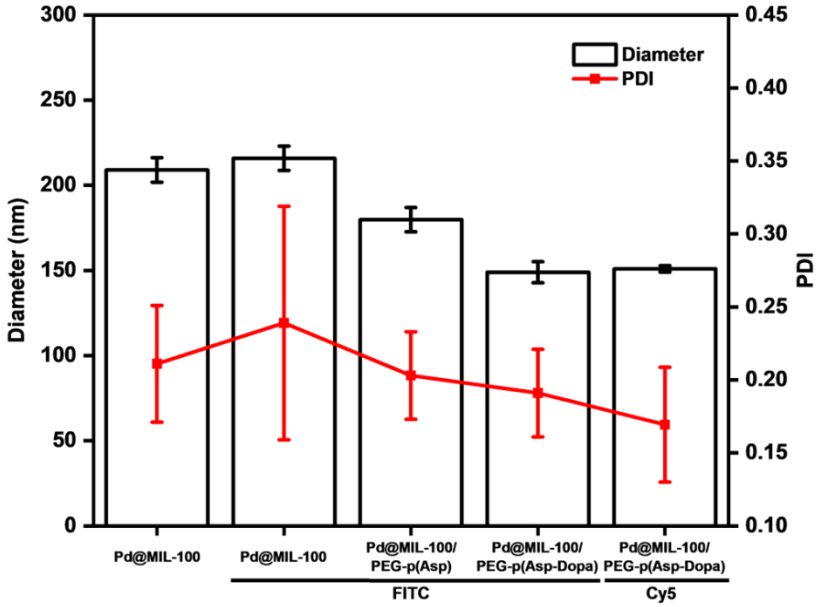

Figure 5.3 The hydrodynamic diameter and PDI of FITC loaded Pd@MIL-100(Fe), and Pd@MIL-100(Fe)/polymer hybrids as well as Cy5 labled Pd@MIL-100(Fe)/PEG-p(Asp-Dopa). The diameter is shown in bar graph and the PDI in red line.

Table 5.2 The fluorescence intensity of FITC loaded Pd@MIL-100(Fe), and Pd@MIL-100(Fe)/polymer hybrids as well as Cy5 labled Pd@MIL-100(Fe)/PEG-p(Asp-Dopa).

Materials	FITC (RFU)	Cy5 (RFU)
H_2O	32 ± 18	37 ± 13
Pd@MIL-100(Fe)	28 ± 11	31 ± 16
Pd-FITC@MIL-100(Fe)	1845 ± 528	–
Pd-FITC@MIL-100(Fe)/PEG-p(Asp)	1677 ± 260	–
Pd-FITC@MIL-100(Fe)/PEG-p(Asp-Dopa)	1551 ± 301	–
Pd@MIL-100(Fe)/PEG-p(Asp-Dopa)-Cy5	–	2019 ± 425

5.3.3 Dynamics in blood circulation

To demonstrate the application of Cy5 labeled Pd@MIL-100(Fe)/PEG-p(Asp-Dopa), we implemented the technique of intravital confocal microscopy. Traditionally, the dynamics of metal nanoparticles in the blood circulation is determined by sampling the blood in different timepoint and measure the concentration of metal with ICP-MS. In this experiment, with the help of fluorescent signal, the dynamics of the nanoparticles in the blood stream can be observed in real-time. The Pd@MIL-100(Fe)/PEG-p(Asp-Dopa)-Cy5 was suspended in 100 μL PBS at the concentration of 5 mg/mL and intravenously injected into mice's tail vein. The video of the blood circulation was captured with intravital confocal microscopy. Before injection, there is no observable red signal. Once after injection, a strong red fluorescence can be detected in the blood vessels. The fluorescent signal was still observable after 100 min post injection **(Figure 5.4)**. To further examined the results, we quantified the intensity of the fluorescent signal and normalized to the maximum value detected. In **Figure 5.5**, the signal of Cy5 went up immediately and gradually reduced. After 1 hour, there was about 15% of Cy5 signal remaining in the blood vessel while about 5% of Cy5 signal remained after 5 hours. These results are similar to the blood circulation results that we determined with ICP-MS indicating the successful imaging of Pd@MIL-100(Fe)/PEG-p(Asp-Dopa)-Cy5 and the potential to be used for the fluorescent imaging applications. Additionally, in **Figure 4.5**, the residual percentage of MOF/polymer hybrids was determined by the Pd content using ICP-MS, indicating the presence of Pd@MIL-100(Fe). Conversely, in **Figure 5.5**, the percentage was calculated based on the fluorescent intensity originating from Cy5-labeled PEG-p(Asp-Dopa). The comparable blood circulation dynamics between the two figures suggested that the polymers were stably complexed onto Pd@MIL-100(Fe) and circulated together for 6 hours. Hence, the results from TGA and the similarity in blood circulation dynamics affirm that the polymer, PEG-p(Asp-Dopa), is successfully complexed with Pd@MIL-100(Fe).

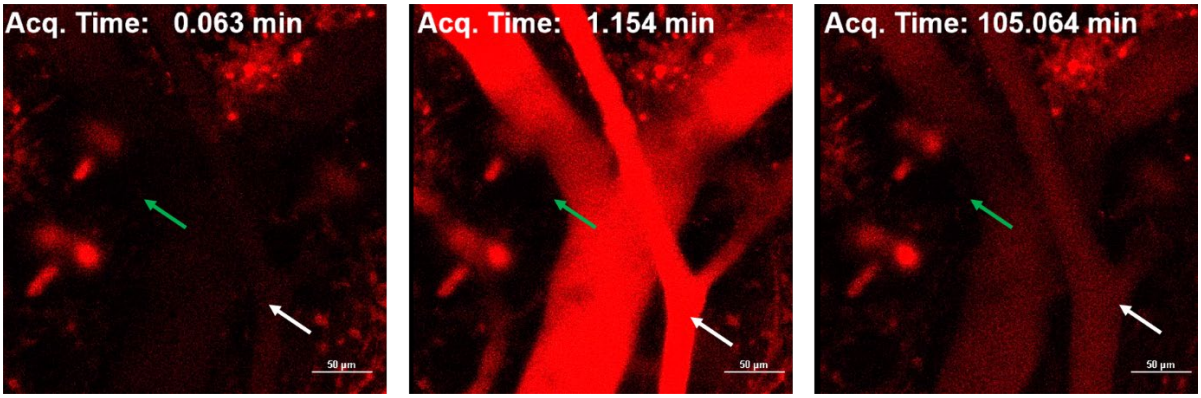

Figure 5.4 The dynamic of Cy5 labeled Pd@MIL-100(Fe)/PEG-p(Asp-Dopa) in blood vessels visualized with intravital confocal microscopy. Green arrow indicated the skin (paraphral tissue), and white arrow indicated the blood vessel.

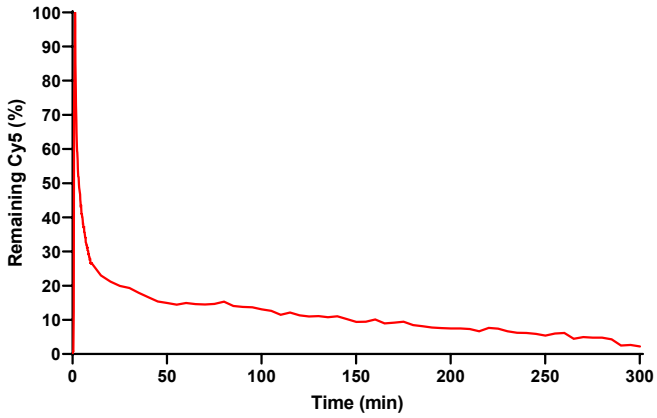

Figure 5.5 Quantification of the remaining fluorescence intensity of Cy5 labeled Pd@MIL-100(Fe)/PEG-p(Asp-Dopa) in the blood vessel. All the fluorescence intensity of Cy5 recorded was normailized to the maximum detected level.

5.3.4 In vitro cellular uptake

Furthermore, in addition to Cy5-labeled Pd@MIL-100(Fe)/PEG-p(Asp-Dopa), we present another example of fluorescent imaging approach for MOFs by using FITC-loaded Pd@MIL-100(Fe) and Pd@MIL-100(Fe)/polymer hybrids. To enable the tracking of these nanoparticles, FITC was initially incorporated into the structure of Pd@MIL-100(Fe). Following this, the surface of FITC-loaded Pd@MIL-100(Fe) was shielded using PEG-p(Asp) and PEG-p(Asp-Dopa). The characteristics of these FITC-loaded nanoparticles were confirmed in **Figure 5.3** and **Table 5.2**, supporting their potential for fluorescent imaging applications. Analysis through confocal laser scanning microscopy unveiled that both FITC-loaded Pd@MIL-100(Fe) and Pd@MIL-100(Fe)/polymer hybrids were detectable within melanoma B16F10 cells. Remarkably, only FITC-loaded Pd@MIL-100(Fe) stabilized by PEG-p(Asp-Dopa) exhibited a more pronounced green signal within the cytoplasm compared to FITC-loaded Pd@MIL-100(Fe) and Pd@MIL-100(Fe)/PEG-p(Asp) **(Figure 5.6)**. Further quantification of the fluorescent intensity highlighted that the mean fluorescent intensity of FITC-loaded Pd@MIL-100(Fe)/PEG-p(Asp-Dopa) significantly surpassed that of FITC-loaded Pd@MIL-100(Fe) and Pd@MIL-100(Fe)/PEG-p(Asp) **(Figure 5.7)**. Notably, the cellular uptake outcomes measured by fluorescent intensity **(Figure 5.7)** aligned closely with the results obtained through ICP-MS **(Figure 4.3)**, emphasizing the feasibility of FITC loaded Pd@MIL-100(Fe) for tracking. Once more, the increased cellular uptake facilitated by the surface protection of PEG-p(Asp-Dopa) underlined its promise in stabilizing the surface of Pd@MIL-100(Fe) for the biomedical applications.

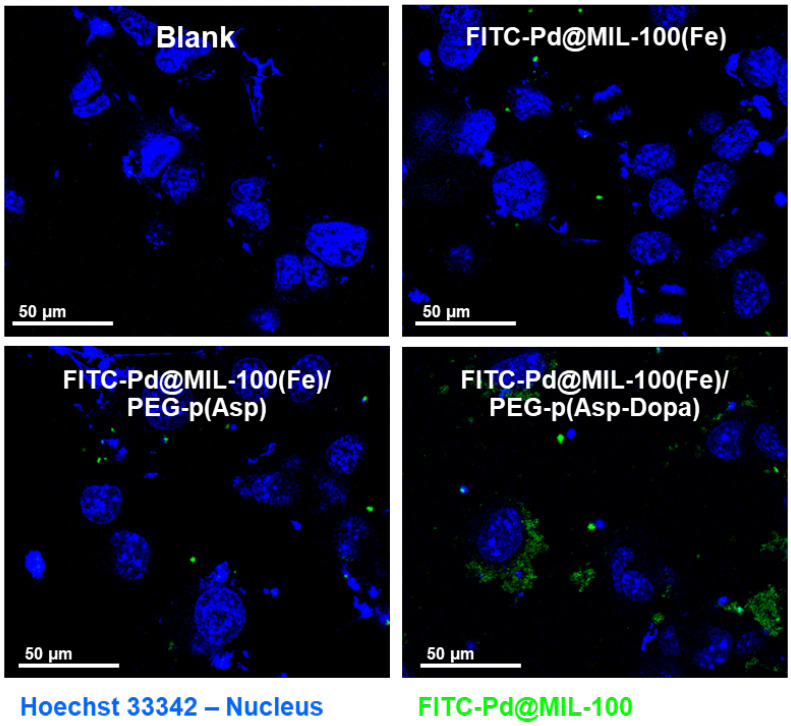

Figure 5.6 The cellular upatke of FITC loaded Pd@MIL-100(Fe) and Pd@MIL-100(Fe)/polymer hybrids. The figure was adopted from S. W. Li *et al.* (2023) with the permission.

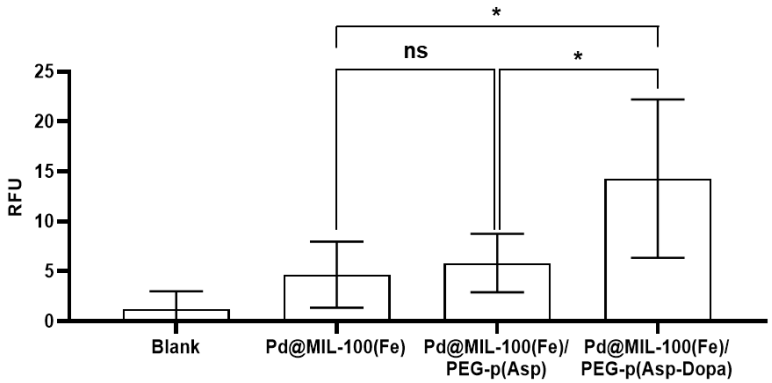

Figure 5.7 Quantification of FITC fluorescence intensity in confocal images. The figure was adopted from S. W. Li *et al.* (2023) with the permission. (Data are presented as mean fluorescence signal ± SD; ns indicated not significant; * indicated $p < 0.05$; 25 cells were measured per group)

5.3.5 Tumor accumulation of fluorescent Pd@MIL-100/polymer hybrid

To further investigate the utility of FITC-loaded Pd@MIL-100(Fe)/PEG-p(Asp-Dopa) in a mouse model, we implemented *in vivo* imaging technology via IVIS. In this experiment, C57BL/6j mice were subcutaneously injected with melanoma B16F10 cancer cells. Subsequently, FITC-loaded Pd@MIL-100(Fe)/PEG-p(Asp-Dopa) was administered intravenously through the tail vein at a concentration of 25 mg/kg (based on Pd). Analysis of IVIS images from the mice revealed FITC signals in tumors from 2 out of 3 mice, demonstrating observable tumor accumulation **(Figure 5.8)**. To further validate the usability and confirm the biodistribution of FITC-loaded Pd@MIL-100(Fe)/PEG-p(Asp-Dopa) in the mouse model, the mice were sacrificed, and tissue samples were collected for IVIS analysis. The IVIS images showed FITC signals in the tumors of 2 out of 3 mice, reaffirming tumor accumulation **(Figure 5.9)**. However, in accordance with previous findings and the biodistribution data illustrated in **Figure 4.7**, a substantial FITC signal was observed in the liver, spleen, but unexpectedly, in the kidneys (Simon-Yarza *et al.*, 2016). This discrepancy might arise from the potential release of free FITC dye, which was captured and excreted by the kidneys. In summary, this study demonstrated the diverse imaging potential of Pd@MIL-100(Fe) through MRI and fluorescence technologies, offering promising approaches for employing Pd@MIL-100(Fe)/polymer hybrid systems in cancer theranostics.

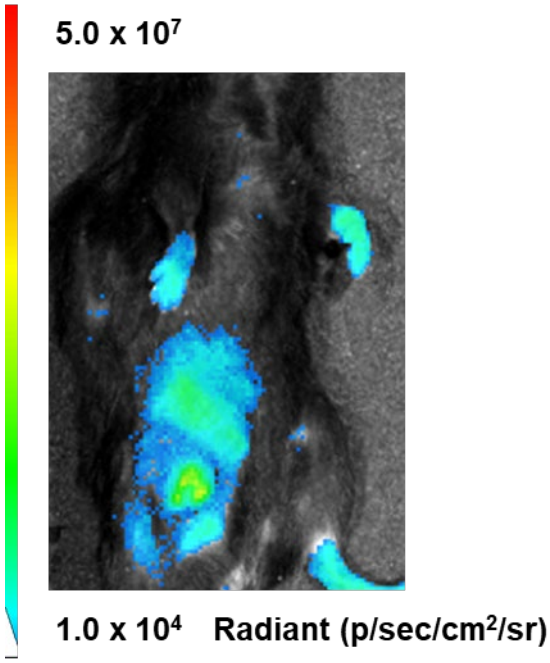

Figure 5.8 The IVIS images of mice treated with FITC loaded Pd@MIL-100(Fe)/PEG-p(Asp-Dopa) at the conclusion of 25mg/kg (based on Pd).

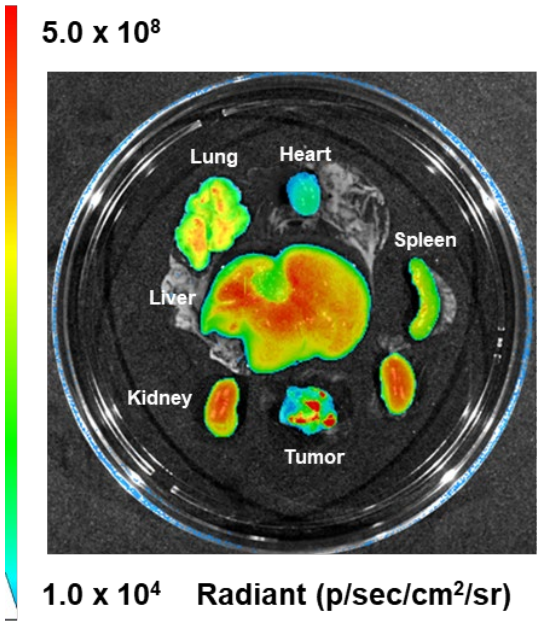

Figure 5.9 The IVIS images of the tissues including lung, heart, liver, spleen, kidney, and tumor collected from the mice treated with FITC loaded Pd@MIL-100(Fe)/PEG-p(Asp-Dopa) at the conclusion of 25mg/kg (based on Pd).

5.4 Summary

To showcase Pd@MIL-100(Fe) as a promising tool in cancer theranostics, we employed three distinct imaging methods for *in vitro* and *in vivo* assessments, including MRI and fluorescent technology. Initially, the relaxivity studies of Pd@MIL-100(Fe) and Pd@MIL-100(Fe)/polymer hybrids demonstrated their intrinsic potential as MRI contrast agents. Concurrently, we explored two approaches to achieve fluorescent Pd@MIL-100(Fe). Fluorescent dye incorporation into MIL-100(Fe) and PEG-p(Asp-Dopa) was pursued separately. In one example of creating fluorescent Pd@MIL-100(Fe)/polymer hybrids, we conjugated the commonly used fluorescent dye, Cy5, to the terminal amine of PEG-p(Asp-Dopa) and subsequently coated it onto the surface of Pd@MIL-100(Fe). We demonstrated the utility of Pd@MIL-100(Fe)/PEG-p(Asp-Dopa)-Cy5 for tracking dynamics in blood circulation. Using intravital confocal microscopy, we can perform real-time monitoring of Pd@MIL-100(Fe)/PEG-p(Asp-Dopa)-Cy5 levels in the bloodstream. The quantified blood level dynamics of Pd@MIL-100(Fe)/PEG-p(Asp-Dopa)-Cy5 closely matched results quantified with ICP-MS. In another demonstration involving fluorescent Pd@MIL-100(Fe)/polymer hybrids, we loaded the widely used fluorescent dye FITC into Pd@MIL-100(Fe) before the formation of MOF/polymer hybrids. This approach showcased applications in both *in vitro* and *in vivo* scenarios. Following treatment of B16F10 cells, we observed cellular uptake via confocal microscopy. Notably, FITC-loaded Pd@MIL-100(Fe)/PEG-p(Asp-Dopa) displayed the highest cellular uptake, consistent with results determined by ICP-MS. Finally, we illustrated the *in vivo* application of FITC-loaded Pd@MIL-100(Fe)/PEG-p(Asp-Dopa) using IVIS in B16F10 tumor-bearing mice. IVIS images clearly depicted fluorescent signals in the tumors of 2 out of 3 mice. Corresponding with biodistribution data from ICP-MS, we observed high accumulation in the liver and spleen. Overall, these findings underscore the versatile imaging potential of Pd@MIL-100(Fe) and its promising role in cancer theranostics.

Chapter 6.

Conclusions and future perspectives

6.1 Conclusion

The integration of tumor targeting, precise therapy, and monitoring within a single cancer treatment, theranostics holds significant promise for enhancing patients' quality of life. While this therapeutic concept is in its early stages within healthcare, advancing research and developing versatile, highly biocompatible theranostic platforms can unlock its full potential. This study aimed to create a versatile MOF/polymer hybrid platform for cancer theranostics. Leveraging the inherent advantages of Fe-based MOF, MIL-100(Fe), as the scaffold for multifunctional capabilities, coupled with polymeric surface stabilization for improved physiological stability, the Pd-NPs loaded MIL-100(Fe)/polymer hybrids showed promise in photothermal therapy against cancers and diverse imaging modalities. This hybrid model addresses shortcomings in the biomedical application of MOFs, offering a viable solution for multifunctional and combined therapy.

In this study, we developed a Pd-NPs loaded MIL-100(Fe) MOF model and characterized it thoroughly. To stabilize the surface in physiological conditions, a block copolymer was designed, integrating dopamine-modified PEG-p(Asp) with carboxylates and catechol in the side chain to establish a stable complex with the metals on the surface of MOFs. These elements were merged to create Pd@MIL-100(Fe)/polymer hybrids, exhibiting uniform size and favorable properties under physiological conditions. This system improved pharmacokinetics and demonstrated significant photothermal therapeutic efficacy both *in vitro* and *in vivo*. Additionally, we explored the integration of diverse imaging techniques, showcasing the versatility of Pd@MIL-100(Fe)/polymer hybrids as a promising platform for cancer theranostics.

One of the most promising photothermal agents among transitional metals is Pd. Extensive research has focused on developing Pd-NPs and their application in effective photothermal therapy (Rubio-Ruiz *et al.*, 2018). This study explores the integration of Pd-NPs into our system, showcasing the potential of MIL-100(Fe)'s porous structure to synthesize NPs within. Our aim is to establish Pd-NPs loaded MOF as an effective photothermal therapy against B16F10 tumors. Like many theranostic platforms, our system aims to offer a versatile, stable platform for loading diverse drugs while providing imaging capabilities for monitoring purposes. Our results demonstrated significant photothermal therapeutic effects against B16F10 tumors in mice using Pd-NPs and showcasing its potential for tumor imaging.

MOFs stand as versatile tools across various domains, including catalysis, gas or energy storage, and drug delivery. However, a significant challenge lies in the potential health risks associated with released metal ions and their instability under physiological conditions. MOFs based on metals like Cu, Fe, and Gd are particularly promising due to their intrinsic MRI contrast capabilities. Concerns arise regarding the toxicity of released Cu and Gd, leading to issues such as copperiedus and nephrogenic systemic fibrosis (Gallo-Bernal *et al.*, 2022). In contrast, Fe demonstrates higher tolerance than Gd and Cu. This distinction makes MIL-100(Fe) a promising candidate for cancer theranostics. Despite its potential, MIL-100(Fe) faces challenges in poor serum stability, hindering its application as a viable drug delivery solution (Simon-Yarza *et al.*, 2016).

In our MOF/polymer hybrids, the shielding effect of PEG offered by the PEG-p(Asp-Dopa) block copolymers prevents aggregation in physiological conditions, ensuring prolonged circulation in the bloodstream. Compared to other MOF systems, our hybrids exhibit improved stability and pharmacokinetics, leading to robust antitumor efficacy. Furthermore, the polymeric surface protection in our system presents possibilities for further conjugation. For instance, we demonstrated Cy5 conjugation, enabling real-time tracking of the dynamics in

blood circulation through intravital confocal microscopy. Additionally, these block copolymers can be readily tailored with other functional groups like azide groups, facilitating click chemistry for the addition of tumor-targeting ligands. The adaptable length of p(Asp-Dopa) offers versatility to suit various MOFs. As a result, our block copolymers hold promise for stabilizing other MOF systems, fostering their potential in cancer theranostics.

In conclusion, the Pd@MIL-100(Fe)/polymer hybrid system overcomes the drawbacks of poor stability and limited pharmacokinetics seen in conventional MOF systems. Our Pd@MIL-100(Fe)/PEG-p(Asp-Dopa) not only significantly enhanced tumor accumulation but also displayed considerable photothermal therapeutic efficacy, completely eradicating B16F10 tumors in 2 out of 5 treated mice. Moreover, our system showed promise in monitoring and tumor imaging through MRI and fluorescence-based technologies **(Figure 6.1)**. This research presents exciting possibilities for innovative cancer theranostic platforms based on MOF/polymer hybrids.

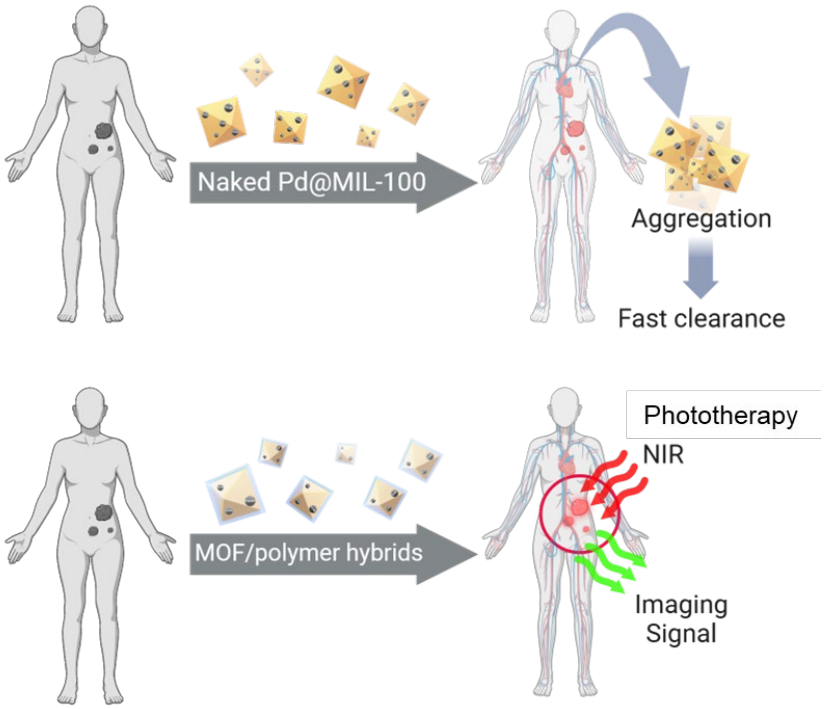

Figure 6.1 The prospect of MOF/polymer hybirds as the versatile cancer theranostic.

6.2 Future perspectives

Our findings highlight MIL-100(Fe) as a scaffold for creating metal NPs in the MOF, showing promise in generating photothermal agents. The integration of PEG block copolymer, PEG-p(Asp-Dopa), efficiently protected Pd@MIL-100(Fe), enhancing its blood circulation and accumulation in tumors. Despite the current high dosage of 25 mg/kg based on Pd, toxicity assessments revealed no adverse responses. Improvements in the size of Pd@MIL-100(Fe), block copolymer design, and incorporation of tumor-targeting ligands may enhance tumor accumulation, allowing for superior antitumor efficacy at lower doses and shorter period of NIR light exposure. Moreover, the adaptable nature of PEG-p(Asp-Dopa) for complexing with metals suggests its potential to stabilize various MOFs, expanding the scope of MOF systems in biomedical applications. Further exploration could involve assessing dual metal MOF systems like Fe + Mn to enhance relaxivity. Additionally, exploring near-infrared light-absorbing fluorescent dyes such as indocyanine green for imaging could improve the system's imaging capabilities. In conclusion, the combination of MOFs and polymer surface stabilization using PEG-p(Asp-Dopa) offers valuable insights for the development of versatile MOFs/polymer hybrids with potential applications *in vivo*.

Acknowledgements

I extend my deepest gratitude to Associate Professor Horacio Cabral for his invaluable support and guidance throughout my 3-year PhD journey, especially during the challenging period of COVID-19 entrance restrictions (2020/10/1 to 2022/04/01). Despite the restriction, Prof. Cabral provided unwavering mentorship and supervision, even while I was in Taiwan due to the pandemic. His expertise and insights were instrumental in completing this dissertation. I am also grateful to Professor Jiashing Yu and Professor Kevin C.-W. Wu at National Taiwan University for their kind guidance during the initial year of my PhD studies amidst the COVID-19 entry restrictions.

I am very grateful to Professor Madoka Takai, Professor Taichi Ito, Professor Takamasa Sakai, and Associate Professor Hirotaka Ejima for their critical input and kind suggestions. Our discussions were stimulating and motivated me to improve my work in the future. Additionally, I would like to express my gratitude to Professor Ichio Aoki, and Dr. Kensuke Osada in Quantum Science and Technology and Dr. Xueying Liu in Innovation Center of NanoMedicine for their help in MRI experiments.

A huge thank you to all the members of Cabral Lab, in particular, Dr. Taehun Hong and Mr. Pengwen Chen for their help in research expertise. I am very grateful to Dr. Lucas Mixich for his continuous support and companionship. Additionally, a big thank you to Mr. Ming-Feng Hsieh for his help in MOF synthesis. Special thanks to Mrs. Hiroko Koyama for her tireless support and assistance. Thanks to them, even though I only spent 2 years physically in lab, I will remember my time at The University of Tokyo for whole my life.

Finally, I would like to express my love and thanks to my friends and family in Taiwan as well as my wife, Mrs. Yi-Hsueh Yang, who were always there for me and giving huge support.

Achievements

I. Original Articles:

1. **Shang-Wei Li**, Ming-Feng Hsieh, Taehun Hong, Pengwen Chen, Kensuke Osada, Xueying Liu, Ichio Aoki, Jiashing Yu, Kevin C.-W. Wu and Horacio Cabral, "Block copolymer-stabilized MOF hybrids loading Pd nanoparticles enable tumor remission through near-infrared photothermal therapy." *Adv. Nanobiomed Res*. 2023, DOI: 10.1002/anbr.202300107. **Selected as cover picture.**
2. Pengwen Chen, Wenqian Yang, Koji Nagaoka, George Lo Huang, Takuya Miyazaki, Taehun Hong, **Shang-Wei Li**, Kazunori Igarashi, Kazuyoshi Takeda, Kazuhiro Kakimi, Kazunori Kataoka, and Horacio Cabral, "An IL-12-based nanocytokine safely potentiates anticancer immunity through spatiotemporal control of inflammation to eradicate advanced cold tumors." *Adv. Sci*. 2023, 10, 2205139.

II. Conferences:

Oral presentations

- **Shang-Wei Li**, Ming-Feng Hsieh, Taehun Hong, Jiashing Yu, Kevin C.-W. Wu, and Horacio Cabral, International Conference on Precision Nanomedicine in Theranostics, Taichung, Taiwan, July 2023.

III. Honor:

- Benefit-type scholarship from *The University of Tokyo*, The University of Tokyo Fellowship, Apr. 2021 – Mar. 2024.

IV. Other:

International collaboration

- Development of metal organic framework with polymer hybrids, Jan. 2021 – Jan. 2024, The University of Tokyo and National Taiwan University.

References

Akbarzadehlaleh, P., Mirzaei, M., Mashahdi-Keshtiban, M., and Heidari, H. R., **2021**, The Effect of Length and Structure of Attached Polyethylene Glycol Chain on Hydrodynamic Radius, and Separation of PEGylated Human Serum Albumin by Chromatography, *Adv Pharm Bull*, 11(4), 728.

Al Haydar, M., Abid, H. R., Sunderland, B., and Wang, S., **2017**, Metal organic frameworks as a drug delivery system for flurbiprofen, *Drug Design, Development and Therapy*, 11, 2685.

Alshehri, S., Imam, S. S., Rizwanullah, M., Akhter, S., Mahdi, W., Kazi, M., and Ahmad, J., **2021**, Progress of Cancer Nanotechnology as Diagnostics, Therapeutics, and Theranostics Nanomedicine: Preclinical Promise and Translational Challenges, *Pharmaceutics*, 13(1), 24.

Asati, A., Santra, S., Kaittanis, C., and Perez, J. M., **2010**, Surface-charge-dependent cell localization and cytotoxicity of cerium oxide nanoparticles, *Acs Nano*, 4 9, 5321.

Babacic, H., Lehtio, J., Pico de Coana, Y., Pernemalm, M., and Eriksson, H., **2020**, In-depth plasma proteomics reveals increase in circulating PD-1 during anti-PD-1 immunotherapy in patients with metastatic cutaneous melanoma, *J Immunother Cancer*, 8(1).

Bajracharya, R., Song, J. G., Patil, B. R., Lee, S. H., Noh, H. M., Kim, D. H., et al., **2022**, Functional ligands for improving anticancer drug therapy: current status and applications to drug delivery systems, *Drug Deliv*, 29(1), 1959.

Bian, W., Wang, Y., Pan, Z., Chen, N., Li, X., Wong, W.-L., et al., **2021**, Review of Functionalized Nanomaterials for Photothermal Therapy of Cancers, *Acs Appl Nano Mater*, 4(11), 11353.

Breitenborn, H., Dong, J., Piccoli, R., Bruhacs, A., Besteiro, L. V., Skripka, A., et al., **2019**, Quantifying the photothermal conversion efficiency of plasmonic nanoparticles by means of terahertz radiation, *APL Photonics*, 4(12).

Budijono, S. J., Russ, B., Saad, W., Adamson, D. H., and Prud'homme, R. K., **2010**, Block copolymer surface coverage on nanoparticles, *Colloids and Surfaces A: Physicochemical and Engineering Aspects*, 360(1), 105.

Bunzen, H., **2021**, Chemical Stability of Metal-organic Frameworks for Applications in Drug Delivery, *ChemNanoMat*, 7(9), 998.

Cabral, H., and Kataoka, K., **2014**, Progress of drug-loaded polymeric micelles into clinical studies, *Journal of Controlled Release*, 190, 465.

Cabral, H., Li, J., Miyata, K., and Kataoka, K., **2023**, Controlling the biodistribution and clearance of nanomedicines, *Nature Reviews Bioengineering*, 10.1038/s44222.

Cabral, H., Miyata, K., Osada, K., and Kataoka, K., **2018**, Block Copolymer Micelles in Nanomedicine Applications, *Chem Rev*, 118(14), 6844.

Cabral, H., Nishiyama, N., Okazaki, S., Koyama, H., and Kataoka, K., **2005**, Preparation and biological properties of dichloro(1,2-diaminocyclohexane)platinum(II) (DACHPt)-loaded polymeric micelles, *J Control Release*, 101(1-3), 223.

Charalampaki, P., Nakamura, M., Athanasopoulos, D., and Heimann, A., **2019**, Confocal-Assisted Multispectral Fluorescent Microscopy for Brain Tumor Surgery, *Front Oncol*, 9, 583.

Chen, B., Li, Y., Du, Q., Pi, X., Wang, Y., Sun, Y., et al., **2022**, Effective Removal of Tetracycline from Water Using Copper Alginate @ Graphene Oxide with In-Situ Grown MOF-525 Composite: Synthesis, Characterization and Adsorption Mechanisms,

Nanomaterials (Basel), 12(17).
Chen, P. W., Yang, W. Q., Nagaoka, K., Huang, G. L., Miyazaki, T., Hong, T. H., et al., **2023**, An IL-12-Based Nanocytokine Safely Potentiates Anticancer Immunity through Spatiotemporal Control of Inflammation to Eradicate Advanced Cold Tumors, *Adv Sci*, 10(10).
Chen, W.-H., Vázquez-González, M., Zoabi, A., Abu-Reziq, R., and Willner, I., **2018**, Biocatalytic cascades driven by enzymes encapsulated in metal–organic framework nanoparticles, *Nature Catalysis*, 1(9), 689.
Chen, Y., Liu, W., Shang, Y., Cao, P., Cui, J., Li, Z., Yin, X., and Li, Y., **2019**, Folic acid-nanoscale gadolinium-porphyrin metal-organic frameworks: fluorescence and magnetic resonance dual-modality imaging and photodynamic therapy in hepatocellular carcinoma, *Int J Nanomedicine*, 14, 57.
Chien, W. C., Cheng, P. H., Cheng, X. J., Chuang, C. C., Huang, Y. T., Anilkumar, T. S., Liu, C. H., Lu, Y. J., and Wu, K. C. W., **2021**, MCP-1-Functionalized, Core-Shell Gold Nanorod@Iron-Based Metal-Organic Framework (MCP-1/GNR@MIL-100(Fe)) for Photothermal Therapy, *Acs Appl Mater Inter*, 13(44), 52092.
Christodoulou, I., Bourguignon, T., Li, X., Patriarche, G., Serre, C., Marliere, C., and Gref, R., **2021**, Degradation Mechanism of Porous Metal-Organic Frameworks by In Situ Atomic Force Microscopy, *Nanomaterials (Basel)*, 11(3).
Correia, J. H., Rodrigues, J. A., Pimenta, S., Dong, T., and Yang, Z., **2021**, Photodynamic Therapy Review: Principles, Photosensitizers, Applications, and Future Directions, *Pharmaceutics*, 13(9), 1332.
Czarnomysy, R., Radomska, D., Szewczyk, O. K., Roszczenko, P., and Bielawski, K., **2021**, Platinum and Palladium Complexes as Promising Sources for Antitumor Treatments, *Int J Mol Sci*, 22(15).
D'Este, M., Eglin, D., and Alini, M., **2014**, A systematic analysis of DMTMM vs EDC/NHS for ligation of amines to Hyaluronan in water, *Carbohyd Polym*, 108, 239.
Dai, Q., Wilhelm, S., Ding, D., Syed, A. M., Sindhwani, S., Zhang, Y., Chen, Y. Y., MacMillan, P., and Chan, W. C. W., **2018**, Quantifying the Ligand-Coated Nanoparticle Delivery to Cancer Cells in Solid Tumors, *Acs Nano*, 12(8), 8423.
Ding, M., Cai, X., and Jiang, H. L., **2019**, Improving MOF stability: approaches and applications, *Chem Sci*, 10(44), 10209.
Domingues, C., Alvarez-Lorenzo, C., Concheiro, A., Veiga, F., and Figueiras, A., **2019**, Nanotheranostic Pluronic-Like Polymeric Micelles: Shedding Light into the Dark Shadows of Tumors, *Molecular Pharmaceutics*, 16(12), 4757.
Egorova, K. S., and Ananikov, V. P., **2017**, Toxicity of Metal Compounds: Knowledge and Myths, *Organometallics*, 36(21), 4071.
Elmehrath, S., Nguyen, H. L., Karam, S. M., Amin, A., and Greish, Y. E., **2023**, BioMOF-Based Anti-Cancer Drug Delivery Systems, *Nanomaterials (Basel)*, 13(5).
Evangelopoulos, M., Parodi, A., Martinez, J. O., and Tasciotti, E., **2018**, Trends towards Biomimicry in Theranostics, *Nanomaterials (Basel)*, 8(9).
Fan, Z., Liu, H., Xue, Y., Lin, J., Fu, Y., Xia, Z., et al., **2021**, Reversing cold tumors to hot: An immunoadjuvant-functionalized metal-organic framework for multimodal imaging-guided synergistic photo-immunotherapy, *Bioact Mater*, 6(2), 312.
Fang, J., Islam, W., and Maeda, H., **2020**, Exploiting the dynamics of the EPR effect and strategies to improve the therapeutic effects of nanomedicines by using EPR effect enhancers, *Advanced Drug Delivery Reviews*, 157, 142.
Figueiredo Borgognoni, C., Kim, J. H., Zucolotto, V., Fuchs, H., and Riehemann, K., **2018**, Human macrophage responses to metal-oxide nanoparticles: a review, *Artif Cells Nanomed Biotechnol*, 46(sup2), 694.

Friedman, A. A., Letai, A., Fisher, D. E., and Flaherty, K. T., **2015**, Precision medicine for cancer with next-generation functional diagnostics, *Nat Rev Cancer*, 15(12), 747.

Fu, L., Huang, Y., Hou, J., Sun, M., Wang, L., Wang, X., and Chen, L., **2022**, A Raman/fluorescence dual-modal imaging guided synergistic photothermal and photodynamic therapy nanoplatform for precision cancer theranostics, *J Mater Chem B*, 10(41), 8432.

Gallo-Bernal, S., Patino-Jaramillo, N., Calixto, C. A., Higuera, S. A., Forero, J. F., Lara Fernandes, J., et al., **2022**, Nephrogenic Systemic Fibrosis in Patients with Chronic Kidney Disease after the Use of Gadolinium-Based Contrast Agents: A Review for the Cardiovascular Imager, *Diagnostics (Basel)*, 12(8).

Gao, G., Xing, Y., Liu, T., Wang, J., and Hou, X., **2019**, UiO-66(Zr) as sorbent for porous membrane protected micro-solid-phase extraction androgens and progestogens in environmental water samples coupled with LC-MS/MS analysis: The application of experimental and molecular simulation method, *Microchemical Journal*, 146, 126.

Garai, M., and Yavuz, C. T., **2021**, Robust Mesoporous Zr-MOF with Pd Nanoparticles for Formic-Acid-Based Chemical Hydrogen Storage, *Matter*, 4(1), 10.

Giliopoulos, D., Zamboulis, A., Giannakoudakis, D., Bikiaris, D., and Triantafyllidis, K., **2020**, Polymer/Metal Organic Framework (MOF) Nanocomposites for Biomedical Applications, *Molecules*, 25(1).

Gou, Y., Miao, D., Zhou, M., Wang, L., Zhou, H., and Su, G., **2018**, Bio-Inspired Protein-Based Nanoformulations for Cancer Theranostics, *Front Pharmacol*, 9, 421.

Grazon, C., Salas-Ambrosio, P., Ibarboure, E., Buol, A., Garanger, E., Grinstaff, M. W., Lecommandoux, S., and Bonduelle, C., **2020**, Aqueous Ring-Opening Polymerization-Induced Self-Assembly (ROPISA) of N-Carboxyanhydrides, *Angew Chem Int Ed Engl*, 59(2), 622.

Guo, S., Gu, D., Yang, Y., Tian, J., and Chen, X., **2023**, Near-infrared photodynamic and photothermal co-therapy based on organic small molecular dyes, *Journal of Nanobiotechnology*, 21(1), 348.

Hansson, S., Trouillet, V., Tischer, T., Goldmann, A. S., Carlmark, A., Barner-Kowollik, C., and Malmstrom, E., **2013**, Grafting efficiency of synthetic polymers onto biomaterials: a comparative study of grafting-from versus grafting-to, *Biomacromolecules*, 14(1), 64.

Hapuarachchige, S., and Artemov, D., **2020**, Theranostic Pretargeting Drug Delivery and Imaging Platforms in Cancer Precision Medicine, *Front Oncol*, 10, 1131.

Horcajada, P., Chalati, T., Serre, C., Gillet, B., Sebrie, C., Baati, T., et al., **2010**, Porous metal-organic-framework nanoscale carriers as a potential platform for drug delivery and imaging, *Nat Mater*, 9(2), 172.

Horcajada, P., Surblé, S., Serre, C., Hong, D.-Y., Seo, Y.-K., Chang, J.-S., Grenèche, J.-M., Margiolaki, I., and Férey, G., **2007**, Synthesis and catalytic properties of MIL-100(Fe), an iron(iii) carboxylate with large pores, *Chemical Communications*(27), 2820.

Horseman, M., Panahi, L., Udeani, G., Tenpas, A. S., Verduzco, R., Jr., Patel, P. H., et al., **2022**, Drug-Induced Hyperthermia Review, *Cureus*, 14(7), e27278.

Huang, J., Xu, Z., jiang, Y., Law, W.-c., Dong, B., Zeng, X., et al., **2021**, Metal organic framework-coated gold nanorod as an on-demand drug delivery platform for chemo-photothermal cancer therapy, *Journal of Nanobiotechnology*, 19(1), 219.

Imaoka, H., Sasaki, M., Hashimoto, Y., Watanabe, K., Miyazawa, S., Shibuki, T., Mitsunaga, S., and Ikeda, M., **2021**, Impact of Endoscopic Ultrasound-Guided Tissue Acquisition on Decision-Making in Precision Medicine for Pancreatic Cancer: Beyond Diagnosis, *Diagnostics (Basel)*, 11(7).

Inoue, K., **2017**, 5-Aminolevulinic acid-mediated photodynamic therapy for bladder cancer, *Int J Urol*, 24(2), 97.

Ishiguchi, T., and Takahashi, S., **2010**, Safety of Gadoterate Meglumine (Gd-DOTA) as a Contrast Agent for Magnetic Resonance Imaging, *Drugs in R & D*, 10(3), 133.
Jain, A., Ong, S. P., Hautier, G., Chen, W., Richards, W. D., Dacek, S., et al., **2013**, Commentary: The Materials Project: A materials genome approach to accelerating materials innovation, *APL Materials*, 1(1).
Jin, X., Zeng, Q., Zheng, J., Xing, D., and Zhang, T., **2021**, Aptamer-Functionalized Upconverting Nanoformulations for Light-Switching Cancer-Specific Recognition and In Situ Photodynamic-Chemo Sequential Theranostics, *ACS Appl Mater Interfaces*, 13(8), 9316.
Johnson, K. K., Koshy, P., Yang, J.-L., and Sorrell, C. C., **2021**, Preclinical Cancer Theranostics—From Nanomaterials to Clinic: The Missing Link, *Adv Funct Mater*, 31(43), 2104199.
Kalaj, M., Bentz, K. C., Ayala, S., Palomba, J. M., Barcus, K. S., Katayama, Y., and Cohen, S. M., **2020**, MOF-Polymer Hybrid Materials: From Simple Composites to Tailored Architectures, *Chem Rev*, 120(16), 8267.
Kenny, R. G., and Marmion, C. J., **2019**, Toward Multi-Targeted Platinum and Ruthenium Drugs-A New Paradigm in Cancer Drug Treatment Regimens?, *Chem Rev*, 119(2), 1058.
Kumar, P., Tambe, P., Paknikar, K. M., and Gajbhiye, V., **2018**, Mesoporous silica nanoparticles as cutting-edge theranostics: Advancement from merely a carrier to tailor-made smart delivery platform, *Journal of Controlled Release*, 287, 35.
Kush, P., Bajaj, T., Kaur, M., Madan, J., Jain, U. K., Kumar, P., Deep, A., and Kim, K. H., **2020**, Biodistribution and Pharmacokinetic Study of Gemcitabine Hydrochloride Loaded Biocompatible Iron-Based Metal Organic Framework, *J Inorg Organomet P*, 30(8), 2827.
La, T., Jin, L., Liu, X. Y., Song, Z. H., Farrelly, M., Feng, Y. C., et al., **2020**, Cylindromatosis Is Required for Survival of a Subset of Melanoma Cells, *Oncology Research Featuring Preclinical and Clinical Cancer Therapeutics*, 28(4), 385.
Lan, G., Ni, K., Xu, Z., Veroneau, S. S., Song, Y., and Lin, W., **2018**, Nanoscale Metal-Organic Framework Overcomes Hypoxia for Photodynamic Therapy Primed Cancer Immunotherapy, *J Am Chem Soc*, 140(17), 5670.
Le, B. T., La, D. D., and Nguyen, P. T. H., **2023**, Ultrasonic-Assisted Fabrication of MIL-100(Fe) Metal–Organic Frameworks as a Carrier for the Controlled Delivery of the Chloroquine Drug, *ACS Omega*, 8(1), 1262.
Le, T. N.-M., Chiu, C.-c., and Kuo, J.-L., **2021**, A decomposition mechanism for Mn2(DSBDC) metal–organic frameworks in the presence of water molecules, *Physical Chemistry Chemical Physics*, 23(39), 22794.
Li, B., Wang, X., Chen, L., Zhou, Y., Dang, W., Chang, J., and Wu, C., **2018**, Ultrathin Cu-TCPP MOF nanosheets: a new theragnostic nanoplatform with magnetic resonance/near-infrared thermal imaging for synergistic phototherapy of cancers, *Theranostics*, 8(15), 4086.
Li, J., Zhang, W., Ji, W., Wang, J., Wang, N., Wu, W., et al., **2021**, Near infrared photothermal conversion materials: mechanism, preparation, and photothermal cancer therapy applications, *J Mater Chem B*, 9(38), 7909.
Li, S. W., Hsieh, M. F., Hong, T. H., Chen, P. W., Osada, K., Liu, X. Y., et al., **2023**, Block copolymer-stabilized MOF hybrids loading Pd nanoparticles enable tumor remission through near-infrared photothermal therapy, *Adv. Nanobiomed Res.*, in press.
Li, X. S., Lovell, J. F., Yoon, J., and Chen, X. Y., **2020**, Clinical development and potential of photothermal and photodynamic therapies for cancer, *Nat Rev Clin Oncol*, 17(11), 657.
Li, Y., Zhong, H., Jin, Y., Guan, B., Yue, J., Zhao, R., and Huang, Y., **2022**, Metal-Organic

Framework Accelerated One-Step Capture and Reduction of Palladium to Catalytically Active Nanoparticles, *ACS Appl Mater Interfaces*, 14(35), 40408.
Liang, C., Xu, L., Song, G., and Liu, Z., **2016**, Emerging nanomedicine approaches fighting tumor metastasis: animal models, metastasis-targeted drug delivery, phototherapy, and immunotherapy, *Chem Soc Rev*, 45(22), 6250.
Liang, R. W., Luo, S. G., Jing, F. F., Shen, L. J., Qin, N., and Wu, L., **2015**, A simple strategy for fabrication of Pd@MIL-100(Fe) nanocomposite as a visible-light-driven photocatalyst for the treatment of pharmaceuticals and personal care products (PPCPs), *Appl Catal B-Environ*, 176, 240.
Liu, H., Lv, X., Qian, J., Li, H., Qian, Y., Wang, X., Meng, X., Lin, W., and Wang, H., **2020**, Graphitic Carbon Nitride Quantum Dots Embedded in Carbon Nanosheets for Near-Infrared Imaging-Guided Combined Photo-Chemotherapy, *Acs Nano*, 14(10), 13304.
Liu, H., Xu, C., Meng, M., Li, S., Sheng, S., Zhang, S., Ni, W., Tian, H., and Wang, Q., **2022**, Metal-organic framework-mediated multifunctional nanoparticles for combined chemo-photothermal therapy and enhanced immunotherapy against colorectal cancer, *Acta Biomater*, 144, 132.
Liu, J., Zheng, X., Yan, L., Zhou, L., Tian, G., Yin, W., et al., **2015**, Bismuth Sulfide Nanorods as a Precision Nanomedicine for in Vivo Multimodal Imaging-Guided Photothermal Therapy of Tumor, *Acs Nano*, 9(1), 696.
Liu, Y., Li, J., Chen, M., Chen, X., and Zheng, N., **2020**, Palladium-based nanomaterials for cancer imaging and therapy, *Theranostics*, 10(22), 10057.
Lucky, S. S., Soo, K. C., and Zhang, Y., **2015**, Nanoparticles in photodynamic therapy, *Chem Rev*, 115(4), 1990.
Lv, Z., He, S., Wang, Y., and Zhu, X., **2021**, Noble Metal Nanomaterials for NIR-Triggered Photothermal Therapy in Cancer, *Advanced Healthcare Materials*, 10(6), 2001806.
Madamsetty, V. S., Mukherjee, A., and Mukherjee, S., **2019**, Recent Trends of the Bio-Inspired Nanoparticles in Cancer Theranostics, *Front Pharmacol*, 10, 1264.
Malonzo, C. D., Wang, Z., Duan, J., Zhao, W., Webber, T. E., Li, Z., et al., **2018**, Application and Limitations of Nanocasting in Metal-Organic Frameworks, *Inorg Chem*, 57(5), 2782.
Marquez, A. G., Demessence, A., Platero-Prats, A. E., Heurtaux, D., Horcajada, P., Serre, C., et al., **2012**, Green Microwave Synthesis of MIL-100(Al, Cr, Fe) Nanoparticles for Thin-Film Elaboration, *Eur J Inorg Chem*(32), 5165.
McNerney, M. P., Doiron, K. E., Ng, T. L., Chang, T. Z., and Silver, P. A., **2021**, Theranostic cells: emerging clinical applications of synthetic biology, *Nat Rev Genet*, 22(11), 730.
Mi, P., Cabral, H., and Kataoka, K., **2020**, Ligand-Installed Nanocarriers toward Precision Therapy, *Adv Mater*, 32(13), e1902604.
Mieog, J. S. D., Achterberg, F. B., Zlitni, A., Hutteman, M., Burggraaf, J., Swijnenburg, R. J., Gioux, S., and Vahrmeijer, A. L., **2022**, Fundamentals and developments in fluorescence-guided cancer surgery, *Nat Rev Clin Oncol*, 19(1), 9.
Moghimi, S. M., Hunter, A. C., and Andresen, T. L., **2012**, Factors controlling nanoparticle pharmacokinetics: an integrated analysis and perspective, *Annu Rev Pharmacol Toxicol*, 52, 481.
Mokhtarian, F., Rastegari, B., Zeinali, S., Tohidi, M., and Karbalaei-Heidari, H. R., **2022**, Theranostic Effect of Folic Acid Functionalized MIL-100(Fe) for Delivery of Prodigiosin and Simultaneous Tracking-Combating Breast Cancer, *Journal of Nanomaterials*, 2022, 1108865.
Munawar, J., Khan, M. S., Zehra Syeda, S. E., Nawaz, S., Janjhi, F. A., Ul Haq, H., Rashid, E. U., Jesionowski, T., and Bilal, M., **2023**, Metal-organic framework-based smart nanoplatforms for biosensing, drug delivery, and cancer theranostics, *Inorganic*

Chemistry Communications, 147, 110145.
Na, H. B., Song, I. C., and Hyeon, T., **2009**, Inorganic Nanoparticles for MRI Contrast Agents, *Adv Mater*, 21(21), 2133.
Nabil, G., Bhise, K., Sau, S., Atef, M., El-Banna, H. A., and Iyer, A. K., **2019**, Nano-engineered delivery systems for cancer imaging and therapy: Recent advances, future direction and patent evaluation, *Drug Discov Today*, 24(2), 462.
Ni, K., Luo, T., Nash, G. T., and Lin, W., **2020**, Nanoscale Metal–Organic Frameworks for Cancer Immunotherapy, *Accounts of Chemical Research*, 53(9), 1739.
Nunes, R. W., Martin, J. R., and Johnson, J. F., **1982**, Influence of molecular weight and molecular weight distribution on mechanical properties of polymers, *Polymer Engineering & Science*, 22(4), 205.
Overchuk, M., Weersink, R. A., Wilson, B. C., and Zheng, G., **2023**, Photodynamic and Photothermal Therapies: Synergy Opportunities for Nanomedicine, *Acs Nano*, 17(9), 7979.
Pander, M., Gil-San-Millan, R., Delgado, P., Perona-Bermejo, C., Kostrzewa, U., Kaczkowski, K., Kubicki, D. J., Navarro, J. A. R., and Bury, W., **2023**, MOF/polymer hybrids through in situ free radical polymerization in metal-organic frameworks, *Materials Horizons*, 10(4), 1301.
Peng, Q., Qian, Z., Gao, H., and Zhang, K., **2022**, Recent Advances in Transition-Metal Based Nanomaterials for Noninvasive Oncology Thermal Ablation and Imaging Diagnosis, *Front Chem*, 10, 899321.
Phan, T. T. V., Huynh, T. C., Manivasagan, P., Mondal, S., and Oh, J., **2020**, An Up-To-Date Review on Biomedical Applications of Palladium Nanoparticles, *Nanomaterials-Basel*, 10(1).
Porter, J., Arreguin, S., and Pierpont, C. G., **2010**, Ferric iron complexes of dopamine and 5,6-dihydroxyindole with nta, edda, and edta as ancillary ligands, *Inorganica Chimica Acta*, 363(12), 2800.
Poryvaev, A. S., Yazikova, A. A., Polyukhov, D. M., Chinak, O. A., Richter, V. A., Krumkacheva, O. A., and Fedin, M. V., **2021**, Guest Leakage from ZIF-8 Particles under Drug Delivery Conditions: Quantitative Characterization and Guest-Induced Framework Stabilization, *The Journal of Physical Chemistry C*, 125(28), 15606.
Qin, J., Wang, X., Fan, G., Lv, Y., and Ma, J., **2023**, Recent Advances in Nanodrug Delivery System for Tumor Combination Treatment Based on Photothermal Therapy, *Advanced Therapeutics*, 6(3), 2200218.
Quijia, C. R., Lima, C., Silva, C., Alves, R. C., Frem, R., and Chorilli, M., **2021**, Application of MIL-100(Fe) in drug delivery and biomedicine, *J Drug Deliv Sci Tec*, 61.
Raja, I. S., Kang, M. S., Kim, K. S., Jung, Y. J., and Han, D. W., **2020**, Two-Dimensional Theranostic Nanomaterials in Cancer Treatment: State of the Art and Perspectives, *Cancers (Basel)*, 12(6).
Rubio-Ruiz, B., Perez-Lopez, A. M., Bray, T. L., Lee, M., Serrels, A., Prieto, M., et al., **2018**, High-Precision Photothermal Ablation Using Biocompatible Palladium Nanoparticles and Laser Scanning Microscopy, *Acs Appl Mater Inter*, 10(4), 3341.
Schmitt, S., Hümmer, J., Kraus, S., Welle, A., Grosjean, S., Hanke-Roos, M., et al., **2016**, Tuning the Cell Adhesion on Biofunctionalized Nanoporous Organic Frameworks, *Adv Funct Mater*, 26(46), 8455.
Schwab, K. S., Heine, A., Weimann, T., Kristiansen, G., and Brossart, P., **2016**, Development of Hemolytic Anemia in a Nivolumab-Treated Patient with Refractory Metastatic Squamous Cell Skin Cancer and Chronic Lymphatic Leukemia, *Case Rep Oncol*, 9(2), 373.
Shi, L., Wu, J., Qiao, X., Ha, Y., Li, Y., Peng, C., and Wu, R., **2020**, In Situ Biomimetic

Mineralization on ZIF-8 for Smart Drug Delivery, *ACS Biomater Sci Eng*, 6(8), 4595.
Shi, L., Zhang, J., Zhao, M., Tang, S., Cheng, X., Zhang, W., et al., **2021**, Effects of polyethylene glycol on the surface of nanoparticles for targeted drug delivery, *Nanoscale*, 13(24), 10748.
Shirata, C., Kaneko, J., Inagaki, Y., Kokudo, T., Sato, M., Kiritani, S., et al., **2017**, Near-infrared photothermal/photodynamic therapy with indocyanine green induces apoptosis of hepatocellular carcinoma cells through oxidative stress, *Sci Rep-Uk*, 7(1), 13958.
Siamaki, A. R., Khder, A. E. R. S., Abdelsayed, V., El-Shall, M. S., and Gupton, B. F., **2011**, Microwave-assisted synthesis of palladium nanoparticles supported on graphene: A highly active and recyclable catalyst for carbon–carbon cross-coupling reactions, *Journal of Catalysis*, 279(1), 1.
Silva, C. O., Pinho, J. O., Lopes, J. M., Almeida, A. J., Gaspar, M. M., and Reis, C., **2019**, Current Trends in Cancer Nanotheranostics: Metallic, Polymeric, and Lipid-Based Systems, *Pharmaceutics*, 11(1).
Simon-Yarza, T., Baati, T., Neffati, F., Njim, L., Couvreur, P., Serre, C., et al., **2016**, In vivo behavior of MIL-100 nanoparticles at early times after intravenous administration, *Int J Pharmaceut*, 511(2), 1042.
Simon, M. A., Anggraeni, E., Soetaredjo, F. E., Santoso, S. P., Irawaty, W., Thanh, T. C., Hartono, S. B., Yuliana, M., and Ismadji, S., **2019**, Hydrothermal Synthesize of HF-Free MIL-100(Fe) for Isoniazid-Drug Delivery, *Sci Rep*, 9(1), 16907.
Singh, N., Qutub, S., and Khashab, N. M., **2021**, Biocompatibility and biodegradability of metal organic frameworks for biomedical applications, *J Mater Chem B*, 9(30), 5925.
Singh, P., Haloi, P., Singh, K., Roy, S., Sarkar, A., B, S. L., et al., **2023**, Palladium Nanocapsules for Photothermal Therapy in the Near-Infrared II Biological Window, *ACS Appl Mater Interfaces*, 15(33), 39081.
Song, G., Kenney, M., Chen, Y.-S., Zheng, X., Deng, Y., Chen, Z., et al., **2020**, Carbon-coated FeCo nanoparticles as sensitive magnetic-particle-imaging tracers with photothermal and magnetothermal properties, *Nature Biomedical Engineering*, 4(3), 325.
Sun, T., Zhang, Y. S., Pang, B., Hyun, D. C., Yang, M., and Xia, Y., **2014**, Engineered nanoparticles for drug delivery in cancer therapy, *Angew Chem Int Ed Engl*, 53(46), 12320.
Troyano, J., and Maspoch, D., **2023**, Propagating MOF flexibility at the macroscale: the case of MOF-based mechanical actuators, *Chemical Communications*, 59(13), 1744.
Turner, J. H., **2018**, An introduction to the clinical practice of theranostics in oncology, *Br J Radiol*, 91(1091), 20180440.
van der Heide, C. D., and Dalm, S. U., **2022**, Radionuclide imaging and therapy directed towards the tumor microenvironment: a multi-cancer approach for personalized medicine, *Eur J Nucl Med Mol Imaging*, 49(13), 4616.
Vojtek, M., Pinto, E., Goncalves-Monteiro, S., Almeida, A., Marques, M. P. M., Mota-Filipe, H., Ferreira, I. M. P. L. V. O., and Diniz, C., **2020**, Fast and reliable ICP-MS quantification of palladium and platinum-based drugs in animal pharmacokinetic and biodistribution studies, *Anal Methods-Uk*, 12(39), 4806.
Vrtovec, N., Jurjevec, S., Zabukovec Logar, N., Mazaj, M., and Kovačič, S., **2023**, Metal Oxide-Derived MOF-74 Polymer Composites through Pickering Emulsion-Templating: Interfacial Recrystallization, Hierarchical Architectures, and CO2 Capture Performances, *Acs Appl Mater Inter*, 15(14), 18354.
Wang, J., Han, J., Zhu, C., Han, N., Xi, J., Fan, L., and Guo, R., **2018**, Gold Nanorods/Polypyrrole/m-SiO2 Core/Shell Hybrids as Drug Nanocarriers for Efficient Chemo-Photothermal Therapy, *Langmuir*, 34(48), 14661.
Wang, J. W., Chen, Q. W., Luo, G. F., Han, Z. Y., Song, W. F., Yang, J., Chen, W. H., and Zhang,

X. Z., **2021**, A Self-Driven Bioreactor Based on Bacterium-Metal-Organic Framework Biohybrids for Boosting Chemotherapy via Cyclic Lactate Catabolism, *Acs Nano*, 15(11), 17870.

Wang, K., Du, Y., Zhang, Z., He, K., Cheng, Z., Yin, L., et al., **2023**, Fluorescence image-guided tumour surgery, *Nature Reviews Bioengineering*, 1(3), 161.

Wang, S., Zhao, Y., Zhang, Z., Zhang, Y., and Li, L., **2021**, Recent advances in amino acid-metal coordinated nanomaterials for biomedical applications, *Chinese Journal of Chemical Engineering*, 38, 30.

Wildeman, M. A., Nyst, H. J., Karakullukcu, B., and Tan, B. I., **2009**, Photodynamic therapy in the therapy for recurrent/persistent nasopharyngeal cancer, *Head Neck Oncol*, 1, 40.

Wu, J., **2021**, The Enhanced Permeability and Retention (EPR) Effect: The Significance of the Concept and Methods to Enhance Its Application, *J Pers Med*, 11(8).

Xiao, J. W., Fan, S. X., Wang, F., Sun, L. D., Zheng, X. Y., and Yan, C. H., **2014**, Porous Pd nanoparticles with high photothermal conversion efficiency for efficient ablation of cancer cells, *Nanoscale*, 6(8), 4345.

Xu, J., Wang, J., Ye, J., Jiao, J., Liu, Z., Zhao, C., Li, B., and Fu, Y., **2021**, Metal-Coordinated Supramolecular Self-Assemblies for Cancer Theranostics, *Adv Sci (Weinh)*, 8(16), e2101101.

Yadav, P., Kumari, S., Yadav, A., Bhardwaj, P., Maruthi, M., Chakraborty, A., and Kanoo, P., **2023**, Biocompatible Drug Delivery System Based on a MOF Platform for a Sustained and Controlled Release of the Poorly Soluble Drug Norfloxacin, *ACS Omega*, 8(31), 28367.

Yang, J., and Yang, Y.-W., **2020**, Metal-organic framework-based cancer theranostic nanoplatforms, *VIEW*, 1(2), e20.

Yang, Q., Xu, Q., Yu, S.-H., and Jiang, H.-L., **2016**, Pd Nanocubes@ZIF-8: Integration of Plasmon-Driven Photothermal Conversion with a Metal–Organic Framework for Efficient and Selective Catalysis, *Angewandte Chemie International Edition*, 55(11), 3685.

Yang, W., Wang, L., Fang, M., Sheth, V., Zhang, Y., Holden, A. M., et al., **2022**, Nanoparticle Surface Engineering with Heparosan Polysaccharide Reduces Serum Protein Adsorption and Enhances Cellular Uptake, *Nano Lett*, 22(5), 2103.

Yau, T. O., **2019**, Precision treatment in colorectal cancer: Now and the future, *JGH Open*, 3(5), 361.

Ye, Y., Zhao, Y., Sun, Y., and Cao, J., **2022**, Recent Progress of Metal-Organic Framework-Based Photodynamic Therapy for Cancer Treatment, *Int J Nanomedicine*, 17, 2367.

Yin, Y., Yang, J., Pan, Y., Gao, Y., Huang, L., Luan, X., et al., **2021**, Mesopore to Macropore Transformation of Metal-Organic Framework for Drug Delivery in Inflammatory Bowel Disease, *Adv Healthc Mater*, 10(3), e2000973.

Yordanova, A., Eppard, E., Kurpig, S., Bundschuh, R. A., Schonberger, S., Gonzalez-Carmona, M., Feldmann, G., Ahmadzadehfar, H., and Essler, M., **2017**, Theranostics in nuclear medicine practice, *Onco Targets Ther*, 10, 4821.

Yu, G., Zhao, X., Zhou, J., Mao, Z., Huang, X., Wang, Z., et al., **2018**, Supramolecular Polymer-Based Nanomedicine: High Therapeutic Performance and Negligible Long-Term Immunotoxicity, *J Am Chem Soc*, 140(25), 8005.

Yu, J., Mu, C., Yan, B., Qin, X., Shen, C., Xue, H., and Pang, H., **2017**, Nanoparticle/MOF composites: preparations and applications, *Materials Horizons*, 4(4), 557.

Yu, Y., Yu, R., Wang, N., Bai, Y., Shi, Q., Maswikiti, E. P., and Chen, H., **2023**, Photodynamic therapy in combination with immune checkpoint inhibitors plus chemotherapy for first-line treatment in advanced or metastatic gastric or gastroesophageal junction cancer: A phase 2-3 clinical trial protocol, *Front Pharmacol*, 14, 1063775.

Yuan, C., Li, Y., Xu, Z., Wang, C., Zhang, J., Jin, Y., et al., **2022**, Imaging-Guided Synergistic Photo-Chemotherapy Using Doxorubicin-Loaded Gadolinium Porphyrin-Based Metal–Organic Framework Nanosheets, *Acs Appl Nano Mater*, 5(10), 15318.

Zhang, H., Li, Q., Liu, R., Zhang, X., Li, Z., and Luan, Y., **2018**, A Versatile Prodrug Strategy to In Situ Encapsulate Drugs in MOF Nanocarriers: A Case of Cytarabine-IR820 Prodrug Encapsulated ZIF-8 toward Chemo-Photothermal Therapy, *Adv Funct Mater*, 28(35), 1802830.

Zhang, H., and Yin, X. B., **2022**, Mixed-Ligand Metal-Organic Frameworks for All-in-One Theranostics with Controlled Drug Delivery and Enhanced Photodynamic Therapy, *ACS Appl Mater Interfaces*.

Zhang, W., Li, J., Chen, L., Chen, H., and Zhang, L., **2023**, Palladium-based multifunctional nanoparticles for combined chemodynamic/photothermal and calcium overload therapy of tumors, *Colloids Surf B Biointerfaces*, 230, 113529.

Zhang, X., Lu, Y., Jia, D., Qiu, W., Ma, X., Zhang, X., Xu, Z., and Wen, F., **2021**, Acidic microenvironment responsive polymeric MOF-based nanoparticles induce immunogenic cell death for combined cancer therapy, *J Nanobiotechnology*, 19(1), 455.

Zhang, Z., Nguyen, H. T., Miller, S. A., and Cohen, S. M., **2015**, polyMOFs: A Class of Interconvertible Polymer-Metal-Organic-Framework Hybrid Materials, *Angew Chem Int Ed Engl*, 54(21), 6152.

Zhao, L., Zhang, W., Wu, Q., Fu, C., Ren, X., Lv, K., et al., **2022**, Lanthanide europium MOF nanocomposite as the theranostic nanoplatform for microwave thermo-chemotherapy and fluorescence imaging, *J Nanobiotechnology*, 20(1), 133.

Zheng, Q., Liu, X., Zheng, Y., Yeung, K. W. K., Cui, Z., Liang, Y., et al., **2021**, The recent progress on metal-organic frameworks for phototherapy, *Chem Soc Rev*, 50(8), 5086.

Zuna, I., and Holt, A., **2017**, ADAM, a hands-on patient simulator for teaching principles of drug disposition and compartmental pharmacokinetics, *Br J Clin Pharmacol*, 83(11), 2426.